

# All-atom relativistic molecular dynamics simulations of channeling and radiation processes in oriented crystals

Andrei V. Korol, Gennady B. Sushko, and Andrey V. Solov'yov\*

MBN Research Center, Altenhöferallee 3, 60438 Frankfurt am Main, Germany

E-mail: solovyov@mbnresearch.com

**Abstract.** We review achievements made in recent years in the field of numerical modeling of ultra-relativistic projectiles propagation in oriented crystals, radiation emission and related phenomena. This topic is highly relevant to the problem of designing novel gamma-ray light sources based on the exposure of oriented crystals to the beams of ultra-relativistic charged particles. The paper focuses on the approaches that allow for advanced computation exploration beyond the continuous potential and the binary collisions frameworks. A comprehensive description of the multiscale all-atom relativistic molecular dynamics approach implemented in the MBN EXPLORER package is given. Several case studies related to modeling of ultra-relativistic projectiles (electrons, positron and pions) channeling and photon emission in oriented straight, bent and periodically bent crystals are presented. In most cases, the input data used in the simulations, such as crystal orientation and thickness, the bending radii, periods and amplitudes, as well as the energies of the projectiles, have been chosen to match the parameters used in the accomplished and the ongoing experiments. Wherever available the results of calculations are compared with the experimental data and/or the data obtained by other numerical means.

## 1. Introduction

Development of light sources (LS) for wavelengths  $\lambda$  well below one angstrom (corresponding photon energies  $E_{\text{ph}} \gg 10$  keV) is a challenging goal of modern physics. Sub-angstrom wavelength powerful spontaneous and, especially, coherent radiation will have many applications in the basic sciences, technology and medicine. They may have a revolutionary impact on nuclear and solid-state physics, as well as on the life sciences [1]. Modern X-ray Free-Electron-Laser (XFEL) can generate X-rays with wavelengths  $\lambda \sim 1$  Å [2–5]. Existing synchrotron facilities provide radiation of shorter wavelengths but orders of magnitude less intensive [6, 7]. Therefore, to create a powerful LS in the range  $\lambda \ll 1$  Å new approaches and technologies are needed.

One of the approaches to designing novel gamma-ray LSs relies on the exposure of oriented crystals to the beams of ultra-relativistic charged particles [1]. In an exemplary

case study, presented in the cited paper, brilliance of radiation emitted in Crystalline Undulator (CU) based LSs have been estimated. It was shown that in the range  $E_{\text{ph}} = 10^{-1} - 10^2$  MeV the brilliance is comparable to or higher than the synchrotrons brilliance at much lower photon energies. A rigorous computation of the brilliance [8] based on numerical simulations carried out by means of the MBN EXPLORER software package [9,10] has confirmed the estimates. The brilliance can be boosted by orders of magnitude through the process of superradiance [11] by a pre-bunched beam [12,13]. In this case the brilliance can be comparable with the values achievable at the XFEL facilities which operate in much lower photon energy range [1].

Crystal-based LSs can generate radiation in the photon energy range where the technologies based on the fields of permanent magnets become inefficient or incapable. The limitations of conventional LS is overcome by exploiting very strong crystalline fields. The orientation of a crystal along the beam enhances significantly the strength of the particles interaction with the crystal due to strongly correlated scattering from lattice atoms [14]. This allows for the guided motion of particles through crystals of different geometry and for the enhancement of radiation. A comprehensive review of physics of channeling and radiation emission in periodically bent crystals one finds in [12].

Construction of novel crystal-based LSs is an extremely challenging task, which constitutes a highly interdisciplinary and broad field. A roadmap review [1] presents an overview of the field, outlines the achievements that have been made and discusses the goals which can be achieved. It also provides an updated review of the issues relevant to practical realization of the novel LSs including, in particular, channeling experiments with bent and periodically bent crystals, technologies and methods developed or/and proposed to create bent crystalline structures. The results, data, supportive detailed description of the formalism involved, the discussion of the related phenomena as well as the outlook has been presented in a consistent and complete manner for the first time in the cited paper.

The goal of the current paper is to present recent achievements in one of the research directions within the aforementioned interdisciplinary field, namely, numerical modeling of the channeling and related phenomena. Within this direction we focus on the approaches that allow for advanced computation exploration beyond the continuous potential framework [14]. The computational tools, which are based on the continuous potential concept and on the binary collisions approach, developed in recent years are reviewed briefly in Section 2. A detailed description of the multiscale all-atom relativistic molecular dynamics approach implemented in the MBN EXPLORER package is given in Section 3. In the last years the channeling module of the package [15] has been used extensively to simulate propagation and radiation emission by projectiles in various crystalline media. In Section 4 we present several case studies related to modeling of ultra-relativistic projectiles channeling and calculation of the spectral intensities by means of MBN EXPLORER.

## 2. Overview of numerical approaches to simulate channeling phenomenon

Various approximations have been used to simulate channeling phenomenon in oriented crystals. Whilst most rigorous description relies can be achieved within the framework of quantum mechanics (see recent paper [16] and references therein) quite often classical description in terms of particles trajectories is highly adequate and accurate. Indeed, the number of quantum states  $N$  of the transverse motion of a channeling electron and/or positron increases with its energy as  $N \sim A\sqrt{\gamma}$  where  $A \sim 1$  and  $\gamma = \varepsilon/mc^2$  stands for the relativistic Lorentz factor of a projectile of energy  $\varepsilon$  and mass  $m$  [17,18]. The classical description implies strong inequality  $N \gg 1$ , which becomes well fulfilled for projectile energy in the hundred MeV range and above.

Simulation of channeling and related phenomena has been implemented in several software packages within frameworks of different theoretical approaches. Below we briefly characterize the most recently developed ones.

- The computer code *Basic Channeling with Mathematica* [19] uses continuous potential for analytic solution of the channeling related problems. The code allows for computation of classical trajectories of channeled electrons and positrons in continuous potential as well as for computation of wave functions and energy levels of the particles. Calculation of the spectral distribution of emitted radiation is also supported.
- A toolkit for the simulation of coherent interactions between high-energy charged projectiles with complex crystalline structures called DYNECHARM++ has been developed [20]. The code allows for calculation of electrostatic characteristics (charge densities, electrostatic potential and field) in complex atomic structures and to simulate and track a particle's trajectory. Calculation of the characteristics is based on their expansion in the Fourier series through the ECHARM (Electrical CHARACTERistics of Monocrystals) method [21]. Two different approaches to simulate the interaction have been adopted, relying on (i) the full integration of particle trajectories within the continuum potential approximation, and (ii) the definition of cross-sections of coherent processes. Recently, this software package was supplemented with the RADCHARM+ module [22] which allows for the computation of the emission spectrum by direct integration of the quasi-classical formula of Baier and Katkov [23].
- The CRYSTALRAD simulation code, presented in Ref. [24] is an unification of the CRYSTAL simulation code [25] and the RADCHARM++ routine [22]. The former code is designed for trajectory calculations taking into account various coherent effects of the interaction of relativistic and ultrarelativistic charged particles with straight or bent single crystals and different types of scattering. The program contains one- and two-dimensional models that allow for modeling of classical trajectories of relativistic and ultrarelativistic charged particles in the field of atomic planes and strings, respectively. The algorithm for simulation of motion

of particles in presence of multiple Coulomb scattering is modeled accounting for the suppression of incoherent scattering [26]. In addition to this, nuclear elastic, diffractive, and inelastic scattering are also simulated.

- In Ref. [27] the algorithm based on the Fourier transform method for planar radiation has been presented and implemented to compute the emission spectra of ultra-relativistic electrons and positrons within the Baier-Katkov quasiclassical formalism. Special attention has been given to treat the radiation emission in the planar channeling regime in bent crystals with account for the contributions of both volume reflection and multiple volume reflection events. The simulation presented took into consideration both the nondipole nature and arbitrary multiplicity of radiation accompanying volume reflection. A large axial contribution to the hard part of the radiative energy loss spectrum as well as the strengthening of planar radiation, with respect to the single volume reflection case, in the soft part of the spectrum have been demonstrated.
- The codes described in Ref. [28] (see also [12]) allow for simulation of classical trajectories of ultra-relativistic projectiles in straight and periodically bent crystals as well as for computing spectra-angular distribution of the radiated energy within the quasi-classical formalism [23]. The trajectories are calculated by solving three-dimensional equations of motion with account for: (i) the continuous interplanar potential; (ii) the centrifugal potential due to the crystal bending; (iii) the radiative damping force; (iv) the stochastic force due to the random scattering of the projectile by lattice electrons and nuclei.
- Recently presented code [29] allows one to determine the trajectory of particles traversing oriented single crystals and to evaluate the radiation spectra within the quasi-classical approximation. To calculate the electrostatic field of the crystal lattice the code uses thermally averaged Doyle-Turner continuous potential [30] (see also Appendix A). Beyond this framework, included are multiple Coulomb scattering and energy loss due to radiation emission. It is shown that the use of Graphics Processing Units (GPU) instead of the CPU processors speeds up calculations by several orders of magnitude.
- In Ref. [18] a Monte Carlo code was described which allows one to simulate the electron and positron channeling. The code did not use the continuous potential concept but utilized the algorithm of binary collisions of the projectile with the crystal constituents. However, as it has been argued [12, 15, 31], the code was based on the peculiar model of the elastic scattering of the projectile from the crystal atoms. Namely, atomic electrons are treated as point-like charges placed at fixed positions around the nucleus. The model implies also that the interaction of an projectile with each atomic constituent, electrons included, is treated as the classical Rutherford scattering from a static, infinitely massive point charge. It was demonstrated in the cited papers that in practical simulations, non-zero statistical weight of hard collisions with spatially fixed electrons overestimates the increase of

the root-mean square scattering angle with increasing the propagation distance of the channeling particle. As a result, the model over-counts dechanneling-channeling events resulting from the hard collisions.

### 3. Atomistic molecular dynamics approach

Numerical modeling of the channeling and related phenomena beyond the continuous potential framework can be carried out by means of the multi-purpose computer package MBN EXPLORER [9, 10]. The MBN EXPLORER package was originally developed as a universal computer program to allow investigation of structure and dynamics of molecular systems of different origin on spatial scales ranging from nanometers and beyond.

In order to address the channeling phenomena, an additional module has been incorporated into MBN EXPLORER to compute the motion for relativistic projectiles along with dynamical simulations of the propagation environments, including the crystalline structures, in the course of the projectile's motion [15]. The computation accounts for the interaction of projectiles with separate atoms of the environments, whereas a variety of interatomic potentials implemented in MBN EXPLORER supports rigorous simulations of various media. The software package can be regarded as a powerful numerical tool to reveal the dynamics of relativistic projectiles in crystals, amorphous bodies, as well as in biological environments. Its efficiency and reliability has been benchmarked for the channeling of ultra-relativistic projectiles (within the sub-GeV to tens of GeV energy range) in straight, bent and periodically bent crystals [15, 32–45]. In these papers verification of the code against available experimental data and predictions of other theoretical models was carried out.

#### 3.1. Methodology

The description of the simulation procedure is sketched below.

Within the framework of classical relativistic dynamics propagation of an ultra-relativistic projectile of the charge  $q$  and mass  $m$  through a crystalline medium implies integration of the following two coupled equations of motion (EM):

$$\partial \mathbf{r} / \partial t = \mathbf{v}, \quad \partial \mathbf{p} / \partial t = -q \partial U / \partial \mathbf{r} \quad (1)$$

where  $U = U(\mathbf{r})$  is the electrostatic potential due to the crystal constituents,  $\mathbf{r}(t)$ ,  $\mathbf{v}(t)$ , and  $\mathbf{p}(t) = m\gamma\mathbf{v}(t)$  stand, respectively, for the position vector, velocity and momentum of the particle at instant  $t$ ,  $\gamma = (1 - v^2/c^2)^{-1/2} = \varepsilon/mc^2$  is the relativistic Lorentz factor,  $\varepsilon$  is the particle's energy, and  $c$  is the speed of light.

In MBN EXPLORER, the EM are integrated using the forth-order Runge-Kutta scheme with variable time step. At each step, the potential  $U = U(\mathbf{r})$  is calculated as the sum of potentials  $U_{\text{at}}(\mathbf{r})$  of individual atoms

$$U(\mathbf{r}) = \sum_j U_{\text{at}}(|\mathbf{r} - \mathbf{R}_j|) \quad (2)$$

where  $\mathbf{R}_j$  is the position vector of the  $j$ th atom. The code allows one to evaluate the atomic potential using the approximations due to Molière [46] and Pacios [47] (see also Section Appendix A). A rapid decrease of these potentials with increasing the distances from the atoms allows the sum (2) to be truncated in practical calculations. Only atoms located inside a sphere of the (specified) cut-off radius  $\rho_{\max}$  with the center at the instant location of the projectile. The value  $\rho_{\max}$  is chosen large enough to ensure negligible contribution to the sum from the atoms located at  $r > \rho_{\max}$ . The search for such atoms is facilitated by using the linked cell algorithm implemented in MBN EXPLORER [9,48].

As a first step in simulating the motion along a particular direction, a crystalline lattice is generated inside the rectangular simulation box of the size  $L_x \times L_y \times L_z$ . The  $z$ -axis is oriented along the beam direction. To simulate the axial channeling the  $z$ -axis is directed along a chosen crystallographic direction  $\langle klm \rangle$  (here integers  $k, l, m$  stand for the Miller). In the case planar channeling, the  $z$ -axis is parallel to the  $(klm)$  plane, and the  $y$  axis is perpendicular to the plane. The position vectors of the nodes  $\mathbf{R}_j^{(0)}$  ( $j = 1, 2, \dots, N$ ) within the simulation box are generated in accordance with the type of the Bravais cell of the crystal and using the predefined values of the lattice vectors. The simulation box can be cut along specified faces, thus allowing tailoring the generated crystalline sample to achieve the desired form of the sample.

Several build-in options, characterized below, allow one to further modify the generated crystalline structure [37].

- The sample can be rotated around a specified axis thus allowing for the construction of the crystalline structure along any desired direction. In particular, this option allows one to choose the direction of the  $z$ -axis well away from major crystallographic axes, thus avoiding the axial channeling (when not desired).
- The nodes can be displaced in the transverse direction:  $y \rightarrow y + R(1 - \cos \phi)$  where  $\phi = \arcsin(z/R)$ . As a result, a crystal bent with constant radius  $R$  is generated.
- Periodic harmonic displacement of the nodes is achieved by means of the transformation  $\mathbf{r} \rightarrow \mathbf{r} + \mathbf{a} \sin(\mathbf{k} \cdot \mathbf{r} + \varphi)$ . The vector  $\mathbf{a}$  and its modulus,  $a$ , determine the direction and amplitude of the displacement, the wave-vector  $\mathbf{k}$  specifies the axis along which the displacement to be propagated, and  $\lambda_u = 2\pi/k$  defines the wave-length of the periodic bending. The parameter  $\varphi$  allows one to change the phase-shift of periodic bending.

In a special case  $\mathbf{a} \perp \mathbf{k}$ , this options provides simulation of linearly polarized periodically bent crystalline structure which is an important element of a crystalline undulator.

These transformations, illustrated schematically in Fig. 1left, are reversible and, therefore, allow for efficient construction of a crystalline structure in an arbitrary spatial area. Also, the simulation box can be cut along specified faces, thus allowing tailoring the generated structure to achieve the desired form of the sample. In addition to the aforementioned options, MBN EXPLORER allows one to model binary structures (for example,  $\text{Si}_{1-x}\text{Ge}_x$  or diamond-boron superlattices, see Fig. 1right) can generated by



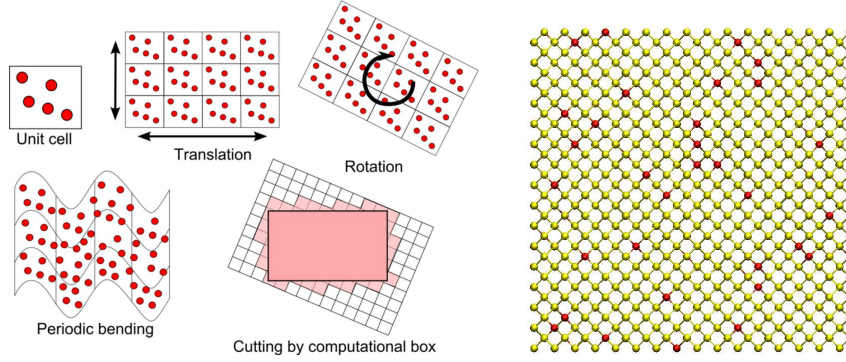


**Figure 1.** *Left.* Construction of a crystalline medium is done through the definition of a unit cell of the crystal and a set of reversible transformations. This approach provides efficient mapping of the coordinates into crystalline reference frame i.e. cutting the periodic crystalline structure by a simulation box. *Right.* Illustrative  $\text{Si}_{1-x}\text{Ge}_x$  binary crystal sample with concentration  $x = 0.05$  of germanium atoms. The silicon and germanium atoms are shown in yellow and red, respectively. The Ge atoms occupy positions in the same grid structure as Si but the difference in the lattice constant leads to a deformation of the whole sample.

introducing random or regular substitution of atoms in the initial structure with the dopant atoms.

Once the nodes are defined, the position vectors of the atomic nuclei are generated with account for random displacement from the nodes due to thermal vibrations corresponding to a given temperature  $T$ . For each atom the displacement vector  $\Delta$  is generated by means of the normal distribution

$$w(\Delta) = \frac{1}{(2\pi u_T^2)^{3/2}} \exp(-\Delta^2/2u_T^2) \quad (3)$$

where  $u_T$  denotes the root-mean-square amplitude of the thermal vibrations. The values of  $u_T$  for a number of crystals are summarized in [49].

By introducing unrealistically large value of  $u_T$  (for example, exceeding the lattice constants) it is possible to consider large random displacements. As a result, the amorphous medium can be generated.

The trajectory of a particle entering the initially constructed crystal at the instant  $t = 0$  is calculated by integrating equations (1). Initial transverse coordinates,  $(x_0, y_0)$ , and velocities,  $(v_{x,0}, v_{y,0})$ , are generated randomly accounting for the conditions at the crystal entrance (i.e., the crystal orientation and beam emittance). A particular feature of MBN EXPLORER is in simulating the crystalline environment "on the fly", i.e. in the course of propagating the projectile. This is achieved by introducing a *dynamic simulation box* which moves following the particle (see Refs. [12, 15] for the details).

The important methodological issue concerns formulation of a criterion for distinguishing between channeling and non-channeling regimes of projectiles' motion. Depending on theoretical approach used to describe interaction of a projectile with a crystalline environment, the criterion can be introduced in different ways. For example,

within the continuous potential framework [14] the transverse and longitudinal motions of the projectile are decoupled. As a result, it is straightforward to define the channeling projectiles as those with transverse energies  $\varepsilon_{\perp}$  less than the height  $\Delta U$  of the interplanar (or, inter-axial) potential barrier, see Fig. 2left). Within this framework, the *acceptance*  $\mathcal{A}$  is determined at the entrance to the crystal and can be defined as the ratio of the number of particles with  $\varepsilon_{\perp} < \Delta U$  to the total number of particles.

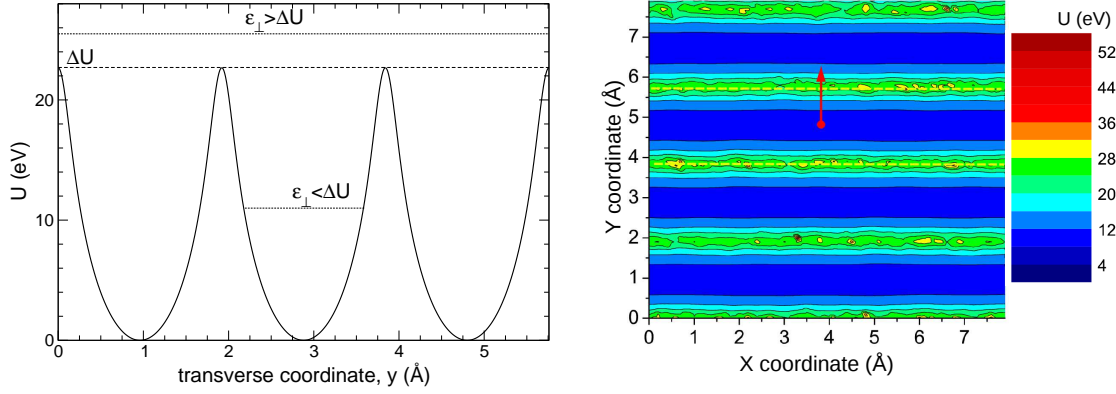


**Figure 2.** *Left.* Continuous interplanar Si(110) potential  $U(y)$  for a positron calculated in the Molière approximation at  $T = 300$  K. The coordinate  $y$  is measured along the  $\langle 110 \rangle$  axial direction. The channeling regime corresponds to the transverse energies  $\varepsilon_{\perp} < \Delta U$ . *Right.* The positron potential in Si(110) calculated following Eq. (2) as a sum of individual atomic potentials with account for thermal vibrations of the atoms. The red arrow is aligned with the  $\langle 110 \rangle$  direction.

Within the framework of molecular dynamics, the simulations are based on solving the EM (1) accounting, as in reality, for the interaction of a projectile with individual atoms of the crystal. The potential  $U(\mathbf{r})$  (2) experienced by the projectile varies rapidly in the course of the motion (see Fig. 2 right) coupling the transverse and longitudinal degrees of freedom. Therefore, other criterion must be provided to identify the channeling segments in the projectile's trajectory. To distinguish the channeling segments we employ a kinematic criterion introduced in Refs. [15, 18]. For a particular case of planar channeling the criterion as follows: a particle is considered to be moving in the channeling mode if the sign of its transverse velocity  $v_y$  (normal to the planar direction) has been changed at least two times inside the same channel. This corresponds to at least one full oscillation executed by the particle. The criterion must be supplemented by geometrical definition of the channels. In the case of straight crystals the positron channels are the volume areas restricted by the neighboring planes, whereas the electron channels are the areas between the corresponding neighboring mid-planes. For bent and periodically bent crystals this definition is modified accordingly.

It was noted however [50] that this criterion is not perfect in a sense that it leads to some artificial features in the evolution of the fraction of channeling particles with the penetration distance, see Section 3.2.



### 3.2. Statistical analysis of trajectories

Taking into account randomness in sampling the incoming projectiles and in positions of the lattice atoms due to the thermal fluctuations, one concludes that each simulated trajectory corresponds to a unique crystalline environment. Thus, all simulated trajectories are statistically independent and can be analyzed further to quantify the channeling process as well as the emitted radiation.

Figure 3 shows two simulated trajectories of 10 GeV electrons which enter straight oriented diamond crystal along the (110) crystallographic planes. Dashed horizontal lines in Fig. 3 mark the cross section of the (110) crystallographic planes separated by the distance  $d = 1.26 \text{ \AA}$ . Thus, the  $y$ -axis is aligned with the  $\langle 110 \rangle$  crystallographic axis. The horizontal  $z$ -axis corresponds to the direction of the incoming particles. To avoid the axial channeling, the  $z$ -axis was chosen along the  $[10, -10, 1]$  crystallographic direction. A projectile enters the crystal at  $z = 0$  and exits at  $z = L$ . The crystal is considered infinitely large in the  $x$  and  $y$  directions. In the simulations, the integration of the equations of motion (1) produces a 3D trajectory. The curves shown in the figure represent the projections of the corresponding 3D trajectories on the  $(yz)$  plane.

These exemplary trajectories illustrate a variety of features which characterize the motion of a charged projectile in an oriented crystal: the channeling motion, the over-barrier motion, the dechanneling and the rechanneling processes, rare events of hard collisions. Apart from providing the possibility of illustrative comparison, the simulated trajectories allow one to quantify the channeling process in terms of several parameters and functional dependencies which can be generated on the basis of statistical analysis of the trajectories [12, 15, 32–34, 36, 38, 40].

Randomization of the "entrance conditions" leads to different chain of scattering events for the different projectiles at the entrance to the bulk. As a result, not all trajectories start with the channeling segments. In Fig. 3, trajectory (a) refers to an accepted projectile that changes the direction of transverse motion more than two times while moving in the same channel. In contrast, trajectory (b) corresponds to the non-accepted projectile. To quantify this feature we define acceptance as the ratio

$$\mathcal{A} = \frac{N_{\text{acc}}}{N_0} \quad (4)$$

where  $N_{\text{acc}}$  stands for the number of accepted particles and  $N_0$  is the total number of the incident particles. The non-accepted particles experience unrestricted over-barrier motion at the entrance but can rechannel at some distance  $z$ .

As defined, acceptance depends on the beam emittance, on the type of the crystal and the channel, and on the bending radius. In a bent crystal, the channeling condition [51] implies that the centrifugal force  $F_{\text{cf}} = pv/R \approx \varepsilon/R$ , acting on the particle in the co-moving frame ( $R$  stands for the bending radius) is smaller than the maximum interplanar force  $F_{\text{max}}$ . It is convenient to quantify this statement by introducing the dimensionless *bending parameter*  $C$ :

$$C = \frac{F_{\text{cf}}}{F_{\text{max}}} = \frac{\varepsilon}{RF_{\text{max}}} = \frac{R_c}{R}. \quad (5)$$

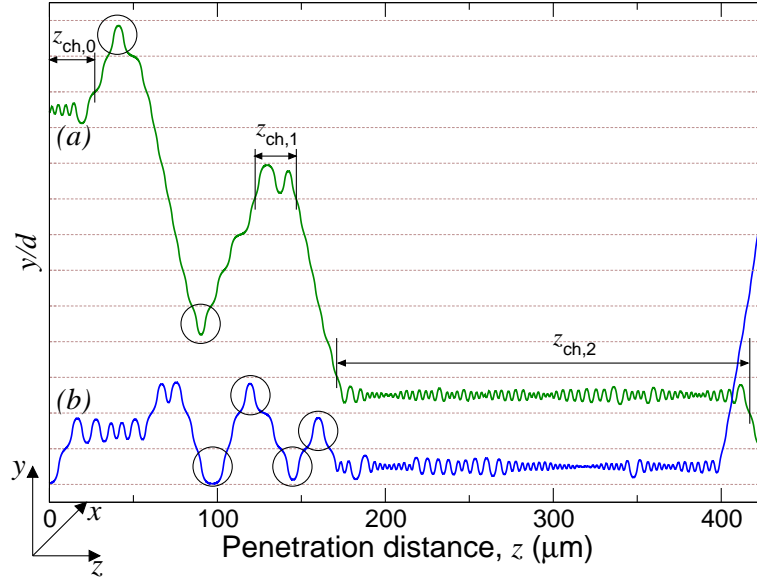


**Figure 3.** Selected simulated trajectories of 10 GeV electrons propagating in straight oriented diamond(110) crystal. The trajectories illustrate the channeling and the over-barrier motion as well as the dechanneling and rechanneling effects. The  $z$ -axis of the reference frame is directed along the incoming projectiles, the  $(xz)$ -plane is parallel to the (110) crystallographic planes (dashed lines) and the  $y$ -axis is perpendicular to the planes. The diamond(110) interplanar distance is  $d = 1.26$  Å. For the accepted trajectory (a) the characteristic lengths of the channeling motion are indicated: the initial channeling segment,  $z_{ch,0}$ , and channeling segments in the bulk,  $z_{ch,1}$  and  $z_{ch,2}$ . The non-accepted trajectory (b) corresponds to  $z_{ch,0} = 0$ . Encircled are the parts of trajectories that do not satisfy the criterion adopted for the definition of the channeling mode: the projectile stays in the same channel but changes the direction of the transverse motion only once.

The case  $C = 0$  ( $R = \infty$ ) characterizes the straight crystal whereas  $C = 1$  corresponds to the critical (minimum) bending radius  $R_c = \varepsilon/F_{\max}$  [51]. Within the framework of the continuous interplanar potential model, one can calculate  $F_{\max}$  by means of the formulae presented in Appendix A.3.

Figure 4 shows acceptance as a function of the bending parameter  $C$  for 855 MeV electrons channeling in several oriented crystals as indicated. The symbols mark the data that were obtained by statistical analysis of the simulated trajectories. For each crystal, the corresponding values of bending radius can be calculated from Eq. (5) using the following values of  $F_{\max}$  calculated in the Molière approximation and at room temperature: 7.0, 5.7, 10.0, and 42.9 GeV/cm for diamond, silicon, germanium, and tungsten, respectively.

An accepted projectile, stays in the channeling mode of motion over some interval  $z_{ch,0}$  until an event of the dechanneling (if it happens). The initial channeling segment is explicitly indicated for trajectory (a). For the non-accepted particle this segment is absent,  $z_{ch,0} = 0$ . To quantify the dechanneling effect for the accepted particles, one can introduce the *penetration length*  $L_p$  [15] defined as the arithmetic mean of the initial

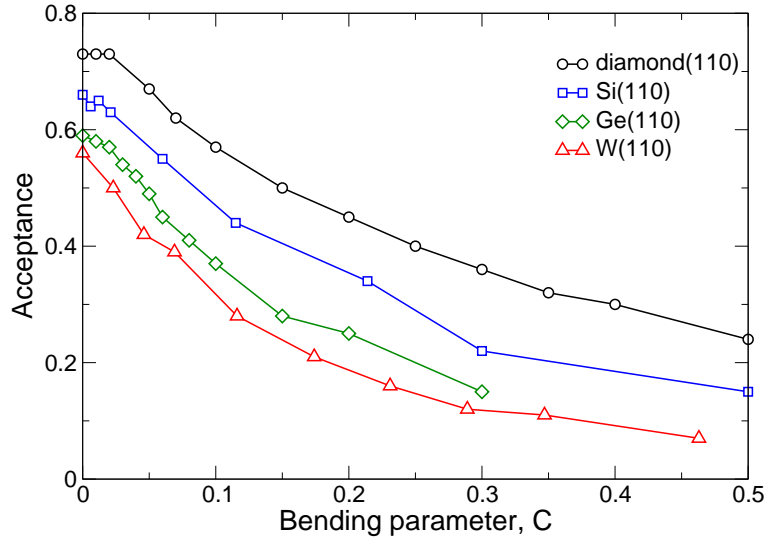


**Figure 4.** Acceptance versus bending parameter  $C$  (see Eq. (5)) for 855 MeV electrons. The presented data, obtained by means of means of MBN EXPLORER, are take from: Ref. [38] for diamond(110), Refs. [33, 34] for Si(110), Ref. [37] for Ge(110), and [42] for W(110).

channeling segments  $z_{\text{ch},0}$  calculated with respect to all accepted trajectories:

$$L_p = \frac{\sum_{j=1}^{N_{\text{acc}}} z_{\text{ch},0}^{(j)}}{N_{\text{acc}}}. \quad (6)$$

For sufficiently thick crystals the penetration length approaches the so-called dechanneling length  $L_d$  that characterizes the decrease of the fraction of channeling particles in terms of the exponential decay law,  $\propto \exp(-z/L_d)$  [52]. The concept of exponential decay has been widely exploited to estimate the dechanneling-channeling lengths for various ultra-relativistic projectiles in straight and bent crystals [53–61]. To derive the *approximate* relationship between the dechanneling length, which does not depend on the crystal thickness, and the penetration length, the value of which depends on  $L$ , one assumes that the exponential decay law is applicable at any distance  $z$  in the crystal. Then, calculating the penetration length as the mean value of the channeling segment in the crystal of thickness  $L$  one obtains:

$$L_p = L_d (1 - e^{-L/L_d}). \quad (7)$$

It is seen, that for any finite thickness  $L$  the value of  $L_p$ , calculated from statistical analysis of the simulated trajectories, is smaller the dechanneling lengths defined within the framework of the diffusion approximation to the dechanneling process [52]. The transcendent Eq. (7) can be easily solved numerically with respect to  $L_d$  for any given values  $L_p$  and  $L$  used in the simulations. The solution becomes trivial in the limit of a thick crystal,  $L \gg L_p, L_d$ , when the exponential term on the right-hand side can be omitted producing  $L_d \approx L_p$ .

Random scattering of the projectiles on the crystal atoms can result in the rechanneling, i.e. the process of capturing the particles into the channeling mode of

**Table 1.** Acceptance  $\mathcal{A}$ , penetration length  $L_p$ , total channeling length  $L_{ch}$  (both in microns) for 855 MeV electrons in straight ( $C = 0$ ) and bent ( $C > 0$ ) germanium (110) and (111) channels [37]. The last column shows the dechanneling lengths measured experimentally at the MAInz MIcrotron (MAMI) facility [61].

$C$	$\mathcal{A}$	(110)		$\mathcal{A}$	$L_p$	(111)		$L_d$ (exp.)
		$L_p$	$L_{ch}$			$L_{ch}$		
0.00	0.59	$6.6 \pm 0.3$	$18.1 \pm 0.7$	0.45	$10.6 \pm 0.5$	$20.6 \pm 0.8$		
0.01	0.58	$6.5 \pm 0.3$	$16.0 \pm 0.7$	0.42	$10.3 \pm 0.6$	$18.4 \pm 0.9$		
0.02	0.57	$6.3 \pm 0.3$	$11.6 \pm 0.6$	0.42	$10.1 \pm 0.5$	$14.9 \pm 0.9$		
0.03	0.54	$6.1 \pm 0.3$	$9.1 \pm 0.5$	0.38	$9.9 \pm 0.5$	$12.4 \pm 0.9$		
0.04	0.52	$5.9 \pm 0.3$	$7.6 \pm 0.5$	0.36	$9.7 \pm 0.6$	$11.0 \pm 1.0$		
0.05	0.49	$5.7 \pm 0.3$	$6.9 \pm 0.4$	0.32	$9.5 \pm 0.5$	$10.4 \pm 1.1$	$9 \pm 5$	
0.06	0.45	$5.4 \pm 0.3$	$6.2 \pm 0.6$	0.29	$9.2 \pm 0.5$	$9.6 \pm 1.1$		
0.08	0.41	$5.2 \pm 0.3$	$5.5 \pm 0.5$	0.22	$9.0 \pm 0.6$	$9.1 \pm 1.9$	$7.3 \pm 1.2$	
0.10	0.37	$4.8 \pm 0.3$	$5.0 \pm 0.5$	0.14	$7.9 \pm 0.7$	$7.7 \pm 2.8$	$5.9 \pm 1.5$	
0.15	0.28	$4.0 \pm 0.3$	$4.1 \pm 0.7$					
0.20	0.25	$3.5 \pm 0.2$	$3.5 \pm 0.7$					

motion. In a sufficiently long crystal, the projectiles can experience dechanneling and rechanneling several times in the course of propagation, as it is illustrated by both trajectories in Fig. 3. These multiple events can be quantified by introducing the *total channeling length*  $L_{ch}$ , which characterizes the channeling process in the whole crystal. The total channeling length  $L_{ch}$  per particle is calculated by averaging the sums of all channeling segments  $z_{ch0} + z_{ch1} + z_{ch2} + \dots$ , calculated for each trajectory, over all trajectories.

The results on the acceptance and the characteristic lengths are presented in Table 1 [37]. All the data refer to zero emittance 855 MeV electrons beams entering a  $L = 75$  microns thick germanium (110) and (111) crystals. Statistical uncertainties due to the finite numbers of the simulated trajectories correspond to the 99.9% confidence level. Also shown are the data on  $L_d$  measured in the recent experiment [61]. As mentioned above, for  $L \gg L_p$  the value of  $L_p$  obtained in the simulations equals to the dechanneling length, which determines the exponential decay of the channeling fraction. Comparing the data from the last column with that for  $L_p$  we state very good agreement between our theory and the experiment.

To further quantify the impact of the rechanneling effect basing on the information which can be extracted from the simulated trajectories, one can compute the channeling fractions  $f_{ch,0}(z) = N_{ch,0}(z)/N_{acc}$  and  $f_{ch}(z) = N_{ch}(z)/N_{acc}$  [15,33]. Here  $N_{ch,0}(z)$  stands for the number of particles that propagate in the same channel where they were accepted up to the distance  $z$  where they dechannel. The second quantity,  $N_{ch}$ , is the total number of particles which are in the channeling mode at the distance  $z$ .

As  $z$  increases the fraction  $\xi_{ch0}(z)$  decreases due to the dechanneling of the accepted particles. In the contrast, the fraction  $\xi_{ch}(z)$  can increase with  $z$  when the particles, including those not accepted at the entrance, can be captured in the channeling mode in

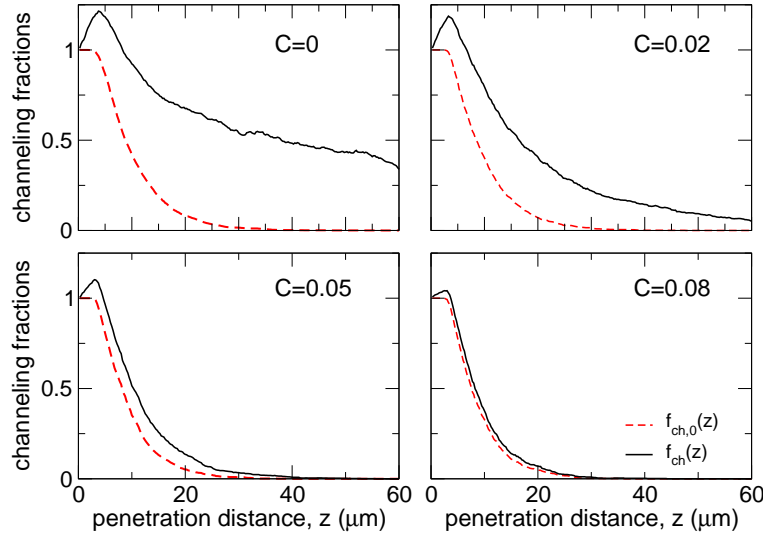


**Figure 5.** Channeling fractions  $f_{ch0}(z)$  (dashed curves) and  $f_{ch}(z)$  (solid curves) calculated for 855 MeV electrons in straight ( $C = 0$ ) and bent ( $C > 0$ ) Ge(110) channels. Ref. [37].

the course of the rechanneling. These dependencies for a 855 MeV electron channeling in straight and bent germanium(110) channels are presented in Fig. 5.

A striking difference in the behaviour of the two fractions as functions of the penetration distance  $z$  is mostly pronounced for the straight channel. Away from the entrance point, the fraction  $f_{ch0}(z)$  (dashed curve) follows approximately the exponential decay law (see discussion below). At large distances, the fraction  $f_{ch}(z)$  (solid curve), which accounts for the rechanneling process, decreases much slower following the power law,  $f_{ch}(z) \propto z^{-1/2}$  [18]. As the bending curvature increases,  $C \propto 1/R$ , the rechanneling events become rarer, and the difference between two fractions decreases. For  $C \gtrsim 0.1$  both curves virtually coincide. We note here that the impact of rechanneling was also highlighted by other authors in connection with the experimental studies with both straight [54] and bent [57] crystals.

Let us present simple analytical fits for both channeling fractions. The parameters, which enter the fitting formulae, can be related to those which are used to quantify the dechanneling process within the framework of the diffusion theory of dechanneling process (see, e.g., [56]).

Apart from the some interval  $[0, z_0]$  at the crystal entrance, the primary channeling fraction,  $f_{ch,0}(z)$ , can be approximated by the exponential decay law:

$$\tilde{f}_{ch,0}(z) = e^{-(z-z_0)/L_d}, \quad (8)$$

where  $z_0$  and  $L_d$  are fitting parameters. The parameter  $z_0 > 0$  appears due to the aforementioned criterion used to identify the accepted particles: the initial segment of each trajectories is analyzed to decide whether the particle moves in the channeling

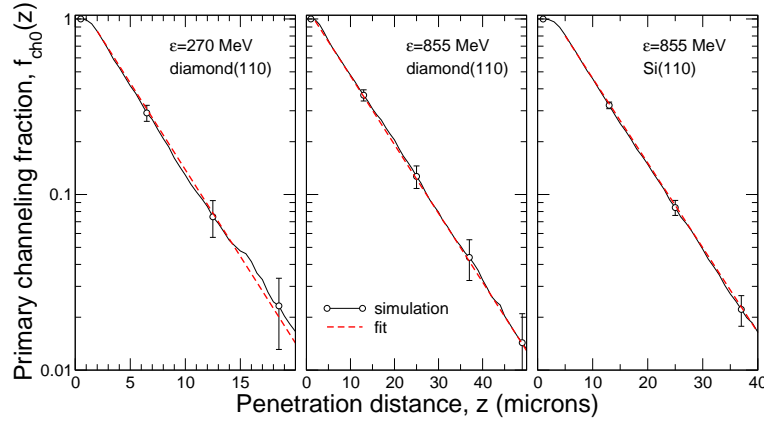


**Figure 6.** Primary channeling fraction  $f_{ch,0}(z)$  versus penetration distance for 270 and 855 MeV electrons in, correspondingly, 300 and 140 microns thick diamond(110) crystal (left and middle graphs), and for 855 MeV electrons in 500 microns thick Si(110) (right). Solid curves with open circles and error bars stand for the simulated data. Red dashed curves correspond to the fit (8). With account for statistical uncertainties the intervals for the fitting parameter  $z_0$  and  $\lambda$  are (from left to right):  $z_0 = (1.42 \pm 0.05)$ ,  $(1.7 \pm 0.1)$ ,  $(3.0 \pm 0.1)$  microns and  $L_d = (4.4 \pm 0.1)$ ,  $(11.14 \pm 0.14)$ ,  $(9.0 \pm 0.1)$  microns.

mode. Then, the penetration distance  $L_p$  is written as follows:

$$L_p = z_0 + \int_{z_0}^L (z - z_0) \tilde{f}_{ch,0}(z) \frac{dz}{L_d} + (L - z_0) \tilde{f}_{ch,0}(L).$$

Here, the integral term is due to the particles that dechannel at some distance  $z \in [z_0, L]$  inside the crystal while the last, non-integral term accounts for the particles that travel the whole distance  $L$  in the channeling regime. Carrying out the integration one derives

$$L_p = z_0 + L_d (1 - e^{-(L-z_0)/L_d}). \quad (9)$$

Figure 6 compares the simulated  $f_{ch,0}(z)$  (solid curves with symbols) and approximate  $\tilde{f}_{ch,0}(z)$  (dashed curves) dependences for  $\varepsilon = 270$  and 855 MeV electron channeling in diamond(110) and silicon(110) crystals. The values of the fitting parameters are indicated in the caption.

To derive the fitting formula for the channeling fraction  $f_{ch}(z)$ , which accounts for the re-channeling, one can utilize the approximation based on the one-dimension diffusion equation for the density of channeling particles,  $\rho(\theta, z)$ , as a function of penetration distance and the angle  $\theta$  with respect to the planar channel centerline:

$$\frac{\partial \rho}{\partial z} = D \frac{\partial^2 \rho}{\partial \theta^2}. \quad (10)$$

The diffusion coefficient  $D$ , which is assumed to be independent on  $\theta$  and  $z$ . Imposing the initial and boundary conditions as  $\rho(\theta, 0) = \delta(\theta)$  and  $\rho(\pm\infty, z) = 0$  one writes the



solution of Eq. (10) ‡

$$\rho(\theta, z) = \frac{1}{\sqrt{4\pi Dz}} \exp\left(-\frac{\theta^2}{4Dz}\right). \quad (11)$$

The channeling fraction is calculated as follows

$$f_{\text{ch}}(z) = \int_{-\theta_L}^{\theta_L} \rho(\theta, z) d\theta = \text{erf}\left(\frac{\theta_L}{\sqrt{4Dz}}\right) \quad (12)$$

where  $\theta_L$  is Lindhard's critical angle and  $\text{erf}(\cdot)$  stands for the error function.

To get initial values of the parameters entering the right-hand-side of (12) one estimates the critical angle as  $\Theta_L = \sqrt{2U_0/\varepsilon}$  with  $U_0$  standing for the depth of the continuous interplanar potential well. The diffusion coefficient  $D$  can be related the rms angle of multiple scattering  $\langle\theta^2\rangle(z)$ :

$$D = \frac{\langle\theta^2\rangle}{2z}. \quad (13)$$

For estimation purposes one can use the following formula [62]:

$$\langle\theta^2\rangle = \left(\frac{10.6(\text{MeV})}{\varepsilon(\text{MeV})}\right)^2 \frac{z}{L_{\text{rad}}} \quad (14)$$

where  $L_{\text{rad}}$  is the radiation length. It was argued in the cited paper that the factor 10.6 (MeV) provides a more accurate approximation in the limit of small penetration distances,  $z \ll L_{\text{rad}}$ , whereas a conventional value of 13.6 (MeV) (see, e.g., [63]) is applicable for  $z \gtrsim L_{\text{rad}}$ . Utilizing Eq. (33.20) from Ref. [63]) one obtains the following values of  $L_{\text{rad}}$  for amorphous carbon, silicon and germanium media: 12.2, 9.47 and 2.36 cm. This values are much larger than thickness of crystals used in channeling experiments with electrons and positrons.

Using (13) and (14) one derives the following fitting formula for the channeling fraction

$$\tilde{f}_{\text{ch}}(z) = \text{erf}\left(A\sqrt{\frac{\varepsilon}{z}}\right). \quad (15)$$

Within the model described above the parameter  $A$  is written as follows  $A = (L_{\text{rad}}U_0)^{1/2}/106$  (with  $L_{\text{rad}}$ ,  $U_0$ ,  $\varepsilon$  and  $\varepsilon$  measured in cm, eV, MeV, and microns, correspondingly). The calculated value can be used as the initial guess for the best fit to the  $f_{\text{ch}}(z)$  obtained from numerical simulations.

Note that for sufficiently large penetration distances  $\text{erf}\left(A\sqrt{\varepsilon/z}\right) \propto z^{-1/2}$ .

Figure 7 shows three case studies which illustrate the applicability of the fitting formula (15). Solid curves with symbols present the dependences  $f_{\text{ch}}(z)$  obtained from simulation of  $\varepsilon = 270$  and 855 MeV electron channeling in diamond(110) and silicon(110) crystals. The dashed curves stand for the fits with parameter  $A$  (in  $(\text{micron}/\text{eV})^{1/2}$ ) indicated in the legend and in the caption as well.

‡ The initial condition and the solution are written for the case of ideally collimated beam. For a non-collimated beam one carries out the substitution  $2Dz \rightarrow 2Dz + \theta_0^2$ , where  $\theta_0^2$  is the beam divergence at the crystal entrance

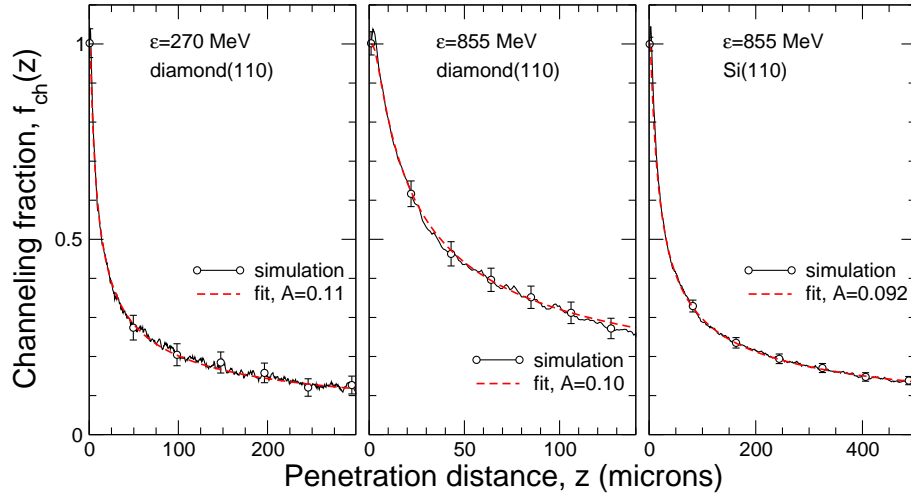


**Figure 7.** Channeling fraction  $f_{ch}(z) = N_{ch}(z)/N_{acc}$  versus penetration distance for 270 and 855 MeV electrons in, correspondingly, 300 and 140 microns thick diamond(110) crystal (left and middle graphs), and for 855 MeV electrons in 500 microns thick Si(110) (right). Solid curves with open circles and error bars stand for the simulated data. Red dashed curves correspond to the fit (15). With account for statistical uncertainties the intervals for the fitting parameter  $A$  are (from left to right):  $A = (0.11 \pm 0.07)$ ,  $(0.10 \pm 0.5)$ , and  $(0.092 \pm 0.007)$  (micron/eV) $^{1/2}$ .

### 3.3. Calculation of spectral distribution of emitted radiation

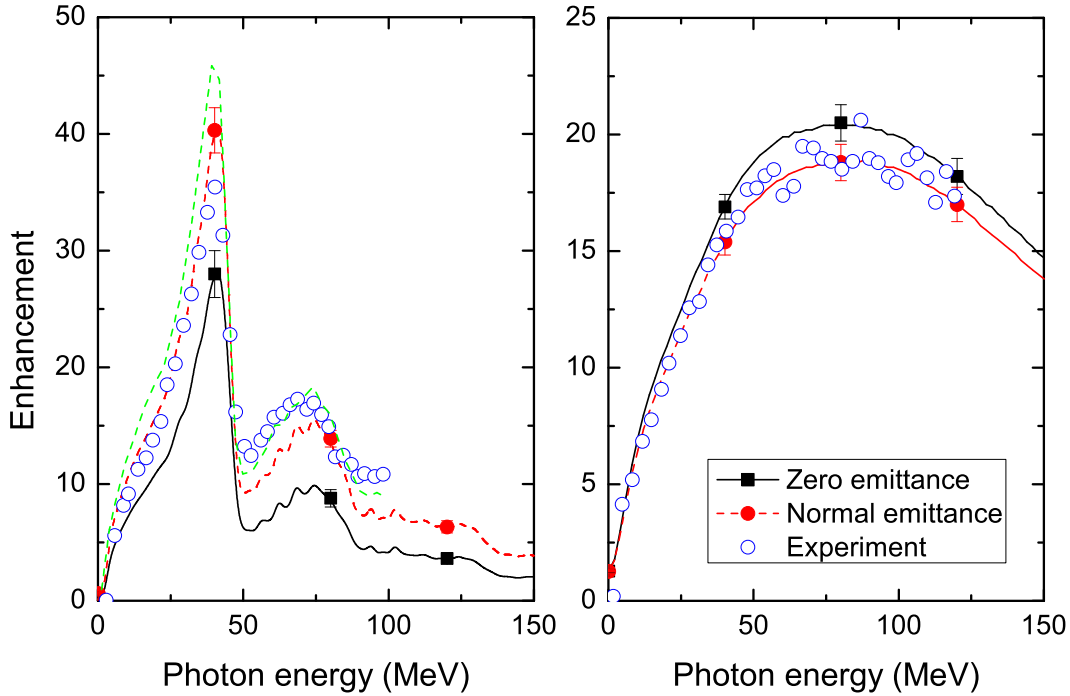
Spectral distribution of the energy emitted within the cone  $\theta \leq \theta_0 \ll 1$  with respect to the incident beam is computed numerically using the following formula:

$$\frac{dE(\theta \leq \theta_0)}{d\omega} = \frac{1}{N_0} \sum_{n=1}^{N_0} \int_0^{2\pi} d\phi \int_0^{\theta_0} \theta d\theta \frac{d^3 E_n}{d\omega d\Omega}. \quad (16)$$

Here,  $\omega$  is the radiation frequency,  $\Omega$  is the solid angle corresponding to the emission angles  $\theta$  and  $\phi$ . The quantity  $d^3 E_n/d\omega d\Omega$  stands for the spectral-angular distribution emitted by a particle that moves along the  $n$ th trajectory. The sum is carried out over *all* simulated trajectories, and thus it takes into account the contribution of the channeling segments of the trajectories as well as of those corresponding to the non-channeling regime.

The numerical procedures implemented in MBN EXPLORER to calculate the distributions  $d^3 E_n/d\omega d\Omega$  [15] are based on the quasi-classical formalism [23] that combines classical description of the particle's motion with the quantum corrections due to the radiative recoil quantified by the ratio  $\hbar\omega/\varepsilon$ . In the limit  $\hbar\omega/\varepsilon \ll 1$  the quasi-classical formula reduces to that known in classical electrodynamics (see, e.g., [64]). The classical description of the radiative process is adequate to characterize the emission spectra by electrons and positrons of the sub-GeV and GeV energy range (see, for example, [12] and references therein). The quantum corrections lead to strong modifications of the radiation spectra of multi-GeV projectiles channeling in bent and periodically bent crystals [35, 36, 38].

The calculated spectral intensity can be normalized to the Bethe-Heitler value (see, for example, Ref. [65]) and, thus, can be presented in the form of an enhancement factor over the bremsstrahlung spectrum in the corresponding amorphous medium.



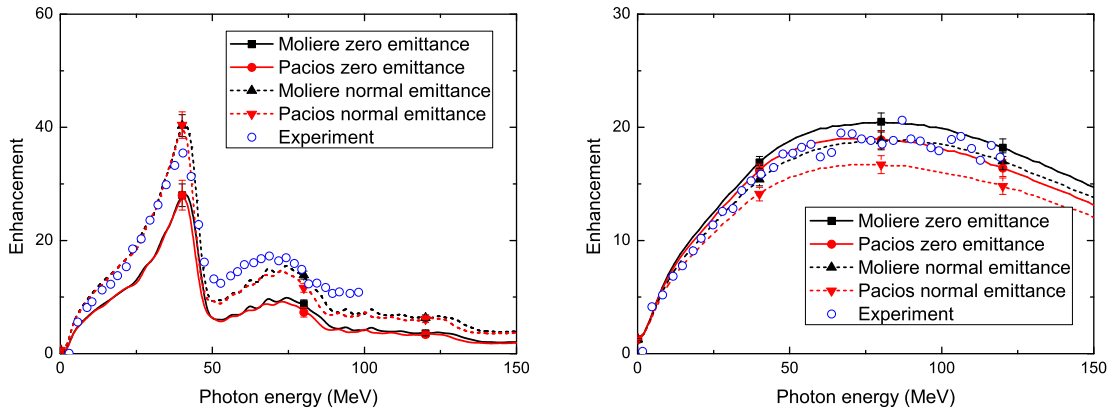
**Figure 8.** Enhancement factor of the channeling radiation over the Bethe-Heitler spectrum for 6.7 GeV positrons (left) and electrons (right) in straight Si(110) crystal. The experimental data, shown with open circles, are taken from Ref. [66] where the results of earlier experiments at CERN were quoted [67]. The calculations performed with MBN EXPLORER [15, 37] are shown with black solid curves, which present the results obtained for fully collimated beams (zero emittance), and red dashed curves, which correspond to the emittance of  $62 \mu\text{rad}$  as in the experiment. The symbols (closed circles and rectangles) mark a small fraction of the points and are drawn to illustrate typical statistical errors (due to a finite number of the trajectories simulated) in different parts of the spectrum. Green dashed curve, shown on the left figure, corresponds to the results presented in Ref. [68]. The data refer to the emission cone  $\theta_0 = 0.4 \text{ mrad}$ .

Figure 8 presents results of an exemplary case study of the emission spectra from 6.7 GeV positrons (left) and electrons (right) channeled in  $L = 105 \mu\text{m}$  thick oriented straight Si(110) crystal. The spectra were computed for the emission cone  $\theta_0 = 0.4 \text{ mrad}$  in accordance with the experimental setup [66]. This value exceeds the natural emission cone  $\gamma^{-1}$  by a factor of about five. Therefore, the calculated curves account for nearly all radiation emitted. Solid black and dashed red curves present the results of two sets of calculations carried out by means of MBN EXPLORER. The first set corresponds to the case of zero beam emittance, when the velocities of all projectiles at the crystal entrance are tangent to Si(110) plane, i.e. the incident angle  $\psi$  is zero [15]. The second set of trajectories was simulated allowing for the uniform distribution of the

incident angle within the interval  $\psi = [-\theta_L, \theta_L]$  with  $\theta_L = 62 \mu\text{rad}$  being Lindhard's critical angle. The calculated enhancement factors are compared with the experimental results presented in Ref. [66] and the results of numerical simulations for positrons from Ref. [68].

Figure 8 demonstrates that the simulated curves reproduce rather well the shape of the spectra and, in the case of the positron channeling, the positions of the main and the secondary peaks. With respect to the absolute values both calculated spectra,  $\psi = 0$  and  $|\psi| \leq \psi_L$ , exhibit some deviations from the experimental results. For positrons, the curve with  $\psi = 0$  perfectly matches the experimental data in vicinity of the main peak but underestimates the measured yield of the higher (the second) harmonic. Increase in the incident angle results in some overestimation of the main maximum but improves the agreement above  $\hbar\omega = 40 \text{ MeV}$ . For electrons, the  $\psi = 0$  curve exceeds the measured values, however, the increase in  $\psi$  leads to a very good agreement if one takes into account the statistical errors of the calculated dependence (indicated by symbols with error bars).

The aforementioned deviations can be due to several reasons.



**Figure 9.** Simulated (lines) versus experimental (open circles, Refs. [66, 67]) photon emission spectra for 6.7 GeV positrons (left) and electrons (right) in straight Si(110) crystal. The simulated spectra were obtained using (i) the Molière approximation (black curves) and (ii) the Pacios approximation (red curves) for atomic potentials. The results for zero emittance of the beam are shown with solid lines, the results for beam emittance  $\psi = \theta_L = 62 \mu\text{rad}$  are shown with dashed lines. Ref. [37].

First, the emission spectra can be sensitive to the choice of the approximation scheme used to describe the atomic potentials when constructing the crystalline field as a superposition of the atomic fields, Eq. (2). The results presented in Fig. 8 were obtained for the trajectories simulated within the Molière approximation framework. Though this approximation is a well-established and efficient approach, more realistic schemes for the crystalline fields, based, for example, on X-ray scattering factors [30, 69] or on accurate numerical approaches for calculation of the electron density in many-electron atoms [47], can also be employed for the channeling simulations. Figure 9 compares the experimentally measured spectra with those simulated numerically using the Molière and

the Pacios approximations for atomic potentials [37]. For positrons, both approximation result in virtually the same dependences. In the case of electrons, the spectra obtained with the Pacios potential are 5-10 per cent less intensive. Within the statistical errors both results are in a good agreement with the experimental measurements.

Another source of the discrepancies can be attributed to some uncertainties in the experimental set-up described in [66, 70]. In particular, it was indicated that the incident angles were in the interval  $[-\psi_L, \psi_L]$  with the value  $\psi_L = 62 \mu\text{rad}$  for a 6.7 GeV projectile. However, no clear details were provided on the beam emittance which becomes an important factor for comparing theory vs experiment. In the calculations a uniform distribution of the particles within the indicated interval of  $\psi$  was used, and this is also a source of the uncertainties. The spectra was also simulated for larger cutoff angle equal to  $2\psi_L$  (these curves are not presented in the figure). It resulted in a considerable ( $\approx 30 \%$ ) decrease of the positron spectrum in the vicinity of the first harmonic peak.

On the basis of the comparison with the experimental data it can be concluded that the code produces reliable results and can be further used to simulate the propagation of ultra-relativistic projectiles along with the emitted radiation. In the Paper below we present several case studies of the channeling phenomena and radiation emission from ultra-relativistic projectiles traveling in various crystalline environments, incl. linear, bent and periodically bent crystals as well as in crystals stacks. In most cases, the parameters used in the simulations, such as crystal orientation and thickness, the bending radii  $R$ , periods  $\lambda_u$  and amplitudes  $a$ , as well as the energies of the projectiles, have been chosen to match those used in past and ongoing experiments. Wherever available we compare results of our simulations with available experimental data and/or those obtained by means of other numerical calculations.

## 4. Case studies

In this section we present several case studies to modeling of ultra-relativistic projectiles (electrons, positron and negative pions) channeling and radiation emission by means of MBN EXPLORER. The case studies refer to the channeling in linear, bent and periodically bent oriented crystals. Wherever available the results of numerical simulations are compared with the experimental data or/and the results of calculations carried out by accompanying propagation of ultra-relativistic projectiles.

### 4.1. Channeling and radiation emission spectra in linear crystals

A case study presented in this section concerns comparative analysis of the channeling properties and spectral distribution of Channeling Radiation (ChR) of electrons and positrons in oriented graphite(002), diamond(110), silicon(110) and tungsten(110)  $L = 1$  mm thick linear crystals.

The choice of the crystalline targets is explained as follows. A silicon crystal, due to

its availability and high degree of purity of a crystalline structure, has been extensively used in the experiments carried out at various accelerator facilities starting from early days of the activity in the field up to nowadays, see e.g. [56, 59, 60, 71–75]. Diamond crystals (natural or/and synthesized [76]) has also been used in channeling experiments (e.g. [74, 77–79]). The use of a diamond crystal is preferential in the experiments with high-intensity particle beams (such as the FACET beam at SLAC [80]) since it bears no visible influence from being irradiated [81].

The technologies, available currently for preparing periodically bent crystals, do not immediately allow for lowering the values of bending period down to tens of microns range or even smaller keeping, simultaneously, the bending amplitude in the range of several angstroms. These ranges of  $a$  and  $\lambda_u$  are most favourable to achieve high intensity of radiation in a CU [12]. One of the potential options to lower the bending period is related to using crystals heavier than diamond and silicon to propagate ultra-relativistic electrons and positrons. In heavier crystals, both the depth,  $\Delta U \propto Z^{2/3}$ , of the interplanar potential and its the maximum gradient,  $U'_{\max} \propto Z^{2/3}$ , attain larger values, resulting in the enhancement of the critical channeling angle and reduction of the critical radius  $R_c \propto 1/U'_{\max}$  [51]. From this end, the tungsten crystal ( $Z = 74$ ) is a good candidate for the study since the critical radius for W(110) is 0.16 cm which is seven times smaller than that in Si(110). This allows one, at least in theory, to consider periodic bending with  $\lambda_u \lesssim 10 \mu\text{m}$ . This crystal was used in channeling experiments with both heavy [56, 82] and light [83, 84] ultra-relativistic projectiles. In Ref. [82] it was noted that the straight tungsten crystals show high structure perfection. This feature is also of a great importance for successful experimental realization of the CU idea [85].

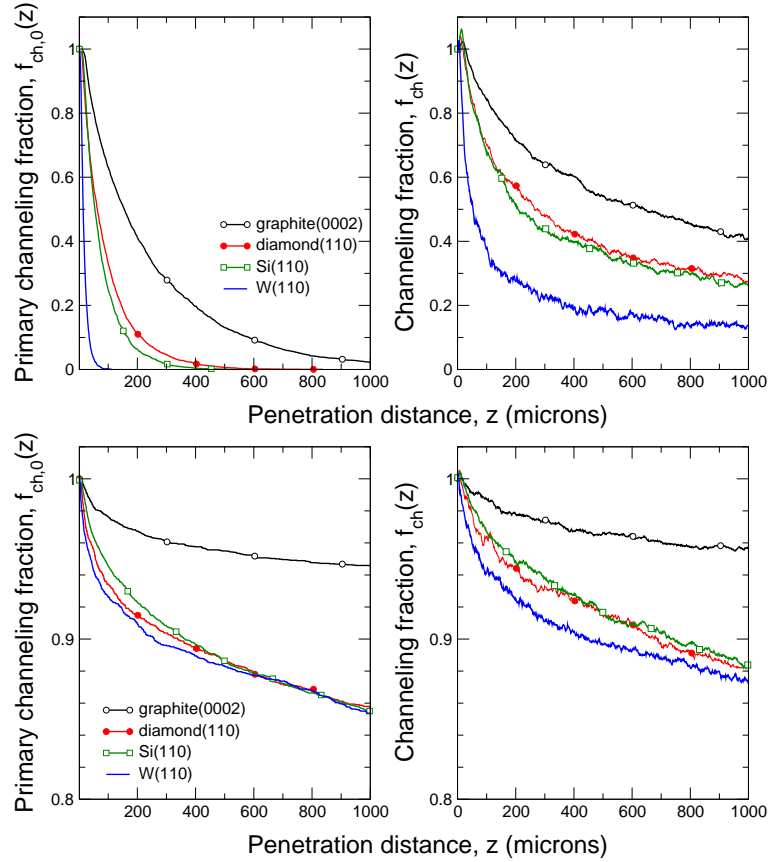
Finally, we have simulated electron and positron channeling in graphite (002). The channel is very wide (the interplanar distance  $d = 3.348 \text{ \AA}$ ) and this, together with low electron density inside the channel, provide excellent conditions for projectile to channel over very large distances. Although it is known that crystalline structure of graphite is spoiled due to high degree of mosaicity [86] the channeling experiments have been carried out with this material (see discussion in Ch. 4.7 in Ref. [87]).

Figure A4 in Section Appendix A.3 compares the continuous planar potentials for electrons and positrons in the four channels indicated. To be note is that cases of W(110) and graphite(002) can be considered as two extreme cases: of a very deep potential well (130 eV) for the former and of a very wide one for the latter.

MBN EXPLORER was used to simulate trajectories of 10 GeV projectiles and to compute the corresponding emission spectra. For each crystal, the number of simulated trajectories was  $N_0 \approx 4000$ . The choice of the incident beam energies was motivated by the planned (though not carried out) channeling experiments with 4...20 GeV electron and positron beams at the SLAC facility (USA).

Figure 10 shows the computed channeling fractions as functions of the penetration distance  $z$  measured along the incident beam. Let us point out that for both negatively and positively charged projectiles the channeling fractions calculated for graphite(002) are notably higher than for other channels presented. The values of the acceptance





**Figure 10.** Channeling fractions  $f_{ch,0}(z) = N_{ch,0}(z)/N_{acc}$  (left graphs) and  $f_{ch}(z) = N_{ch}(z)/N_{acc}$  (right graphs) of 10 GeV electrons (upper row) and positrons (lower row) versus the penetration distance  $z$  in different oriented crystals as indicated.

**Table 2.** Values of the acceptance  $\mathcal{A}$ , penetration length  $L_p$ , total length of the channeling segments  $L_{ch}$  calculated for  $\varepsilon = 10$  GeV electrons and positrons in  $L = 1000$   $\mu\text{m}$  thick Graphite(002), C(110), Si(110) and W(110).  $L_{d,est}$  indicates the estimated values of the dechanneling length.

Crystal	$\mathcal{A}$	Electrons			$\mathcal{A}$	Positrons	
		$L_p$ ( $\mu\text{m}$ )	$L_{d,est}$ ( $\mu\text{m}$ )	$L_{ch}$ ( $\mu\text{m}$ )		$L_p$ ( $\mu\text{m}$ )	$L_{d,est}$ ( $\mu\text{m}$ )
Graphite(002)	0.84	239 $\pm$ 14	1090	508 $\pm$ 16	0.99	993 $\pm$ 9	13 $\times$ 10 <sup>3</sup>
C(110)	0.77	94 $\pm$ 6	210	359 $\pm$ 14	0.97	925 $\pm$ 18	4970
Si(110)	0.72	77 $\pm$ 5	190	311 $\pm$ 12	0.98	928 $\pm$ 13	6060
W(110)	0.62	18 $\pm$ 1	43	144 $\pm$ 6	0.97	921 $\pm$ 18	4620

factor, Eq. (4), penetration length  $L_p$ , Eq. (6), and total channeling length  $L_{ch}$ , calculated from statistical analysis of the trajectories, are listed in Table 2. The quantity  $L_{d,est}$ , also indicated in the table, stands for the estimated value of the dechanneling length  $L_d$  calculated by approximating the fraction  $f_{ch,0}(z)$  of accepted projectiles with  $\exp(-z/L_d)$  at the penetration distances well away from the entrance point.

Spectral distributions of the emitted radiation are presented in the upper row in Fig. 11. For the sake of convenience, in the lower row of the figure we plot the spectral distribution of the enhancement factors over the Bether-Heitler spectra in corresponding amorphous media.

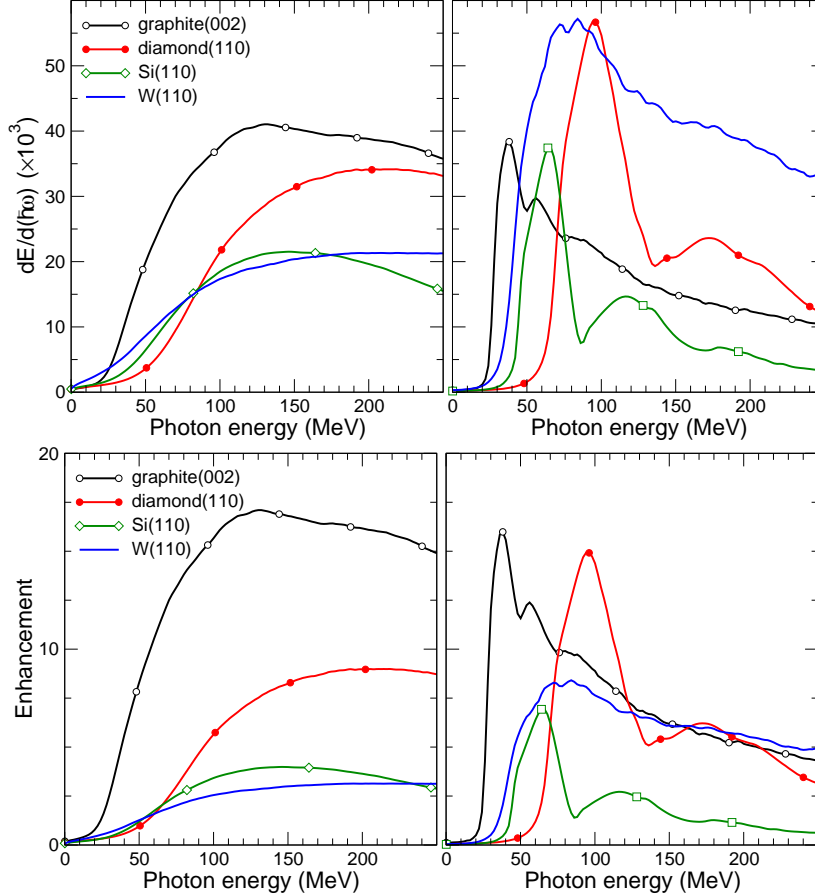


**Figure 11.** Spectral distribution of channeling radiation (upper row) and enhancement factor over the emission in the amorphous medium (lower row) calculated 10 GeV electrons (left column) and positrons (right column) channeled in different oriented crystals as indicated. The data refer to the emission angle  $\theta_0 = 1/\gamma \approx 0.05$  mrad.

#### 4.2. Channeling of negative pions in bent Si(110)

In Ref. [53] the dechanneling phenomenon of  $\varepsilon = 150$  GeV negative pions  $\pi^-$  in Si(110) oriented crystal has been experimentally investigated. In the experiment, the beam of pions was deflected due to channeling effect in the bent crystal, see illustrative left panel of Figure 12. The crystal thickness in the beam direction was  $L = 1.91$  mm, the bending radius  $R = 19.2$  m. The distribution of the beam particles with respect to the deflection angle  $\theta$  was measured, see open squares in Fig. 12 *right*. The dashed curve shows the fit to the experimental data [53]. The fit was obtained as follows. Two peaks in the distribution, the one at  $\theta = 0$  corresponding to the particles scattered at the

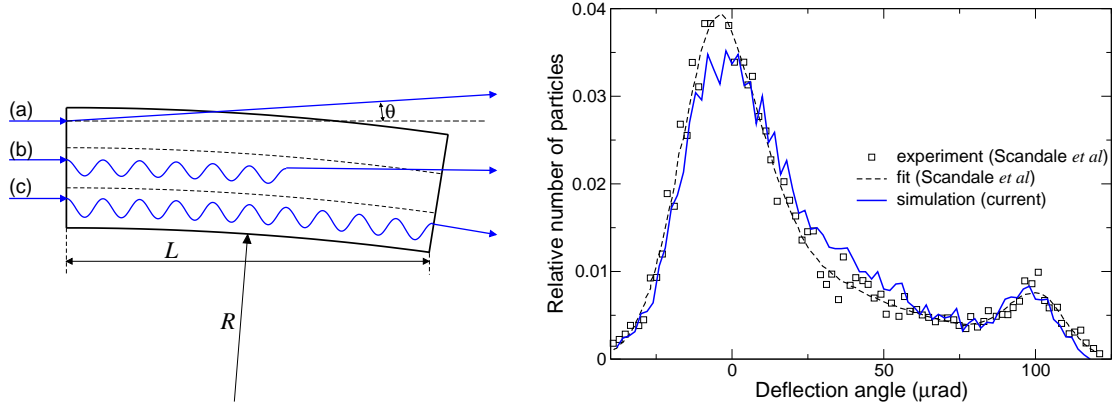


**Figure 12.** *Left.* Schematic picture of particles deflection by a bent crystal. Thick (blue) solid curves illustrate trajectories of the particles which dechannel at the crystal entrance, (a), dechannel somewhere inside the crystal, (b), propagate through the whole crystal, (c). The distribution of particles with respect to the deflection angle  $\theta$  can be measured in experiment. *Right.* Distribution of 150 GeV pions in bent  $L = 1.91$  mm oriented Si(110) crystal with respect to  $\theta$ . Symbols and dashed curve stand for the experimental data and its fit, correspondingly [53]. Solid curve - the current simulation.

crystal entrance and another one at  $\theta = L/R \approx 100 \mu\text{rad}$  due to the particles channeled through the whole crystal, were approximated with two gaussians. The data in between two peaks was fitted with the exponential decay function which provided a measure of the dechanneling length  $L_d$ .

Thick blue curve in Fig. 12 *right* shows the angular distribution derived from the analysis of ca  $12 \times 10^3$  trajectories simulated with the MBN EXPLORER software. Our result corresponds well to the experimental data. Some discrepancy seen can be attributed to (i) comparatively low statistics in both the simulation and the experiment (total number of counts is about 5000, as one can calculate using the data presented in Fig. 3 in [53]), (ii) uncertainty in the beam direction along the (110) plane. Our recent study shows the sensitivity of the angular distribution to this parameter [45].

The bending radius quoted above is much smaller than the critical radius  $R_c$  [51]. The latter can be estimated as  $R_c = \varepsilon/U'_{\text{max}} \approx 0.26$  m where  $U'_{\text{max}} = 5.7$  GeV/cm is the strength of the interplanar field in Si(110) calculated within the Molière approximation at  $T = 300$  K [12, 56]. Thus, the bending parameter is small,  $C = R_c/R = 0.013$ . As indicated in Ref. [53] "A slightly bent crystal ( $R \gg R_c \dots$ ) is the ideal choice to perform measurements of the dechanneling length".

In what follows we demonstrate that the value  $L_d = 0.92 \pm 0.05$  reported in [53] overestimates the dechanneling length defined as the factor in the exponential decay,  $\exp(-z/L_d)$ , of primarily channeled particles. In an experiment, the re-channeled particles cannot be separated from the primarily channeled ones. As a result, the dechanneling rate deduced from the experimental data is intrinsically increased due to the account for the re-channeled fraction. §

§ We note here that that the rechanneling contribution in the deflection efficiency of negative particles

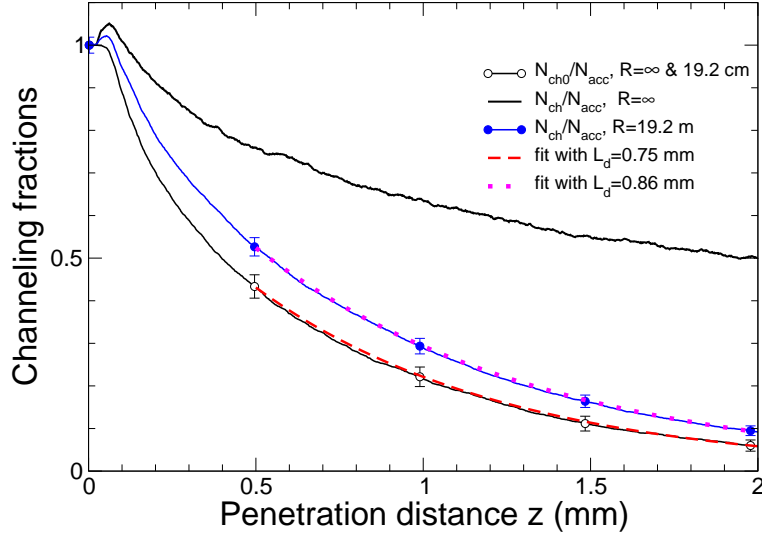


**Figure 13.** Fractions of the channeling negative pions in straight ( $R = \infty$ ) and bent ( $R = 19.2$  m) Si(110) as a function of the penetration distance  $z$ . The curve with open circles shows the primary fraction  $N_{ch,0}(z)/N_{acc}$  which is virtually identical for both straight and bent crystals. The curve with filled circles correspond to the fraction  $N_{ch}(z)/N_{acc}$  accounting for the re-channeling in the bent crystal. Error bars illustrate the statistical uncertainties due to the finite number of the trajectories simulated. For the sake of comparison, the fraction  $N_{ch}(z)/N_{acc}$  calculated for the straight crystal is also presented. Dashed and dotted curves show the exponential decay fits with the  $L_d$  values as indicated in the legend.

To quantify the decay rates of channeled negative pions with and without dechanneling, we have analyzed the fraction of primary channeled particles,  $N_{ch,0}(z)/N_{acc}$ , and the fraction  $N_{ch}(z)/N_{acc}$  which accounts for the re-channeling effect ( $N_{acc}$  stands for the number of accepted particles), see Fig. 13. Because of the large bending radius the primary fraction in the bent crystal coincides (within the statistical errors) with that calculated for the straight crystal ( $R = \infty$ ). Therefore, the curve  $N_{ch,0}(z)/N_{acc}$  in the figure refers to both cases. As it has been already mentioned, the excess due to re-channeling of the total number of channeling particles  $N_{ch}(z)$  over the the number the primary channeling ones  $N_{ch,0}(z)$  is the largest for a straight channel and rapidly decreases with  $R$ . This decrease is seen explicitly when one compares the curve without symbols (straight channel) and the curve with filled circles ( $R = 1.91$  m). Even so, the difference between the fractions in the bent channel results in the different values of the decay rates. In the region far away from the entrance point, both curves can be approximated with  $A \exp(-z/L_d)$ . For the primary fraction this fit (see the dashed curve) produces  $L_d = 0.75 \pm 0.02$  mm which is the dechanneling length associated with the decay rate of  $N_{ch,0}(z)$  in both the straight and the bent Si(110). The same approximation for  $N_{ch}(z)/N_{acc}$  (the dotted curve) results in larger values ( $0.86 \pm 0.02$ ) mm. This interval overlaps with the experimentally measured one [53].

has been accounted for in an earlier experiment with electrons, Ref. [57].

### 4.3. Simulation of emission spectra in bent crystals

The motion of a channeling particle in a bent crystal contains two components: the channeling oscillations and circular motion along the bent centerline. The latter motion gives rise to the synchrotron-type radiation (SR) [64]. Therefore, the total spectrum of radiation formed by a ultra-relativistic projectile propagating in the channeling mode in a bent crystal bears features of both the ChR and SR [88]. The peculiarities which appear in spectral and spectra-angular distributions of the emitted radiation due to the interference of the two mechanisms of radiation were analyzed in Refs. [89–93] by analytical and numerical means.

A quantitative analysis of the emission spectra based on the simulation with the MBN EXPLORER package has been carried out for sub-GeV electrons and positrons channeling in silicon [34], diamond [94] and tungsten [42] crystals. The emission spectra of 4...20 GeV projectiles in oriented bent Si(111) crystal have been presented in Ref. [36] and the corresponding illustrative examples are shown in Fig. 14.

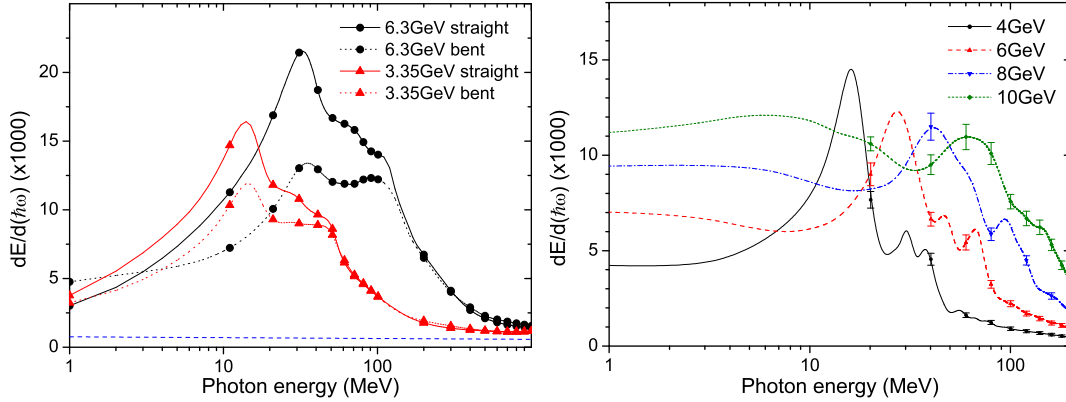


**Figure 14.** *Left.* Radiation spectra by 3.35 and 6.3 GeV electrons in straight and bent 60 micron thick Si(111). Broken line stands for the emission spectrum in amorphous silicon by the 3.35 GeV projectile calculated within the Bethe-Heitler approximation. Radiation spectra of 4...10 GeV positrons in bent Si(111). Ref. [36].

In Fig. 14*left*, comparing the solid curves, which show the intensity of radiation in the straight crystal, with the dashed ones, corresponding to the bent crystal, one notes lowering of the channeling radiation peaks due to the crystal bending. The synchrotron-type radiation, which is absent in the straight crystal, contributes to the low-energy part of the spectrum. It is clearly seen in the spectral dependences for a 6.3 GeV electron: in the photon energy range  $\hbar\omega = 1 \dots 3$  MeV the intensity in the bent crystal is higher than that in the straight one. The contribution of the synchrotron radiation to the emission spectrum becomes more pronounced for more energetic projectile, as it is illustrated by the right panel of the figure.

#### 4.4. Radiation from diamond-based CU by multi-GeV electrons and positrons

In Refs. [32] the results have been presented of the statistical analysis of the channeling properties and of the spectral intensities of the radiation formed by 195...855 MeV electrons and positrons in the crystalline undulator with the parameters used in the experiments at the MAMI facility [95, 96]. The CUs were manufactured in Aarhus University (Denmark) using the molecular beam epitaxy technology to produce strained-layer  $\text{Si}_{1-x}\text{Ge}_x$  superlattices with varying germanium content [97].

Later, similar calculations have been extended to the range of multi-GeV projectile energies [37, 98]. To a great extent, this activity was inspired by the plans to carry out channeling experiments with diamond crystals at the SLAC facility (USA) [80] using high-intensity 4...20 GeV electron and positron beams. The sets of simulations have been performed aiming at providing benchmark data for the emission spectra formed by projectile electrons and positrons in *silicon-based* [37] and *diamond-based* [98] crystalline undulators with the parameters similar to those used in the experiments with sub-GeV electron beams [95, 96].

The parameters of the CU used in the simulations were as follows:

- Bending period amplitude  $\lambda_u = 40$  microns.
- Number of periods  $N_u = 8$  corresponds to the crystal thickness  $L = N_u \lambda_u = 320$  microns.
- Bending period amplitude  $a = 2 \dots 6$  Å.

**Table 3.** Acceptance  $\mathcal{A}$  and penetration length  $L_p$  for 10 GeV positrons and electrons in straight ( $a = 0$ ) and periodically bent ( $\lambda_u = 40$  microns) planar channels Si(110). The bending parameter  $C = a(2\pi/\lambda_u)^2(\varepsilon/U'_{\max})$  stands for the ratio of the centrifugal force to the interplanar force.

Projectile	$a$ (Å)	$C$	$\mathcal{A}$ (%)	$L_p$ ( $\mu\text{m}$ )
positron	0	0	$97.1 \pm 0.9$	$302 \pm 4$
	2	0.08	$89.8 \pm 2.1$	$301 \pm 5$
	4	0.16	$81.6 \pm 2.6$	$287 \pm 7$
	6	0.24	$71.9 \pm 5.8$	$273 \pm 15$
electron	0	0.0	$65.8 \pm 2.3$	$82 \pm 4$
	4	0.16	$42.9 \pm 3.3$	$52 \pm 4$

Table 3 provides the values of acceptance and penetration length  $L_p$  obtained via statistical analysis of the trajectories simulated for 10 GeV electrons and positrons incident of straight ( $a = 0$ ) and periodically bent Si(110) crystal. In the latter case, the bending parameter  $C$  is defined as the ratio of the maximum values of the centrifugal force,  $F_{\text{cf}} \approx \varepsilon/R_{\min}$  with  $R_{\min} = a^{-1}(\lambda_u/2\pi)^2$ , and the interplanar force  $U'_{\max}$ . The latter was taken equal to 5.7 GeV/c, which corresponds to the (110) interplanar potential calculated within the Molière approximation at  $T = 300$  K. The data shown indicate



that most of positrons travel in the channeling mode through the whole crystal. For electrons, both acceptance and channeling segments length are much lower. These features reveal themselves in the emission spectra by the projectiles.

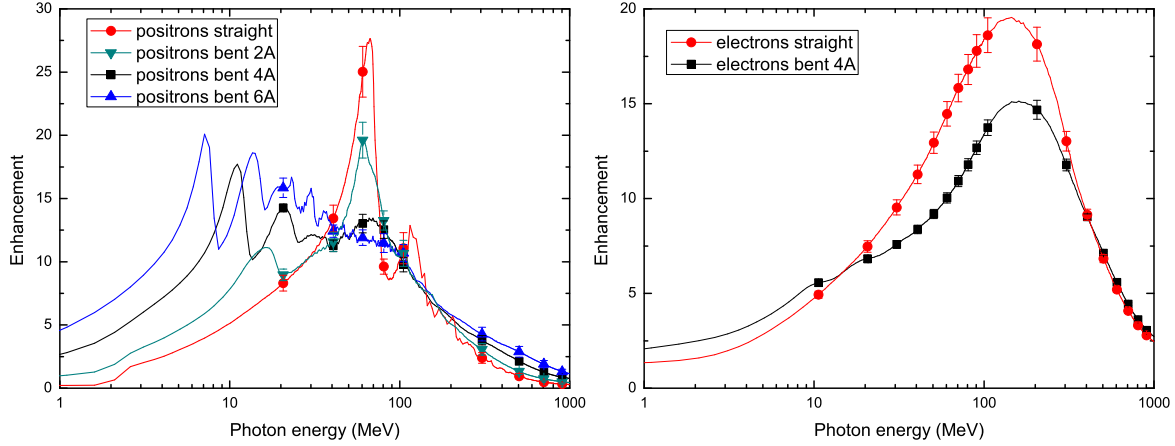


**Figure 15.** Enhancement factor of the radiation over the Bethe-Heitler spectrum for 10 GeV positrons (left) and electrons (right) positrons in straight Si(110) and in Si(110)-based CU with different bending amplitudes as indicated. The bending period is set to  $\lambda_u = 40$  microns. All curves refer to the emission angle  $\theta_0 = 7/\gamma \approx 0.36$  mrad.

Figure 15 shows the enhancement factor (over the Bethe-Heitler background) of the radiation emitted by positrons (left panel) and electrons (right panel) [37]. For both projectiles, the spectra in the straight channel (red curves) are dominated by powerful peaks due to the channeling radiation. The peak is more pronounced for positrons since their channeling oscillations are quasi-harmonic resulting in the emission within comparatively narrow bandwidth centered at  $\hbar\omega_{\text{ch}} \approx 70$  MeV. Strong anharmonicity of the electron channeling oscillation leads to the noticeable broadening of the peak with the maximum located at  $\hbar\omega_{\text{ch}} \approx 120$  MeV. Periodical bending of the crystal planes gives rise to the CUR Radiation (CUR). Since the dechanneling length of positrons greatly exceeds that of electrons, the CUR peaks in the positron spectra are much more pronounced. The energy  $\hbar\omega_1$  of the first harmonic of CUR can be estimated from the relation (see [12], Eq. (6.14)):

$$\hbar\omega_1 [\text{MeV}] = \frac{9.5}{1 + K^2/2} \frac{\varepsilon^2}{\lambda_u} \quad (17)$$

where  $\varepsilon$  is substituted in GeV and  $\lambda_u$  in microns. The quantity  $K$  stands for the total undulator parameter due to both channeling oscillations and those due to the bending periodicity [28]

$$K = \sqrt{K_u^2 + K_{\text{ch}}^2} \quad (18)$$

where  $K_u = 2\pi\gamma a/\lambda_u$  and  $K_{\text{ch}} \propto 2\pi\gamma a_{\text{ch}}/\lambda_{\text{ch}}$  with  $a_{\text{ch}} \leq d/2$  and  $\lambda_{\text{ch}}$  being the amplitude and period of channeling oscillations. In the case of positron channeling, assuming harmonicity of the oscillations one can derive the following expression for  $K_{\text{ch}}^2$  averaged

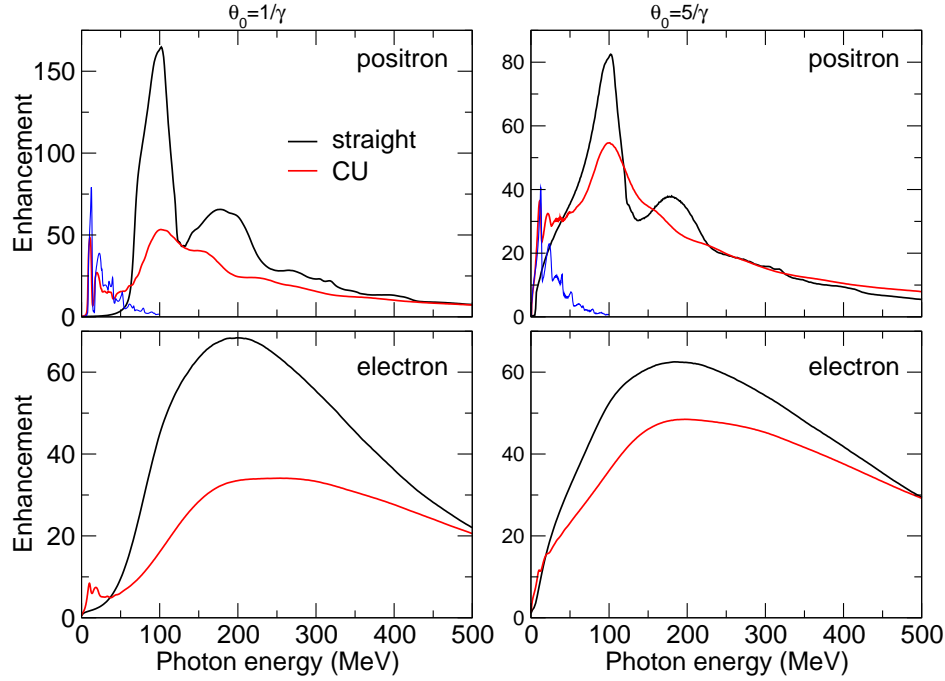


**Figure 16.** Enhancement factor of the radiation over the Bethe-Heitler spectrum for 10 GeV positrons (upper row) and electrons (lower row) positrons in straight diamond (thick black lines) and in diamond-based CU (thick red lines) with amplitude  $a = 4$  Å and period  $\lambda_u = 40$  microns. Thin blue solid lines show the emission spectra from ideal undulator with the same  $a$  and  $\lambda_u$ . Left column corresponds to the emission angle  $\theta_0 = 1/\gamma = 51.1$   $\mu\text{rad}$ ; right column – to  $\theta_0 = 5/\gamma \approx 256$   $\mu\text{rad}$ . All spectra refer to the crystal thickness  $L = 320$  microns.

over the allowed values of  $a_{\text{ch}}$  (see [12], Eq. (6.14)):

$$\langle K_{\text{ch}}^2 \rangle = \frac{2\gamma U_0}{3mc^2}. \quad (19)$$

where  $U_0$  is the depth of the interplanar potential well. For  $\varepsilon = 10$  GeV in Si(110) ( $U_0 \approx 22$  eV at  $T = 300$  K, see, e.g., Fig. A3) one obtains  $\langle K_{\text{ch}}^2 \rangle \approx 0.56$ .

Using (17)-(19) one estimates  $\hbar\omega_1$  for  $a = 2, 4, 6$  Å as 16, 11.7 and 8 MeV, respectively. These values correlate nicely with the positions of the first peaks of CUR seen in Fig. 15 left.

In Ref. [98] the channeling of 4...20 GeV electron and positron beams in oriented diamond(110) crystal, both straight and periodically bent, was simulated and analyzed. As mentioned, this activity has been carried out to produce theoretical benchmarks for the experimental measurements planned to be carried out at the SLAC facility. From this viewpoint, the use of diamond crystals looked preferential since diamond bears no visible influence from being irradiated by high-intensity beams available at SLAC.

The spectral distributions of radiated energy were computed for two values of the emission cone  $\theta_0$  (see Eq. (16)): (i) a 'narrow' cone  $\theta_0 = 1/\gamma$ , and (ii) a 'wide' cone  $\theta_0 = 5/\gamma$ , which collects virtually all radiation emitted by ultra-relativistic particles. The results of calculations for 10 GeV projectiles, presented in the form of

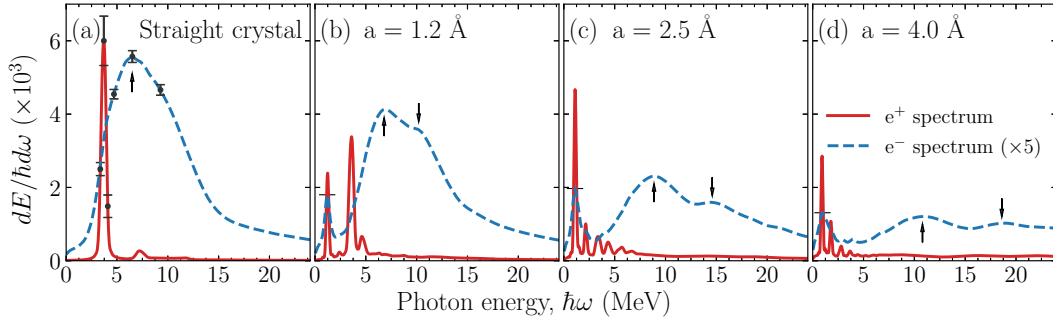


**Figure 17.** Spectral distributions of radiation by 855 MeV electrons (dashed blue curves, multiplied by a factor of 5) and positrons (solid red curves) in straight (a) and periodically bent (b)–(d) diamond (110) crystals. The upward arrows indicate the maxima of ChR for electrons, the downward arrows show the positions of the additional maxima appearing in the bent crystals (see explanations in the text). The error bars shown in graph (a) illustrate the statistical errors due to the finite number of the simulated trajectories. The spectra correspond to the opening angle  $\theta_0 = 0.24$  mrad. Figure from Ref. [43].

the enhancement factor over the emission spectra in amorphous medium, are shown in Fig. 16. For the sake of comparison the spectra formed by a positron moving in an "ideal undulator" (i.e., along the sine trajectory with the given values of  $a$  and  $\lambda_u$ ) are also shown in the upper figures.

#### 4.5. Interplay and specific features of radiation mechanisms for electrons in crystalline undulators

In recent papers [41, 43, 44] an accurate numerical analysis has been performed of the evolution of the channeling properties and the radiation spectra for diamond(110) based CUs. Drastic changes in the radiation spectra with variation of the bending amplitude  $a$  have been observed for different projectile energies and their sensitivity to the projectile's charge has been noted. Some of the predictions made can be verified in channeling experiments with electrons at the MAMI facility.

The calculations were performed for 270–855 MeV electrons and positrons propagating in the 20 microns thick diamond crystal. The periodic bending was assumed to have a harmonic shape  $S(z) = a \cos(2\pi z/\lambda_u)$  with the coordinate  $z$  measured along the incident beam direction. The bending period was fixed at  $\lambda_u = 5$  microns whereas the bending amplitude was varied from  $a = 0$  (straight crystal) up to  $a = 4.0$  Å in accordance with the parameters of crystalline samples used in the experiments at MAMI [99].

Figure 17 presents the emission spectra for the positrons and electrons with  $\varepsilon = 855$  MeV calculated for the opening angle  $\theta_0 = 0.24$  mrad, which is smaller than the natural emission angle  $\gamma^{-1} = 0.59$  mrad. For both types of projectiles the spectra formed in the straight crystal, graph (a), are dominated by the peaks of ChR, the spectral intensity of which by far exceeds that of the incoherent bremsstrahlung background

$2.5 \times 10^{-5}$  in the amorphous medium. For positrons, nearly perfect harmonic channeling oscillations give rise to the narrow peak at  $\hbar\omega_{\text{ChR}} \approx 3.6$  MeV. Strong anharmonicity of the electron channeling oscillations makes the ChR peaks (marked with the upward arrows) less pronounced and significantly broadened (note the scaling factor  $\times 5$  applied to the electron spectra).

In periodically bent crystals, Figs. 17(b)-(d), the spectra exhibit additional features some of which evolve differently with increase in  $a$ .

- For both types of projectiles there are CUR peaks in the low-energy part of spectra. The most powerful peaks correspond to the emission in the first harmonic at  $\hbar\omega_{\text{CUR}} \approx 1$  MeV. To be noted is the non-monotonous dependence of the peak values on bending amplitude  $a$ . This feature has been discussed in detail in Refs. [43,44].
- For positrons, the intensity of ChR becomes strongly suppressed as bending amplitude increases: for  $a = 1.2$  Å the intensity is two times less than in the straight crystal. For larger amplitudes, ChR virtually disappears [41,43]. This happens because the (mean) amplitude of channeling oscillations is a decreasing function of  $a$ . Indeed, as  $a$  increases, the centrifugal force, especially in the points of maximum curvature, drives the projectiles oscillating with large amplitudes away from the channel resulting in a strong quenching of the oscillations. A quantitative analysis of this feature one finds in Ref. [43].
- For electrons, the peak value of ChR does not fall off so dramatically. As  $a$  increases, the peak (marked with the upward arrow) becomes blue-shifted and there appears additional structure (the downward arrow) on the right shoulder of the spectrum. The analysis carried out in Ref. [44] has shown that both features are due to the emission by dechanneled electrons. In a periodically bent crystal, a dechannel particle can experience (i) the volume reflection (VR) [100,102], occurring mainly at the points of maximum curvature, and (ii) the over-barrier motion in the regions with small curvature. These types of motion contribute to different parts of the radiation spectrum. The radiation, which accompanies VR, is emitted in same energy domain as the ChR. The over-barrier particles radiate at higher energies and this radiation reveals itself as an additional peak in the spectrum. The radiation emission by over-barrier particles in the field of a periodically bent crystal was discussed qualitatively in Ref. [103] within the continuous potential framework. More detailed quantitative analysis of the phenomena involved can be provided by means of all-atom molecular dynamics. Below we present a brief overview of the results obtained and conclusions drawn in Ref. [44].

To compare the contributions to the total emission spectrum coming from channeling and non-channeling particles the following procedure has been adopted. Each simulated trajectory has been divided into segments corresponding to different types of motion. Namely, we distinguished the following parts of the trajectory: (i) the channeling motion segments, (ii) segments corresponding to the over-barrier motion

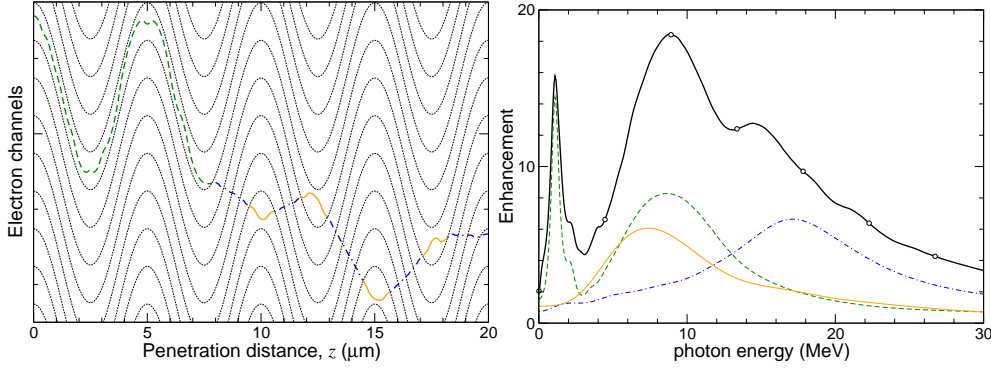


**Figure 18.** *Left.* An exemplary trajectory of a 855 MeV electron in a diamond (110) crystal bent periodically with  $a = 2.5 \text{ \AA}$  and  $\lambda_u = 5 \text{ \mu m}$ . Highlighted are the segments corresponding to (i) the channeling regime (dashed green curve), (ii) the over-barrier motion (dashed-dotted blue curves), (iii) to the VR events (solid orange curves). Thin wavy lines mark the boundaries of the electron channels.

*Right.* Solid black curve with open circles shows the enhancement factor of the total radiation emitted by 855 MeV electrons in the diamond (110) crystal bent as described above. Dashed green, dashed-dotted blue and solid orange curves show the contributions coming from the segments of the channeling and over-barrier motions and due to the VR, respectively. Ref. [44].

across the periodically bent crystallographic planes, (iii) segments corresponding to the motion in the vicinity of points of maximum curvature where a projectile experiences VR. For each type of the motion, the spectrum of emitted radiation has been computed as a sum of emission spectra from different segments. Thus, the interference of radiation emitted from different segments has been lost.

The aforementioned procedure is illustrated by Fig. 18. Its left panel presents a selected trajectory of a 855 MeV electron propagating in periodically bent crystal with bending amplitude  $2.5 \text{ \AA}$ . Different types of segments are highlighted in different colour and type of the line as indicated in the caption. The emission spectra corresponding to different types of motion (calculated accounting for all simulated trajectories) are shown in the right panel. The dependences presented allow one to associate the maxima in the total spectrum (black solid curve) with the corresponding type of motion. The radiation emitted from segments of channeling motion (dashed green curve) govern the spectrum in the vicinity of the CUR peak ( $\hbar\omega_{\text{CUR}} \approx 1 \text{ MeV}$ ) and contributes greatly to the ChR at  $\hbar\omega_{\text{ch}} \approx 6 \dots 12 \text{ MeV}$ . Numerical analysis of the simulated trajectories has shown that the curvature of the trajectories segments in the points of VR is close to that of the channeling trajectories. As a result, the radiation from the VR segments is emitted in the same energy interval as ChR so that the peak centered at  $\approx 9 \text{ MeV}$  is due both to the channeling motion and to the VR events. The over-barrier particles experience quasi-periodic modulation of the trajectory when crossing the periodically bent channels. The (average) period of these modulation is smaller than that of the channeling motion and decreases with the increase of the bending amplitude. For  $a = 2.5 \text{ \AA}$  this period is approximately two times less than the (average) period of channeling oscillations. As

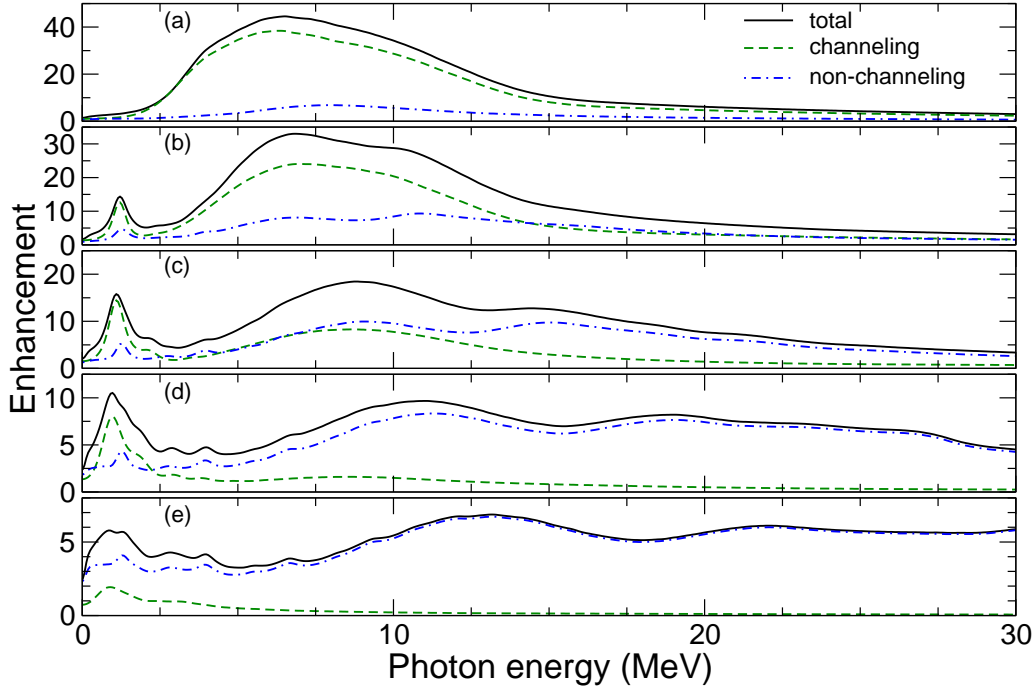


**Figure 19.** Enhancement factor of the radiation over the Bethe-Heitler spectrum for 855 MeV electrons in straight (a) and periodically bent (graphs (b)-(e) correspond to  $a = 1.2, 2.5, 4.0, 5.5$  Å) diamond(110) crystals. Solid black curves show the total spectra, dashed green ones correspond to the radiation emitted from the channeling segments only, and dashed-dotted blue curves present the spectra due to all non-channeling parts of the simulated trajectories. Ref. [44].

a result, radiation emitted from the over-barrier segments (dashed-dotted blue curve) is most intensive in the range  $\hbar\omega_{\text{ch}} \approx 15 \dots 20$  MeV. This contribution results in the additional structure in the total spectrum.

Figure 19 illustrates the evolution of the contributions from the channeling and non-channeling particles to the emission spectrum with bending amplitude. In the figure, each graph presents the total spectrum (solid curve) as well as the contributions of the channeling segments (dashed curve) and the non-channeling segments (both over-barrier and VR, dash-dotted curve).

In the straight crystal as well as in the periodically bent one with small bending amplitude ( $a = 1.2$  Å) the emission spectrum above 1 MeV is dominated by the channeling particles which provide main contributions to the ChR peak. As  $a$  increases, the role of the non-channeling segments becomes more pronounced whereas the channeling particles contribute less. The increase in  $a$  leads to (i) increase of the curvature of a particle's trajectory in the vicinity of the VR points, (ii) decrease in the period of the quasi-periodic modulation of the trajectories of over-barrier particles. As a result, two maxima seen in the graphs (b)-(e) become blue shifted as  $a$  increases: the maxima marked with upward arrows are due to the channeling motion and to the VR, those marked with downward arrows are associated with the over-barrier particles. For



large bending amplitudes, graphs (d)-(e), these maxima are virtually due to the emission of the non-channeling particles only.

The low-energy part of the spectrum formed in periodically bent crystals is dominated by the peak located at  $\hbar\omega \approx 1$  MeV. For moderate amplitudes,  $a \leq 2.5$  Å, when the bending parameter (5) is small, this peak associated with CUR and is due to the motion of the accepted particles which cover a distance of at least one period  $\lambda_u$  in a periodically bent channel. For larger amplitude,  $a = 4.0$  Å ( $C = 0.77$ ), the penetration length  $L_p$  of the accepted particles become less than half a period leading to noticeable broadening of the CUR peak. For even larger amplitudes, there are further modifications of the peak related to the phenomenon different from the channeling. Graph (e) shows the dependences for  $a = 5.5$  Å which corresponds to the bending parameter larger than one,  $C = 1.15$ . As a result, only a small fraction of the incident electrons is accepted, and channels over the distance less than  $\lambda_u/2$  having very small amplitude of channeling oscillations,  $a_{ch} \ll d/2$ . Therefore, these particles virtually do not emit ChR but nevertheless contribute to the CUR part of the spectrum (see the dashed curve in the graph). However, this contribution is not a dominant one. The main part of the peak intensity in the total spectrum comes from the non-channeling particles, see the dash-dotted curve. The explanation is as follows [44]. As discussed above, a trajectory of a non-channeling particle consists of short segments corresponding to VR separated by segments  $\Delta z \approx \lambda_u/2$  where it moves in the over-barrier mode. In the course of two sequential VR the particle experiences 'kicks' in the opposite directions, see the lower trajectory in Fig. 18(a)). Therefore, the whole trajectory becomes modulated periodically with the period  $2\Delta z \approx \lambda_u$ . This modulation gives rise to the emission in the same frequency as CUR.

These effects, which are due to the interplay of different radiation mechanisms in periodically bent crystals, can be probed experimentally. In this connection one can mention recent successful experiments on detecting the excess of radiation emission due to VR in oriented bent Si(111) crystal by 855 MeV electrons [57] and 12.6 GeV electrons [101].

#### 4.6. Channeling and radiation emission in SASP periodically bent crystals

The original concept of a CU assumes the projectiles channel in the crystal following the periodically bent planes or axes. For such motion, the undulator modulation frequencies  $\Omega_u$  are smaller than the frequencies  $\Omega_{ch}$  of the channeling oscillations. This regime implies periodic bending with large-amplitude,  $a > d$ , and large-period,  $\lambda_u \gg a$ . As a result, the CUR spectral lines appear at the energies below those of ChR [104–106].

Another regime of periodic bending, termed as Small-Amplitude Short-Period (SASP), was suggested recently [107]. This regime implies bending with  $a \ll d$  and  $\lambda_u$  shorter than the period of channeling oscillations. In contrast to the motion in a CU, the channeling trajectory in a SASP crystal does not follow the short-period bent planes but acquires a short-period jitter-type modulations resulting from the bending. These



modulations lead to the radiation emission at the energies exceeding the energies of the channeling peaks [35, 40, 107–111]. Interestingly, a similar radiative mechanism has recently been studied with respect to the radiation produced by relativistic particles in interstellar environments with turbulent small-scale fluctuations of the magnetic field [112, 113].

In Ref. [40] results of a thorough study of channeling and radiation by 855 electrons and positrons passing through a SASP silicon crystal has been presented. Comprehensive analysis of the channeling and radiation processes has been carried out on the grounds of numerical simulations. Specific features which appear due to the SASP bending has been highlighted and elucidated within an analytically developed continuous potential approximation (see Appendix B). The parameters of the SASP bending were chosen to match those used in the experiment with 600 and 855 electrons carried out at MAMI [108]. A SASP crystal used in the experiment was produced by using  $\text{Si}_{1-x}\text{Ge}_x$  graded composition with the Ge content  $x$  varied from 0.3 % to 1.3 % to achieve a periodic bending of (110) planes with the amplitude  $a = 0.12 \pm 0.03 \text{ \AA}$  and period  $\lambda_u = 0.43 \pm 0.004 \text{ }\mu\text{m}$ . The number of periods quoted was 10. No further details on the actual characterization of the profile of periodic bending were provided although in a more recent paper [111] it was noted that "... the shape is roughly sinusoidal".

In the simulations [40] a thicker crystalline sample,  $L = 12 \text{ }\mu\text{m}$ , was probed assuming perfect cosine bending with period 400 nm and amplitude varied from  $a = 0$  (straight channel) up to  $a = 0.9 \text{ \AA}$ , which is close to the half of the (110) interplanar spacing in silicon crystal ( $d = 1.92 \text{ \AA}$ ). The calculated emission spectra cover a wide range of the photon energies, from  $\lesssim 1 \text{ MeV}$  up to 40 MeV. The integration over the emission angle  $\theta$  was carried out for two particular cones determined by the values  $\theta_0 = 0.21$  and 4 mrad. For a 855 MeV projectile the natural emission angle is  $\gamma^{-1} \approx 0.6$  mrad. Therefore, the smallest value of  $\theta_0$  refers to a nearly forward emission, whereas the largest value, being significantly larger than  $\gamma^{-1}$ , provides the emission cone which collects almost all the radiation emitted.

The spectra computed display a variety of features seen in Fig. 20. To be noticed are the pronounced peaks of ChR in the spectra for the straight crystal (the black solid-line curves). Nearly perfectly harmonic channeling oscillations in the positron trajectories (the examples of the simulated trajectories can be found in [12, 15, 32]) lead to the undulator-type spectra of radiation with small values of the undulator parameter,  $K^2 \ll 1$ . The positron spectra in straight Si(110) clearly display the fundamental peaks of ChR at the energy  $\hbar\omega \approx 2.5 \text{ MeV}$ , whereas the higher harmonics are strongly suppressed. In particular, for the smaller emission cone the peak intensity in the fundamental harmonic is an order of magnitude larger than that for the second harmonics at  $\hbar\omega \approx 5 \text{ MeV}$ , and only a tiny hump of the third harmonics can be recognized at about 7.5 MeV (see the top left plot in the figure). For electrons passing through the straight crystal, the ChR peaks are less intensive and much broader than these for the positrons, as a result of stronger anharmonicity of the channeling oscillations in the trajectories.

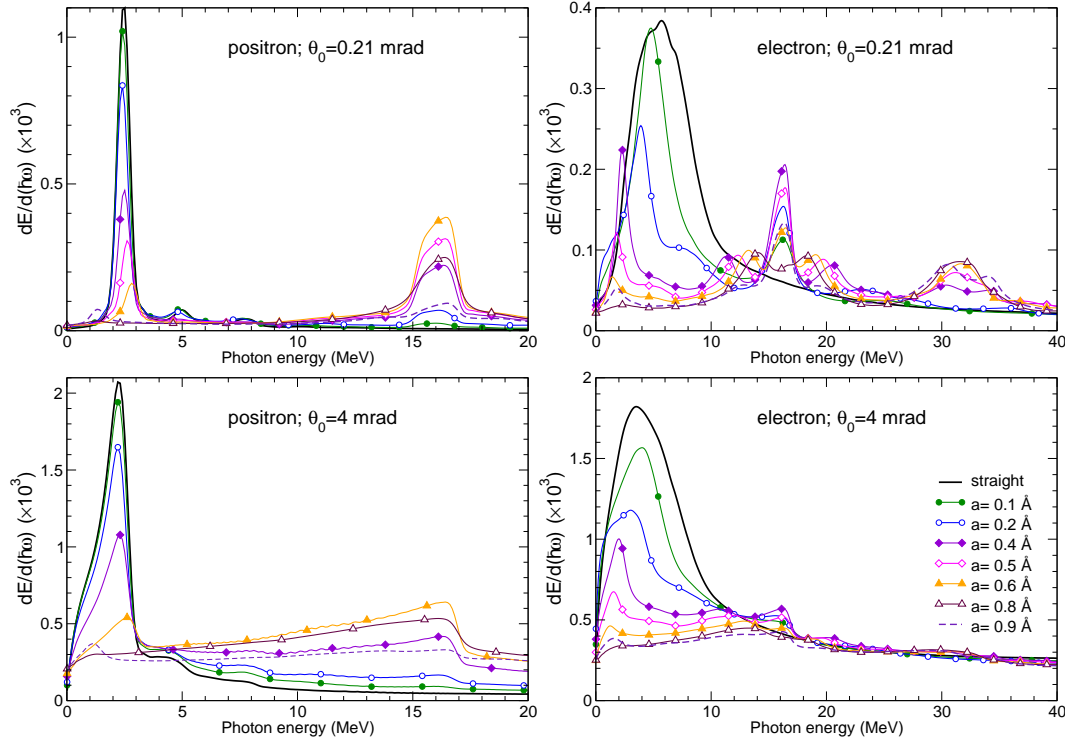


**Figure 20.** Spectral distribution of radiation emitted by 855 MeV positrons (left) and electrons (right) in straight (thick solid lines) and SASP bent Si(110) with period  $\lambda_u = 400$  nm and various amplitudes  $a$  as indicated in the common legend located in the right bottom graph. The upper and lower plots correspond to the aperture values  $\theta_0 = 0.21$  and 4 mrad. All spectra refer to the crystal thickness  $L = 12 \mu\text{m}$ . The intensity of the bremsstrahlung radiation in amorphous silicon (calculated within the Bethe-Heitler approximation) is  $0.016 \times 10^{-3}$  and  $0.15 \times 10^{-3}$  for  $\theta_0 = 0.21$  and 4 mrad, respectively.

The radiation spectra produced in the SASP bent crystals display additional peaks, which emerge from the short-period modulations of the projectile trajectories (see the discussion in Section Appendix B.2). These peaks, more pronounced for the smaller emission cone, appear at the energies larger than the energies of the channeling peaks. For both types of the projectiles, the fundamental spectral peaks in the radiation emergent from the SASP bending correspond to the emission energy about 16 MeV significantly above the ChR peaks. For positrons, the peaks of radiation due to the bending are displayed in the spectra for the amplitude values  $0.1 \dots 0.9 \text{ \AA}$ . For smaller values of  $a$ , the spectral peaks disappear because the positrons experience mainly "regular" channeling staying away from the crystalline atoms and being therefore less affected by the SASP bent planes (see Ref. [40] and Section Appendix B.2 below for the details). In contrast, the electrons experience the impact of the SASP bending at lower values of  $a$ . As seen in the right upper plot for the fundamental spectral peaks emergent from the bending, the peak for  $a = 0.1 \text{ \AA}$  is only two times lower than the maximal peak displayed for  $a = 0.4 \text{ \AA}$ .

To be noted are the spectral properties for smaller aperture value (upper plots in

Fig. 20). The electron spectra display peaks at the energies around 32 MeV for the values of  $a$  exceeding 0.2 Å. These peaks are clearly the second harmonics of the radiation emergent from the SASP bending. In addition, the peaks of channeling radiation decrease in heights and shift towards the lower emission energies. The positron spectra, in contrast to the electron ones, exhibit less peculiarities and gradually converge to the Bethe-Heitler background with increasing radiation energies. For the larger aperture value,  $\theta_0 = 4$  mrad, a sizable part of the energy is radiated at the angles  $\theta > \gamma^{-1}$ . The harmonics energies decrease with  $\theta$  approximately as  $(1 + K^2/2 + (\gamma\theta)^2)^{-1}$ . As a result, the peaks of ChR and those of the radiation due to the SASP bending broaden and shift towards softer radiation energies.

Recently, the impact of the radiation collimation on the intensity of the SASP peaks has been measured in experiments with a 855 MeV electron beam at MAMI [110]. The crystal was produced by adding a fraction  $x$  of germanium atoms to a silicon substrate. By alternating successively a linear increase of  $x$  from 0.5 % to 1.5 % with a linear decrease a sawtooth pattern of the SASP bending was achieved with 120 periods each of a  $\lambda_u = 0.44$   $\mu\text{m}$  wavelength. It was indicated in the paper that "the expected oscillation amplitude" of the (110) planes is  $a \approx 0.12$  Å. In the experiment the radiation spectra enhancement over the amorphous silicon was measured. The measurements were performed (i) with collimation to an emission angle  $\theta_0 \approx 0.24$  mrad, and (ii) with no collimation. It was noted that the latter case corresponded to the emission cone  $\theta_0 = 4$  mrad  $\gg \gamma^{-1}$  considered in [40].

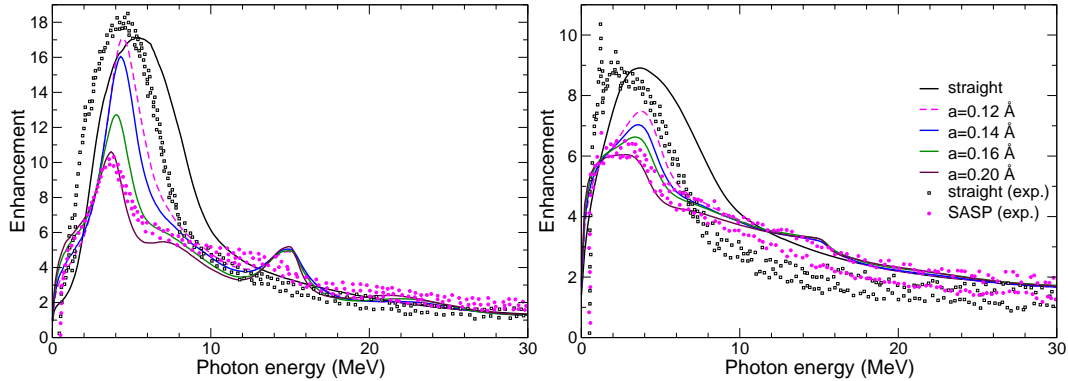


**Figure 21.** Enhancement of radiation emitted by 855 MeV electrons in straight and SASP bent Si(110) with respect to the amorphous silicon. The data refer to the crystal thickness  $L = 52.3$   $\mu\text{m}$  and bending period  $\lambda_u = 436$  nm (total number of periods equals to 120). Left and right graphs refer to the emission cones with opening angle  $\theta_0 = 0.24$  and 4 mrad, correspondingly. Symbols stand for the experimental data taken from Ref. [110] where the bending amplitude was assumed to be  $a = 0.12$  Å. Common legend is presented in the right graph.

In Fig. 21 we compare the experimental data (symbols) with the results of simulations carried out with MBN EXPLORER (solid lines). Shown are the dependences of the enhancement factor on the photon energy for straight and SASP bent Si(110). Left graph corresponds to the narrow emission cone,  $\theta_0 = 0.24$  mrad, the right graph

presents the data for the wide cone,  $\theta_0 = 4$  mrad. The simulations were performed for several values of the bending amplitude as indicated in the common legend shown in the right graph.

The same SASP bent Si(110) with 120 undulations with period  $\lambda_u = 0.44 \mu\text{m}$  was used in the experiment at the SLAC facility with a 16 GeV electron beam [111]. In the experiment, the SASP signal can only be expected to appear when the crystal is properly aligned and should reveal itself in a narrow emission angle and the presence of a peak in the spectrum. Therefore, in Ref. [111] the enhancement was looked for as the crystal was rotated in the beam, passing through the aligned condition, and a narrow radiation cone when scanning the horizontal angular distribution with the SciFi detector, both measurements feasible at high beam intensity. However, it was mentioned in the cited paper that the measurements of the spectrum were not successful due to difficulties with the experimental setup and variations in beam energy that had not been expected.

In connection with these experiments, which initially had been planned to be carried out with both electron and positron beams, the channeling simulations were carried out for 15-35 GeV projectiles [114] by means of the MBN EXPLORER package. The simulations of trajectories were supplemented with computation of the spectra of the emitted radiation for various detector apertures. It was recommended to carry out experiments with electrons and with the smallest aperture possible. In this case the SASP signal in the spectrum was expected to be the highest. Figure 22 illustrates theoretical predictions by presenting the spectral distribution of radiation energy emitted by 20 GeV projectiles in the narrow  $13 \mu\text{rad} \approx 1/2\gamma$  (left graph) and wide  $13 \mu\text{rad} \approx 5/\gamma$  (right graph) cones along the incoming beam direction. The peaks centered around  $\hbar\omega = 7$  GeV are due to the SASP bending. The peaks at much lower energy (0.2-0.5 GeV) correspond to ChR.

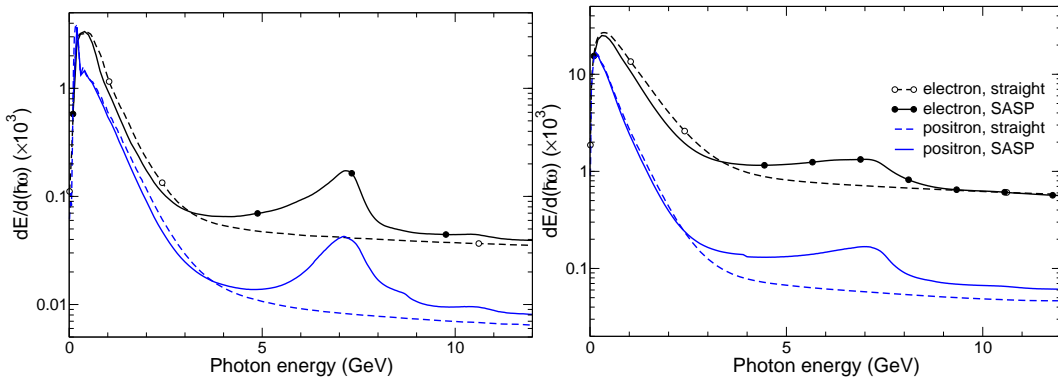


**Figure 22.** Spectral distribution of radiation emitted by 20 GeV electrons and positrons in straight and SASP bent Si(110). The data refer to the crystal thickness  $L = 52.3 \mu\text{m}$ , bending period  $\lambda_u = 436 \text{ nm}$  and bending amplitude  $a = 0.12 \text{ \AA}$ . Left and right graphs refer to the emission cones with opening angle  $\theta_0 = 13$  and  $130 \mu\text{rad}$ , correspondingly. Common legend is presented in the right graph.

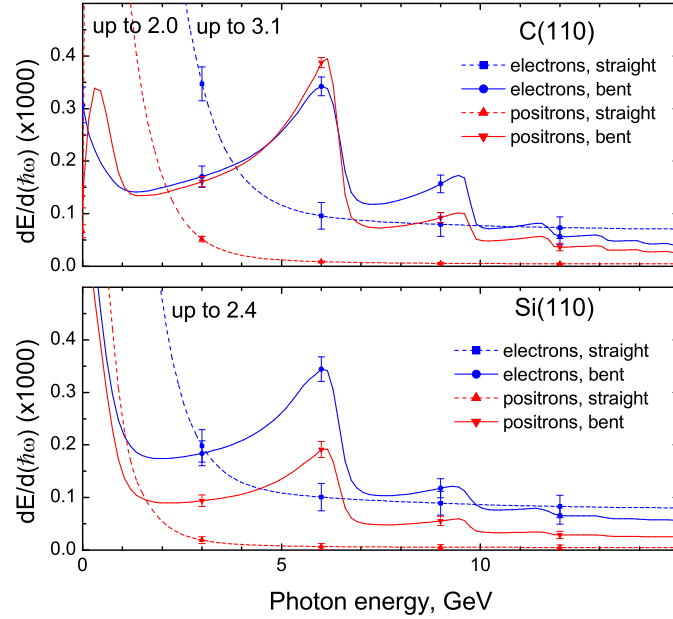


**Figure 23.** Spectral distribution of radiation emitted by 20 GeV electrons and positrons in straight and SASP periodically bent 4 microns thick diamond(110) (top) and silicon(110) (bottom) oriented crystals. Bending amplitude and period are 0.4 Å and 0.4  $\mu\text{m}$ , respectively. Refs. [37, 38].

#### 4.7. Stack of SASP periodically bent crystals

In recent series of experiments at MAMI [108] with 600 and 855 MeV electrons the effect of the radiation enhancement due to the SASP periodic bending has been observed (see discussion in Section 4.6). Another set of experiments with thin SASP diamond crystals was planned within the E-212 collaboration at the SLAC facility (USA) with 10-20 GeV electron beams [109].

As a case study aimed at producing theoretical benchmarks for the SLAC experiments, a series of numerical simulations have been performed of the planar channeling of 10-20 GeV electrons and positrons in straight and SASP periodically bent thin crystals of silicon and diamond [37, 38]. The crystal thickness  $L$  was set to 4 microns, the period of bending  $\lambda_u = 0.4$  microns and the bending amplitude  $a = 0.4$  Å, which is lower than half of the (110) interplanar distance in both cases.

In Figure 23 the results of the simulation of radiation of 20 GeV projectiles are compared for the cases of straight and periodically bent diamond(110) crystals. The beam emittance was taken equal to  $\psi = 5$   $\mu\text{rad}$ . The spectra presented refer to the emission cone  $\theta_0 = 150$   $\mu\text{rad}$ , which is 5.8 times higher than natural emission angle  $1/\gamma = 25.6$   $\mu\text{rad}$  and thus collects virtually all radiation emitted. In both figures the peaks located below 1 GeV corresponds to the channeling radiation. For periodically bent targets, the peaks at  $\hbar\omega \approx 6$  GeV and above are due to the SASP bending. Note, that bending of a crystal leads to significant suppression of the channeling peak. This effect can be explained qualitatively in terms of the continuous potential modification

in a SASP channel (see Section Appendix B.1). With increase of bending amplitude the depth of the potential well decreases and the width of the potential well grows resulting in decrease of the number of channeling projectiles and in lowering frequencies of channeling oscillations.

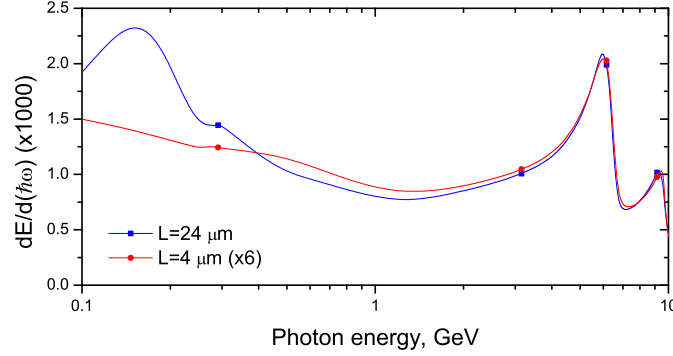


**Figure 24.** Emission spectra for 20 GeV electrons in SASP bent diamond(110) crystal calculated for two different thicknesses, as indicated. The value  $L = 24 \mu\text{m}$  exceeds characteristic channeling oscillations period while  $L = 4 \mu\text{m}$  is lower than that. Note the absence of channeling radiation peak around 150 MeV in the latter case. For the sake of comparison, the curve for  $L = 4 \mu\text{m}$  is multiplied by six. Refs. [37,38].

Another factor that leads to the suppression of the channeling radiation is that for the 20 GeV projectiles the characteristic period of channeling oscillations, deduced from the simulated trajectories, is about  $\langle \lambda_{\text{ch}} \rangle \approx 10$  microns for both diamond and silicon crystals, so that the crystal is too thin to allow for even a single channeling oscillation. Therefore, the peak of channeling radiation is not that pronounced as in the case of thicker,  $L > \lambda_{\text{ch}}$ . The emission spectra formed in thick ( $L = 24$  microns) and thin ( $L = 4$  microns) crystals are compared in Fig. 24 where the latter spectrum is multiplied by a factor of 6 for the sake of convenience. A sharp peak of the channeling radiation at  $\hbar\omega \approx 150$  MeV is present for the thick crystal whereas for the thin one it reduces to a small hump, which is due to the synchrotron-type radiation emitted by projectiles moving along the one-ark trajectory. Remarkable feature, seen in the figure, is that the peaks due to the SASP bending in both curves virtually coincide.

The effects of suppression of the channeling radiation but maintaining the level of undulator radiation in thin crystals can be used to produce intensive radiation at much higher energies corresponding to the SASP bending. To increase the latter intensity one can increase the crystal thickness  $L$ . However, this extensive approach is not optimal taking into account complications related to the technological aspects (increase in the time of the crystal growth as well as in the costs associated, accumulation of the defects in the crystalline structure etc.) Alternatively, instead of a single thick crystal, a stack of several aligned thin crystals can be used [37,38], as illustrated by Fig. 25. A projectile passes sequentially several layers of periodically bent crystals, which constitute the stack, and the radiation produced in each element of the stack adds to the total radiation emitted by the projectile. For SASP undulator the thickness of layers can be



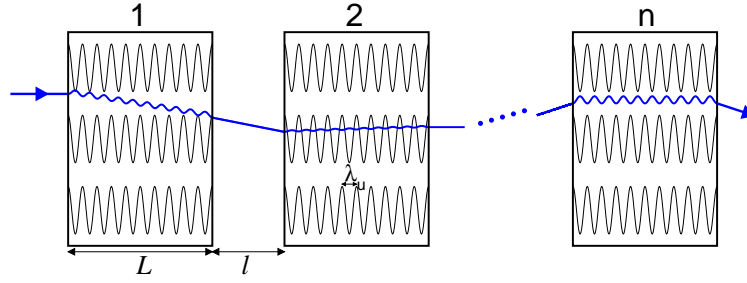


**Figure 25.** Stack of  $n$  SASP bent crystal layers each of the thickness  $L$  separated by the gaps  $l$ . Periodic bending of the crystalline structure is illustrated by thin cosine curves. Blue line illustrates a projectile's trajectory which consists of the modulated parts (inside the crystals) and of the straight line segments in between the layers.

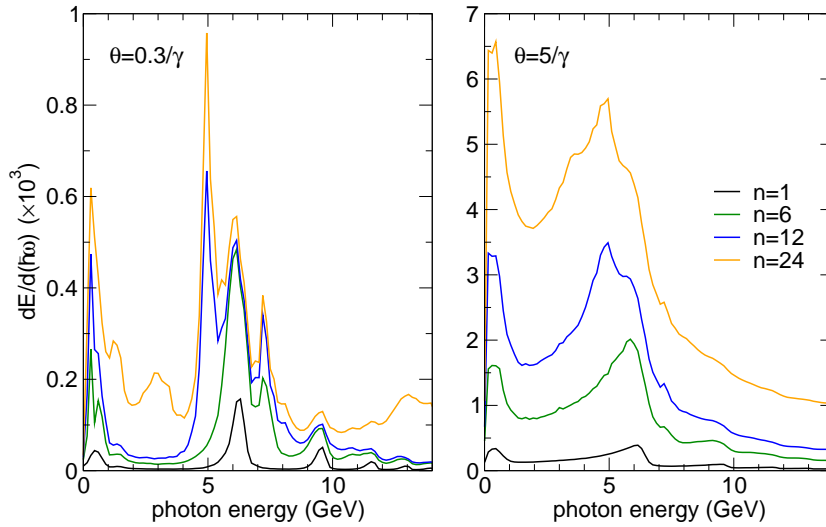


**Figure 26.** Radiation spectra for the small  $\theta_0 = 0.3/\gamma$  (left panel) and large  $\theta_0 = 5/\gamma$  (right) apertures calculated for different number  $n$  of diamond(110) periodically bent crystals in stack (as indicated in the common legend). The data refer to 20 GeV positrons, the bending amplitude and period are  $0.4 \text{ \AA}$  and 400 nm, respectively.

taken in the interval between the bending period  $\lambda_u$  and the characteristic channeling period of projectile. Such choice of the parameters leads to absence of full channeling oscillation periods in each channeling segment of trajectory of projectile which results in suppression of channeling radiation. The effect of undulator radiation in the system remains and grows with increase of number of layers. Thickness of each crystal layer can be chosen to be smaller than the period of channeling oscillations of the projectile thus suppressing ChR. The intensity of radiation due to the SASP periodic bending increases with the number the stack layers.

To simulate the radiation emission from the stack the following system was modeled [37, 38]. A set of several  $L = 4$  microns thick layers of SASP periodically bent crystals (bending period  $\lambda_u = 0.4$  microns) separated with  $l = 4$  microns gaps were generated in the simulation box. The 20 GeV projectiles (positrons) entered the first layer tangent to the (110) crystallographic plane. Due to the multiple scattering in the layer, a



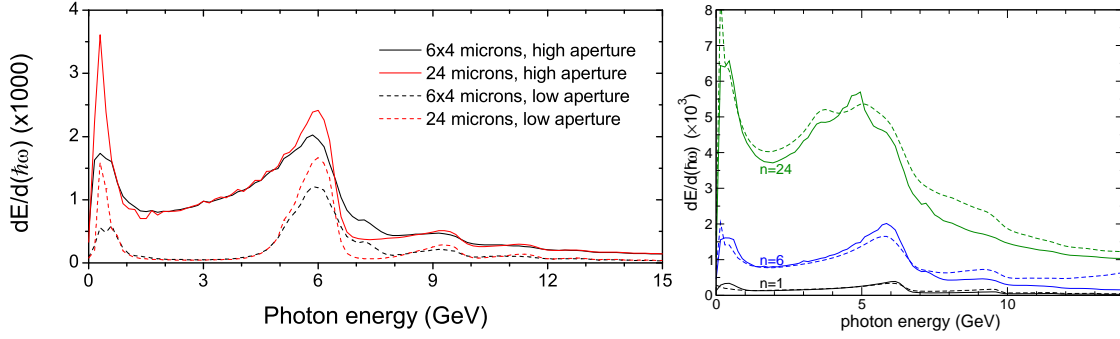


**Figure 27.** *Left panel.* Comparison of radiation spectra formed by 20 GeV positrons in a  $L = 24$  microns thick crystal and in a stack of six  $L = 4$  microns thick layers. Dashed curves present the spectra calculated for the smaller emission angle,  $\theta_0 = 15.3 \mu\text{rad}$ , solid curves – for the larger emission angle  $\theta_0 = 256 \mu\text{rad}$ . Refs. [37,38].

*Right panel.* Comparison of radiation spectra from 20 GeV positrons (solid curves) and electrons (dashed curves) emitted in stacks of diamond(110) SASP periodically bent crystals with different number of layers as indicated. The data refer to the emission angle  $\theta_0 = 5/\gamma = 256 \mu\text{rad}$ .

projectile leaves is at some non-zero angle are with respect to the initial direction and this angle serves as the incident angle at the entrance to the second layer, etc. The multiple scattering leads to a gradual increase of the angular dispersion of the transverse velocity of projectiles and to the decrease of the number of channeling particles with the growth of the layer's number. As a result, for moderate number of layers the destructive effect of the multiple scattering is not too pronounced, so that the radiation intensity increases being proportional to  $n$ . For sufficiently large  $n$  values, the intensity reaches its saturation level and the peak intensity becomes independent on  $n$ .

Figure 26 compares the radiation spectra calculated for different number of layers in stack, as indicated. For the smaller emission angle ( $\theta_0 = 0.3/\gamma = 15.3 \mu\text{rad}$ , left panel) the radiation intensity scales linearly with the number of stack layers until  $n = 6$ . For larger values of  $n$  the spread of the projectiles' transverse velocities gets wider so that the intensity of radiation emitted within a narrow cone along the initial beam direction saturates. For the larger emission angle ( $\theta_0 = 5/\gamma = 256 \mu\text{rad}$ ) the nearly linear growth of the intensity continues up to  $n = 24$ .

Left panel in Fig. 27 compares the intensities of radiation emitted by 20 GeV positrons traveling in a single 24 microns thick SASP diamond(110) crystal and in a stack of six thin ( $L = 4$  microns) layers. It is seen, that for the channeling peak in the spectrum is suppressed in the case of the stack of layers, whereas the undulator peaks are of the same intensity for both targets. Right panel in the figure compares the emission spectra for positrons and electrons of the same energy, 20 GeV, and in the same target (stacks of  $n = 1, 2$  and 24 layers. The curves presented illustrate weak sensitivity of the spectra formed in SASP periodically bent crystals to the sign of a projectile's charge.

Therefore, this regime is favorable for the construction of light sources with the use of intensive electron beams which, at present, are more available than positron beams.

## 5. Conclusion

In this paper we have discussed the relativistic molecular dynamic approach implemented in the multi-purpose MBN EXPLORER software package for accurate computational modeling of propagation and radiation emission by various ultra-relativistic projectiles in crystalline media. The exemplary case studies presented refer to various straight, bent and periodically bent oriented crystals. In cases where the experimental data are available (in particular, the data on the dechanneling length and on the emission spectra) it has been used for the comparison with the results of numerical simulations.

The software package used in the current paper allows for advanced computation exploration, which can be carried out at the atomistic level of detail, of a variety of phenomena accompanying propagation of high energy particles in crystals. Apart from the trajectories simulation and the calculation of the relevant quantities, one can model and analyze quantitatively more complex processes. The latter include:

- (i) structural changes in crystals due to the irradiation and their impact on the projectiles propagation and on the emission spectra (this is important to account for when the target is exposed to highly intensive beams as, for example, the FACET beam at SLAC [80, 115]);
- (ii) the crystal structure modifications, incl. the defects formation, occurring in the course of fabrication of bent and periodically bent crystals (see Ref. [1] for the review of the technologies developed);
- (iii) simulation of the projectile' dynamics with account for the radiation damping force (this is important when considering propagation of highly energetic electrons and positrons,  $\varepsilon \gtrsim 10^2$  for low- $Z$  crystals and  $\varepsilon \gtrsim 10$  for high- $Z$  crystals, when radiative energy losses become noticeable [116]);
- (iv) account for quantum effects (e.g., ionizing collisions, bond breaking [119], specific quantum features in the incoherent scattering from the constituent atoms [120]). which accompany a projectile propagation.

Apart from these, the MBN EXPLORER architecture allows one to develop and explore multiscale algorithms for simulations of the long-term dynamics of a crystalline medium on time scales significantly exceeding those achievable by means of conventional molecular dynamics [48].

These important features of MBN EXPLORER increase significantly accuracy of its predications, expand its application areas and go well beyond the limits of molecular dynamics codes which are unable to deal with the multiscale modeling as well as of the codes based on the continuous potential model for the crystalline field.

The atomistic approaches and the computational algorithms implemented in MBN

|| The radiative damping force can be introduced via different schemes (see, for example, recent paper [117]). The scheme that has been recently implemented in MBN EXPLORER is based on the formalism due to Landau and Lifshitz [118]. Previously, it had been implemented in Ref. [28] within the continuous potential framework.

EXPLORER open a broad range of possibilities for the virtual design of the novel crystal-based LSs, which are mentioned in the Introduction section and discuss in greater detail in Ref. [1]. Thus, the multiscale all-atom relativistic molecular dynamics simulations of the particle propagation and radiation in realistic crystals can be carried out. Combined with modern numerical algorithms, advanced computational facilities and computing technologies, it will bring the predictive power of the software up to the accuracy level comparable or maybe even higher than achievable experimentally. Ultimately, it will turn computational modeling into the instrumental tool that could substitute (or become an alternative to) expensive laboratory experiments, and thus reduce the experimental and technological costs. The important outcome of this analysis will enable us to provide the realistic characterization of the novel LSs in the photon energy range up to GeV region and allow for their optimization with respect to a particular experimental setup and targeted application.

## Acknowledgments

The work was supported in part by the DFG Grant (Project No. 413220201).

## Appendix A. Atomic and interplanar potentials

In this section, for the sake of reference, we compare atomic and interplanar potentials build using the parameterization due to Molière [46], Doyle and Turner [30], and Pacios [47].

The atomic system of units,  $e = m_e = \hbar = 1$ , is used in this Section.

### Appendix A.1. Atomic potential parameterization

Below we summarize the parameterizations for atomic potential,  $U_{\text{at}}(r)$ , and its Fourier image,  $\tilde{U}_{\text{at}}(q)$ :

$$U_{\text{at}}(r) = \frac{4\pi}{(2\pi)^3} \int_0^\infty \frac{\sin(qr)}{qr} \tilde{U}_{\text{at}}(q) q^2 dq. \quad (\text{A.1})$$

- The parameterization due to Molière [46] is based on the Thomas-Fermi atomic model:

$$\begin{cases} U_{\text{at,M}}(r) = \frac{Ze}{r} \sum_{j=1}^3 a_j \exp\left(-\frac{b_j r}{a_{\text{TF}}}\right) \\ \tilde{U}_{\text{at,M}}(r) = 4\pi Ze \sum_{i=1}^3 \frac{\alpha_j}{q^2 + \gamma_j^2} \end{cases}. \quad (\text{A.2})$$

Here  $Z$  is the nucleus charge,  $a_{\text{TF}} = 0.8853Z^{-1/3}$  is the Thomas-Fermi radius. The dimensionless Molière's coefficients are:  $a_{1,2,3} = (0.1, 0.55, 0.35)$ ,  $b_{1,2,3} = (6.0, 1.2, 0.3)$ . The short-hand notation  $\gamma_j = \beta_j/a_{\text{TF}}$  is used.

- Doyle and Turner [30] introduced parametric fits to kinematic scattering factors for X-rays and electrons with the use of relativistic Hartree-Fock approximation (see also Ref. [121]). From their formulae one derives the following parameterization:

$$\begin{cases} U_{\text{at,DT}}(r) = \frac{(4\pi)^3}{4\sqrt{\pi}} \sum_{j=1}^4 \frac{a_j}{b_j^{3/2}} \exp\left(-\frac{4\pi^2 r^2}{b_j}\right) \\ \tilde{U}_{\text{DT}}(q) = 2\pi \sum_{j=1}^4 a_j \exp\left(-\frac{b_j q^2}{(4\pi)^2}\right) \end{cases}. \quad (\text{A.3})$$

For carbon, silicon and germanium atoms the Doyle-Turner parameters  $a_j$  (in Å) and  $b_j$  (in Å<sup>2</sup>) are listed in Table A1.

**Table A1.** Parameters  $a_j$  (in Å) and  $b_j$  (in Å<sup>2</sup>) for the Doyle-Turner fit for several neutral atoms as indicated.

Atom	$a_1$	$b_1$	$a_2$	$b_2$	$a_3$	$b_3$	$a_4$	$b_4$
B	0.9446	46.4438	1.3120	14.1778	0.4188	3.2228	0.1159	0.3767
C	0.7307	36.9951	1.1951	11.2966	0.4563	2.8139	0.1247	0.3456
Si	2.1293	57.7748	2.5333	16.4756	0.8349	2.8796	0.3216	0.3860
Ge	2.4467	55.8930	2.7015	14.3930	1.6157	2.4461	0.6009	0.3415

It has been pointed out (see, e.g., Ref. [122]) that the D-T scheme does not provide correct behaviour of the potential at small distances since  $\lim_{r \rightarrow 0} U_{\text{a,DT}}(r) \neq \infty$ .

- For atoms from H to Kr, Pacios [47] proposed the following parameterization based on the Hartree-Fock potentials:

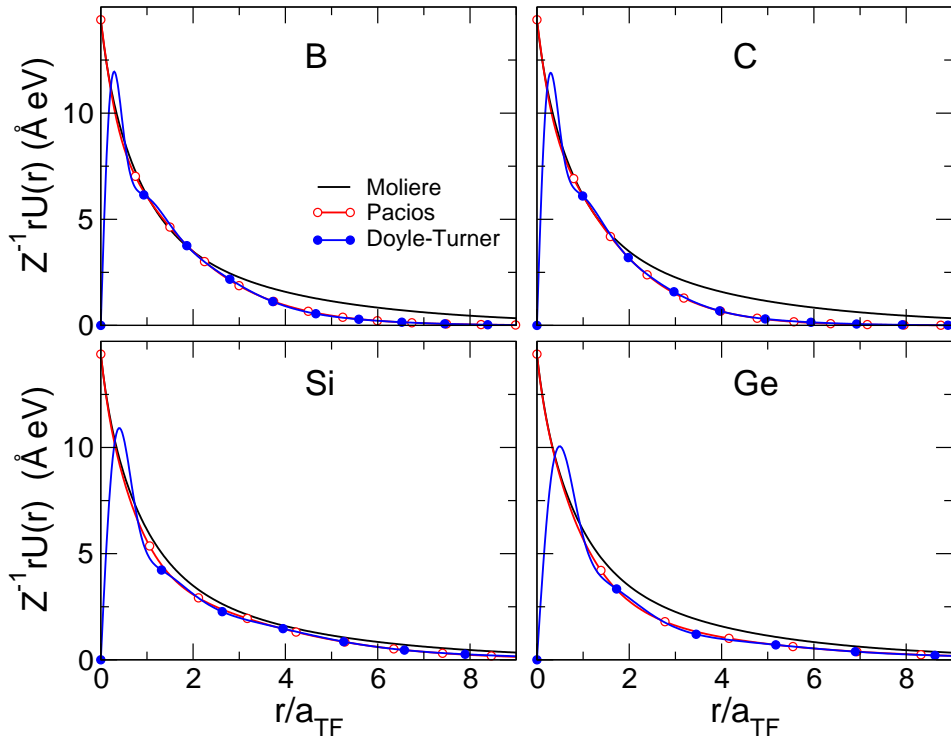
$$\begin{cases} U_{\text{at,P}}(r) = \frac{4\pi}{r} \sum_{j=1}^M \frac{a_j}{b_j^3} (2 + b_j r) \exp(-b_j r), \\ \tilde{U}_{\text{at,P}}(q) = 2(4\pi)^2 \sum_{j=1}^M \frac{a_j}{b_j^3} \left( \frac{1}{q^2 + b_j^2} + \frac{b_j^2}{(q^2 + b_j^2)^2} \right) \end{cases} \quad (\text{A.4})$$

Sets of the coefficients  $a_j$  and  $b_j$  ( $j = 1, \dots, M$ ) and values of the integer  $M$  for several selected atoms are presented in table A2. Note that the nucleus charge  $Z$  is absent in Eqs. (A.4). Although it is not indicated either in Ref. [47] or in earlier papers by the author, the nucleus charge and the coefficients are related as  $Z = 8\pi \sum_{j=1}^M a_j / b_j^3$ .

Figure A1 compares the dependences  $rU_{\text{a}}(r)/Z$  on  $r/a_{\text{TF}}$  calculated for several atoms by means of different parameterizations. the Molière, Pacios and Doyle-Turner approximations. We note that at large distances the Pacios and Doyle-Turner curves practically coincide whereas the Molière approximation provides larger values for the potential. At small distances, where the Doyle-Turner parameterization fails, both Molière and Pacios schemes lead to the same result.

**Table A2.** Parameters  $a_j$  and  $b_j$  (in a.u.) of the Pacios potential Eq. (A.4) for several atoms as indicated.

M		$a_1$	$a_2$	$a_3$	$a_4$	$b_1$	$b_2$	$b_3$	$b_4$
B	3	72.22775	-1.021225	0.778090	—	9.828608	2.984085	1.689647	—
C	4	128.0489	-2.535155	2.041774	—	11.84981	3.508196	2.099930	—
Si	4	1713.363	158.9419	-107.9461	1.348130	29.95277	4.305803	3.906608	1.627379
Ge	4	20901.16	1399.193	169.1339	0.991756	68.65812	22.95161	5.903443	1.541315

**Figure A1.** Dependences  $rU(r)/Z$  on  $r/a_{\text{TF}}$  calculated for B, C, Si and Ge atoms within the Molière, Pacios and Doyle-Turner approximations.

These differences in the behaviour of the atomic potentials reveal themselves in the scattering process of an ultra-relativistic projectile from an atom. Within the framework of classical small-angle scattering framework, the scattering angle  $\theta$  is related to the change of the transverse momentum  $\theta \approx c|\Delta\mathbf{p}_\perp|/\varepsilon$ . To calculate  $\Delta\mathbf{p}_\perp$  one assumes, that the projectile moves along a straight line (the  $z$  direction) with a constant speed  $v \approx c$  (see, e.g., Ref. [123]). As a result, the scattering angle as a function of the impact parameter  $\rho$  is written as follows:

$$\theta(\rho) \approx \frac{2}{\varepsilon} \left| \frac{\partial}{\partial \rho} \int_0^\infty U_a(r) dz \right|_{r=\sqrt{\rho^2+z^2}}. \quad (\text{A.5})$$

Using Eqs. (A.2)-(A.4) in (A.5) one derives

$$\theta(\rho) = \frac{1}{\varepsilon} \begin{cases} \frac{2Z}{a_{\text{TF}}} \sum_{j=1}^3 a_j b_j K_1 \left( b_j \frac{\rho}{a_{\text{TF}}} \right) & \text{Molière approx.} \\ \frac{\rho}{4} \sum_{j=1}^4 \frac{a_j}{B_j^2} \exp \left( -\frac{\rho^2}{4B_j} \right) & \text{Doyle-Turner approx.} \\ 8\pi\rho \sum_{j=1}^M \frac{a_j}{b_j} K_2(b_j\rho) & \text{Pacios approx.} \end{cases} \quad (\text{A.6})$$

Here  $K_1(\cdot)$  and  $K_2(\cdot)$  stand for the MacDonald functions of the first and second order, respectively, and notation  $B_j = b_j/(4\pi)^2$  is introduced in the case of Doyle-Turner formula.

For small arguments,  $K_1(z) \rightarrow z^{-1}$  and  $K_2(z) \rightarrow 2z^{-2}$ . Using these, one finds that in the limit of small impact parameters,  $\rho \ll a_{\text{TF}}$ , both the Molière and Pacios formulae reduce to a correct result  $2Z/\varepsilon\rho$  which is the scattering angle in the point Coulomb field  $Z/r$ . The Doyle-Turner approximation produces incorrect result,  $\theta \propto \rho$ , in this limit.

Figure A2 shows the dependences  $\theta_{\text{M,P,DT}}(\rho)$  calculated for a  $\varepsilon = 855$  MeV electron/positron scattering by carbon and silicon atoms. For the sake of comparison, the dependence for the point Coulomb field is also shown.

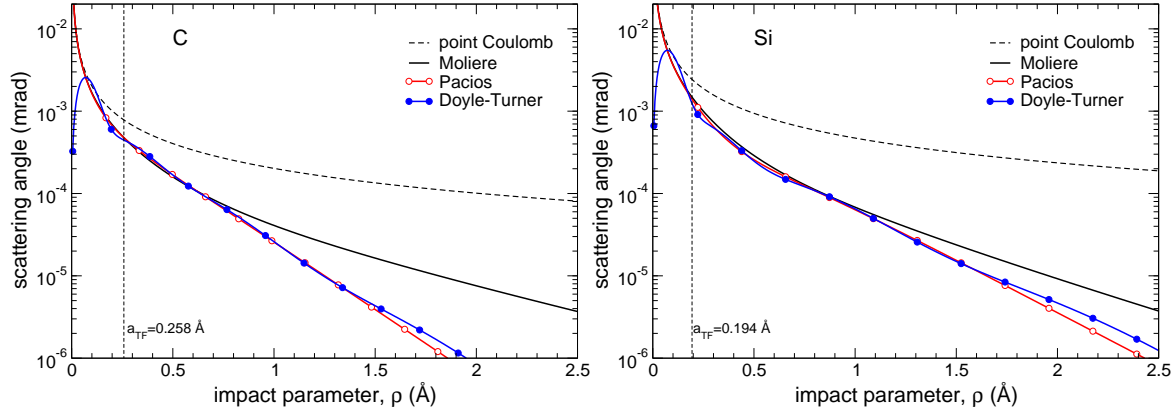


**Figure A2.** Scattering angle  $\theta$  versus impact parameter calculated for a 855 MeV electron (positron) scattered from a carbon (left) and silicon (right) atom. The dependencies obtained within the Molière, Pacios and Doyle-Turner approximations as well as for the point Coulomb field,  $Z/r$ , are presented.

### Appendix A.2. Continuous planar potential

Continuous potential  $\mathcal{U}_{\text{pl}}$  of a plane one obtains summing up the potentials  $U_{\text{at}}$  of individual atoms assuming that the latter are distributed uniformly along the plane [14]. Directing the  $y$ -axis perpendicular to the plane one writes:

$$\mathcal{U}_{\text{pl}}(y) = \mathcal{N} \int w(\Delta) d^3\Delta \int_{-\infty}^{\infty} \int_{-\infty}^{\infty} dz dx U_{\text{at}}(|\mathbf{r} - \Delta|). \quad (\text{A.7})$$

Here  $\mathcal{N} = \langle n \rangle d$  denotes the mean surface density of the atoms expressed in terms of mean volume density  $\langle n \rangle$  and interplanar distance  $d$ . Vector  $\mathbf{\Delta}$  stands for the displacement of an atom from its equilibrium position  $\mathbf{r}$  due to thermal vibrations, which are accounted for via the distribution (3).

To transform the r.h.s. of Eq. (A.7) one expresses  $U_{\text{at}}(|\mathbf{r} - \mathbf{\Delta}|)$  in terms of its Fourier transform  $\tilde{U}_{\text{a}}(q)$  and carries out the spatial integrals:

$$\mathcal{U}_{\text{pl}}(y) = \frac{\mathcal{N}}{\pi} \int_0^\infty dq e^{-\frac{q^2 u_T^2}{2}} \cos(qy) \tilde{U}_{\text{a}}(q). \quad (\text{A.8})$$

Using here the Fourier transforms from Eqs. (A.2)-(A.4) one derives planar potentials within different parameterization schemes. Below we present the collection of formulae for  $\mathcal{U}_{\text{pl}}(y)$ .

- *Molière approximation.*

$$\mathcal{U}_{\text{pl}}(y) = \pi Z \mathcal{N} \sum_{i=1}^3 \frac{\alpha_j}{\gamma_j} e^{\frac{\gamma_j^2 u_T^2}{2}} [F(y; \gamma_j, u_T) + F(-y; \gamma_j, u_T)] \quad (\text{A.9})$$

where

$$F(\pm y; \gamma_j, u_T) = e^{\pm \gamma_j y} \text{erfc}\left(\frac{\gamma_j u_T}{\sqrt{2}} \pm \frac{y}{\sqrt{2} u_T}\right). \quad (\text{A.10})$$

with  $\text{erfc}(x)$  being the complementary error function.

These expressions coincide with those presented in Refs. [124, 125].

- *Doyle-Turner approximation.*

$$\mathcal{U}_{\text{pl}}(y) = 2\pi^{1/2} \mathcal{N} \sum_{j=1}^4 \frac{a_j}{\sqrt{4B_j + 2u_T^2}} \exp\left(-\frac{y^2}{4B_j + 2u_T^2}\right) \quad (\text{A.11})$$

This expression coincides with the formulae presented in Refs. [122, 126]. The seeming deviations are due to different definitions of (i) the coefficients  $B_j$  (in the cited papers they are defined as  $B_j = b_j/4\pi^2$  whereas here it is four times less), and (ii) the rms amplitudes of thermal vibrations: in [126]  $\rho^2 = 2u_T^2$  stands for the two-dimensional rms amplitude.

- *Pacios approximation.*

$$\begin{aligned} \mathcal{U}_{\text{pl}}(y) = & \sqrt{2\pi} Z \mathcal{N} u_T e^{-\frac{y^2}{2u_T^2}} \\ & + 4\pi^2 \mathcal{N} \sum_{j=1}^M \frac{a_j}{b_j^4} e^{\frac{b_j^2 u_T^2}{2}} [(3 - b_j^2 u_T^2 - b_j y) F(y; b_j, u_T) + (3 - b_j^2 u_T^2 + b_j y) F(-y; b_j, u_T)] \end{aligned} \quad (\text{A.12})$$

with  $F(\pm y; b_j, u_T)$  defined in (A.10).



### Appendix A.3. Continuous inter-planar potentials

The inter-planar potential is obtained by summing the potentials  $\mathcal{U}_{\text{pl}}(y)$  of individual separate planes. For electrons it can be presented in the form

$$U_{\text{pl}}(y) = \mathcal{U}_{\text{pl}}(y) + \sum_{n=1}^{N_{\text{max}}} [\mathcal{U}_{\text{pl}}(y + nd) + \mathcal{U}_{\text{pl}}(y - nd)] + C, \quad (\text{A.13})$$

where  $y$  is the transverse coordinate with respect to an arbitrary selected reference plane, and the sum describes a balanced contribution from the neighboring planes. The constant term  $C$  one chooses to ensure  $U_{\text{pl}}(y)(y = 0) = 0$ . The planar potentials (A.9), (A.11) and (A.12) fall off rapidly with increasing distance from the plane. Therefore, Eq. (A.13) provides a good approximation for the inter-planar potential at already moderate numbers of the terms included in the sum. Numerical data presented below refer to  $N_{\text{max}} = 2$ . For positrons, the inter-planar potential can be obtained from Eq. (A.13) by reversing the signs of the  $\mathcal{U}_{\text{pl}}$  terms and selecting the constant  $C$  to adjust  $U_{\text{pl}}(y = \pm d/2) = 0$ .

Three graphs in Fig. A3 compares the Molière, Pacios and Doyle-Turner electron and positron planar (110) potentials in diamond, silicon and germanium crystals.

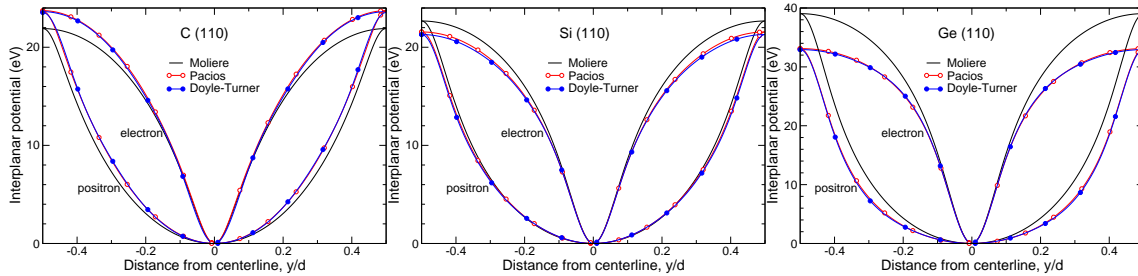


**Figure A3.** Electron and positron planar (110) potentials in diamond, silicon and germanium crystals calculated within frameworks of the Molière, Pacios and Doyle-Turner approximations.

For the sake of reference we present Fig. A4 that compares the Molière planar potentials in different oriented crystals as indicated.

## Appendix B. Continuous potential and transverse motion in a SASP Crystal

In this supplementary section, explicit formulae are derived that describe non-periodic and periodic parts of the continuous planar potential in a SASP bent crystal. The analytical and numerical analysis of the results obtained allow us to qualitatively explain the peculiar features in the motion of ultra-relativistic projectiles as well as in the radiative spectra.

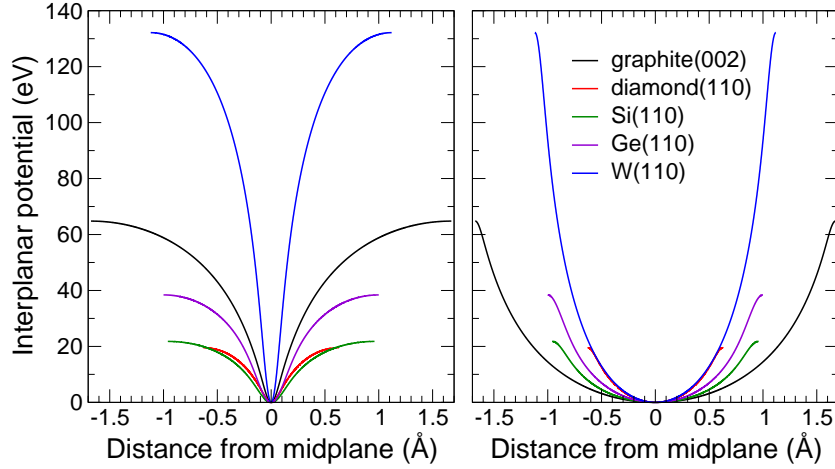


**Figure A4.** Interplanar potentials for electrons (left) and positrons (right) in Graphite (002), C(110), Si(110), Ge(110) and W(110) calculated at  $T = 300^\circ$  within the Molière approximation.

#### Appendix B.1. Continuous potential in a SASP Crystal

Consider a crystallographic plane which coincides with the  $(xz)$  Cartesian plane. For the sake of clarity, let us introduce a cosine periodic bending,  $a \cos(k_u z)$  with  $k_u = 2\pi/\lambda_u$ , of the plane in the transverse  $y$  direction. The bending amplitude  $a$  and period  $\lambda_u$  satisfy the SASP bending condition

$$a < d \ll \lambda_u, \quad (\text{B.1})$$

where  $d$  stands for the interplanar distance.

Similar to the procedure used for a straight plane (see Sect. Appendix A.2), the continuous potential of a periodically bent plane one obtains summing up the potentials of individual atoms assuming that the latter are distributed uniformly along the plane:

$$\mathcal{U}_{\text{pl}}(y, z) = \mathcal{N} \int w(\Delta) d\Delta \int_{-\infty}^{\infty} dz' \int_{-\infty}^{\infty} dx' U_{\text{at}}(|\mathbf{r} - \Delta|). \quad (\text{B.2})$$

Vector  $\Delta$  stands for the displacement of an atom from its equilibrium position, characterized by the coordinates  $(x', y', z')$  with  $y' = a \cos k_u z'$  (see illustrative Fig. B1) due to thermal vibrations.

Expressing  $U_{\text{at}}$  in terms of its Fourier transform and using (3) one integrates over  $x', z', \Delta$  and presents the planar potential in the form of a series:

$$\mathcal{U}_{\text{pl}}(y, z) = V_0(y; a) + \sum_{n=1}^{\infty} \cos(nk_u z) V_n(y; a) \quad (\text{B.3})$$

with

$$V_0(y; a) = \frac{\mathcal{N}}{\pi} \int_0^{\infty} dq e^{-\frac{q^2 a^2}{2}} \cos(qy) J_0(qa) \tilde{U}_{\text{at}}(q) \quad (\text{B.4})$$

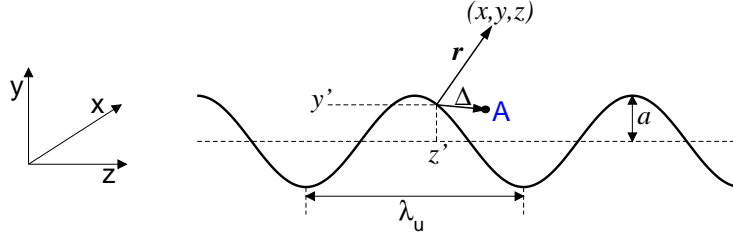


**Figure B1.** Supplementary figure illustrating the derivation of the continuous potential of a periodically bent crystallographic plane (the thick curve represents the bending profile). The atoms are displaced randomly from their equilibrium positions  $(x', y', z')$  due to thermal vibrations (the vector  $\Delta$  shows the position of a displaced atom 'A').

$$V_n(y; a) = \frac{2\mathcal{N}}{\pi} \int_0^\infty dq e^{-\frac{Q_n^2 u_T^2}{2}} J_n(qa) \tilde{U}_{\text{at}}(Q_n) \times \begin{cases} (-1)^{\frac{n}{2}} \cos(qy) \\ (-1)^{\frac{n-1}{2}} \sin(qy) \end{cases} \quad (\text{B.5})$$

where the short-hand notation  $Q_n^2 = q^2 + (nk_u)^2$  is used. The upper line stands for even  $n$  values, the lower line – for the odd ones.

In the limit of a straight channel,  $a = 0$ , the right-hand side of Eq. (B.3) reduces to that in (A.8). Indeed, taking into account that  $J_0(0) = 0$  and  $J_n(0) = 0$  for  $n > 0$ , one notices that this leads to  $V_n(y; 0) \equiv 0$  for all terms defined by (B.5) whereas the term  $V_0(y; 0)$ , Eq. (B.4), reduces to (B.3).

To determine the inter-planar potential  $U(y, z)$  one uses Eq. (A.13) where the potentials  $\mathcal{U}_{\text{pl}}(y, z)$  of individual planes are to be inserted.

The integrals on the right-hand sides of Eqs. (B.4) and (B.5) can be evaluated explicitly for a number of analytic approximations for  $U_{\text{at}}$  which can be found in literature [14, 23, 30, 47, 49, 69, 122]. For reference purposes, we present the explicit formulae derived within the framework of the Molière approximation (A.2):

$$V_n(y; a) = (1 + \delta_{n0}) \mathcal{N} Z e \sum_{j=1}^3 \frac{\alpha_j}{\Gamma_{nj}} e^{\frac{\gamma_j^2 u_T^2}{2}} \mathcal{T}_n(y; a, \Gamma_{nj}) \quad (\text{B.6})$$

Here  $\delta_{n0}$  is the Kronecker symbol,  $\Gamma_{nj} = (\gamma_j^2 + (nk_u)^2)^{1/2}$ ,  $\mathcal{T}_n$  stands for the integral:

$$\mathcal{T}_n(y; a, \Gamma) = \int_0^{\pi/2} d\theta \cos(n\theta) \left( \mathcal{F}(y - a \cos \theta; \Gamma) + (-1)^n \mathcal{F}(y + a \cos \theta; \Gamma) \right) \quad (\text{B.7})$$

where

$$\mathcal{F}(Y; \Gamma, u_T) = F(Y; \Gamma, u_T) + F(-Y; \Gamma, u_T) \quad (\text{B.8})$$

with  $F(\pm Y; \Gamma, u_T)$  defined as in (A.10).

For  $n = 0$ , Eq. (B.6) reproduces the expression derived in Ref. [40].

Similar to the case of a straight crystal, the inter-planar potential  $U(y, z)$  in a SASP bent crystal is obtained by summing up the potentials (B.3) of individual planes. For

the electron channel, the result can be written in the form

$$U(y, z) = \sum_{n=0}^{\infty} \cos(nk_u z) U_n(y) \quad (\text{B.9})$$

where

$$U_n(y) = V_n(y) + \sum_{k=1}^{K_{\max}} \left( V_n(y + kd) + V_n(y - kd) \right) + C_n. \quad (\text{B.10})$$

Here,  $y$  is the transverse coordinate with respect to an arbitrary selected reference plane, and the sum describes a balanced contribution from the neighboring planes. The constants  $C_n$  can be chosen to satisfy the condition  $U_n(0) = 0$ .

For positrons, the inter-planar potential can be obtained from Eq. (B.10) by reversing the signs of the planar potentials and selecting the constants  $C_n$  to ensure  $V_n(\pm d/2) = 0$ . Similar summation schemes allow one to calculate the charge densities, nuclear and electronic, across the periodically bent channels.

### Appendix B.2. Transverse Motion in the SASP Channel

The function  $y(t)$  describes the transverse motion of a particle with respect to the centerline of the channel. The equation of motion (EM) reads

$$\ddot{y} = -\frac{1}{m\gamma} \frac{\partial U(y, z)}{\partial y}. \quad (\text{B.11})$$

In what follows we outline a perturbative solution of the EM.

Assuming the longitudinal coordinate  $z$  changes linearly with time,  $z \approx ct$ , one re-writes the potential (B.9) substituting  $z$  with  $ct$ . Then, the EM is written as follows:

$$\ddot{y} = \frac{1}{m\gamma} \left( f_0(y) + \sum_{n=1}^{\infty} \cos(n\Omega_u t) f_n(y) \right) \quad (\text{B.12})$$

with

$$\Omega_u = k_u c = \frac{2\pi c}{\lambda_u}, \quad f_0(y) = -\frac{dU_0}{dy}, \quad f_n(y) = -\frac{dU_n}{dy}. \quad (\text{B.13})$$

The action of the time-independent force  $f_0$  results in the channeling oscillations. At the same time, the projectile experiences local small-amplitude oscillations (the jitter-like motion) due to the driving forces  $f_n \cos(n\Omega_u t)$  ( $n = 1, 2, \dots$ ). In a SASP channel, the frequency  $\Omega_u$  (and, respectively, its higher harmonics  $n\Omega_u$ ) exceeds greatly the frequency of the channeling oscillations:  $\Omega_u \gg \Omega_{\text{ch}}$ . As a result, the EM (B.12) can be integrated following the perturbative procedure outlined in Ref. [123], Sect. 30, for the motion in a rapidly oscillating field. Namely,  $y(t)$  is represented as a sum

$$y(t) = Y(t) + \Xi(t) \quad (\text{B.14})$$

where  $\Xi(t)$  stands for a small (but rapidly oscillating) correction to the smooth dependence  $Y(t)$  which describes the channeling oscillations. The function  $\Xi(t)$  satisfies the equation in which the coordinate  $Y$  is treated as a parameter:

$$\ddot{\Xi} = \sum_{n=1}^{\infty} \cos(n\Omega_u t) \frac{f_n(Y)}{m\gamma}. \quad (\text{B.15})$$

Its solution reads

$$\Xi(t, Y) = \sum_{n=1}^{\infty} \xi_n(Y) \cos(n\Omega_u t). \quad (\text{B.16})$$

where

$$\xi_n(Y) = -\frac{1}{m\gamma\Omega_u^2} \frac{f_n(Y)}{n^2} \quad (\text{B.17})$$

The presence of the term  $\Xi(t, Y)$  modifies the EM for  $Y(t)$ . In addition to the force  $f_0 = -dU_0(Y)/dY$  due to the static potential, a ponderomotive force  $f_{\text{pond}}$  appears. It can be calculated as follows [123] (below, the overline denotes averaging over the period  $2\pi/\Omega_u$  which is much smaller than the characteristic time of the channeling motion and, thus, does not affect the value of  $Y(t)$ ):

$$f_{\text{pond}}(Y) = \overline{\Xi(t, Y) \sum_{n=1}^{\infty} \cos(n\Omega_u t) \frac{df_n(Y)}{dY}} = -\frac{dU_{\text{pond}}}{dY} \quad (\text{B.18})$$

The ponderomotive potential,  $U_{\text{pond}}$ , introduced here is defined as follows:

$$U_{\text{pond}}(Y) = \frac{\lambda_u^2}{16\pi^2\varepsilon} \sum_{n=1}^{\infty} \frac{f_n^2(Y)}{n^2} \quad (\text{B.19})$$

Note that the ponderomotive correction to the potential becomes smaller as the energy increases since  $U_{\text{pond}} \propto 1/\varepsilon$ .

Therefore, the channeling oscillations  $Y = Y(t)$  are described by the EM

$$\ddot{Y} = -\frac{1}{m\gamma} \frac{dU_{\text{eff}}}{dY} \quad (\text{B.20})$$

where the total effective potential reads

$$U_{\text{eff}}(Y) = U_0(Y) + U_{\text{pond}}(Y). \quad (\text{B.21})$$

The non-periodic potential  $U_0$  and the ponderomotive term  $U_{\text{pond}}$  calculated within the Molière approximation for *positron* SASP Si(110) channel are presented in Fig. B2. The curves correspond to different bending amplitude as indicated. The right panel shows the dependence of the product  $\varepsilon U_{\text{pond}}$  (with  $\varepsilon$  measured in GeV) which is independent on the projectile energy. In both panels the vertical lines mark the (110)-planes in the straight crystal.

The modification of  $U_0$  with increase of the bending amplitude is clearly seen on the left panel in Fig. B2. In detail, this issue was discussed in Ref. [40]. Here, for the sake of consistency, we mention several features relevant to the topic of the current paper. For small and moderate amplitude values,  $a \leq 0.4 \text{ \AA}$ , the major changes in the potential is the decrease of the interplanar potential barrier. As the  $a$  values approach the  $0.4 \dots 0.6 \text{ \AA}$  range, the volume density of atoms becomes more friable leading to flattening of the potential maximum. For larger amplitudes, the potential changes in a more dramatic way as additional potential well appears. In the figure, this feature is clearly seen in the behaviour of the  $U_0$  curve for  $a = 0.8 \text{ \AA}$ : in addition to the "regular" channels centered at the midplanes, i.e. at  $y/d = \dots, -1, 0, 1, \dots$ , "complementary" channels

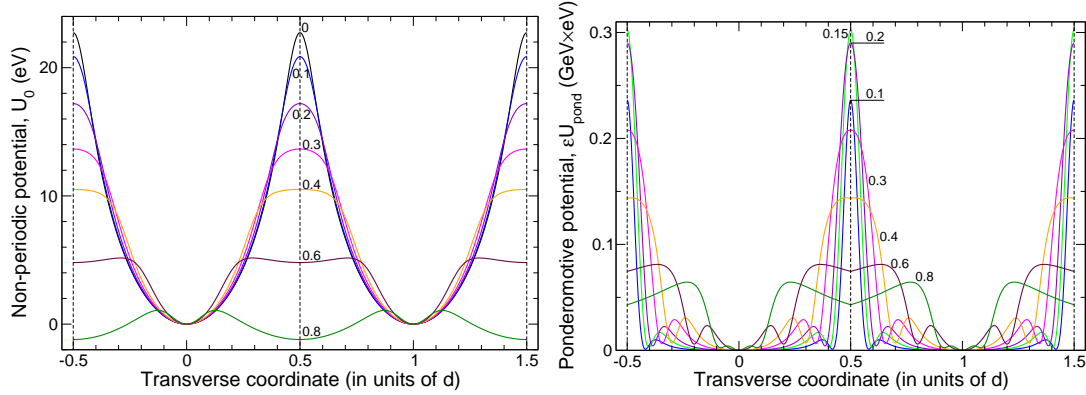


**Figure B2.** *Left.* The non-periodic part  $U_0(y)$  of the continuous inter-planar potential for positrons in Si(110) calculated at different values of bending amplitude indicated in Å near the curves ( $a = 0$  stands for the straight crystal). *Right.* The ponderomotive correction  $U_{\text{pond}}$  multiplied by  $\varepsilon$  in GeV calculated for various  $a$  and for fixed bending period  $\lambda_u = 308$  microns. The potentials shown are evaluated for temperature 300 K by using the Molière atomic potentials. The vertical dashed lines mark the adjacent (110) planes in straight crystal (the interplanar spacing is  $d = 1.92$  Å).

appear centered at  $y/d = \dots, -0.5, 0.5, \dots$ . As a result, a positron can experience channeling oscillations moving in the channels of the two different types. Similar feature characterizes the electron channeling phenomenon at sufficiently large values of bending amplitude [40].

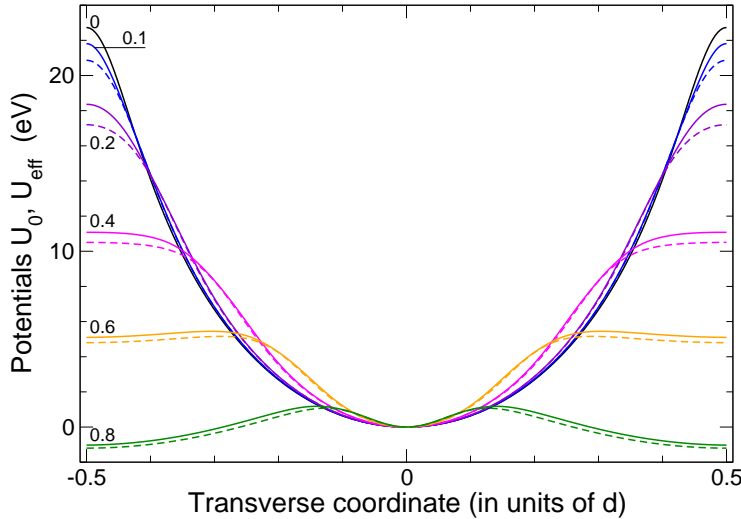


**Figure B3.** The effective interplanar potential  $U_{\text{eff}}$ , Eq. (B.21), (solid lines) for a 250 MeV positron in Si(110) at different values of bending amplitude indicated in Å near the curves ( $a = 0$  stands for the straight crystal). The dashed curves show the continuous potential  $U_0$  without the ponderomotive corrections. The bending period is  $\lambda_u = 308$  microns.

Comparing the absolute values of the ponderomotive term  $U_{\text{pond}}$  (curves in the right panel of Fig. B2 correspond to the terms at  $\varepsilon = 1$  GeV) and those of  $U_0$

one can state that for all bending amplitudes  $U_{\text{pond}}$  is a negligibly small correction to  $U_0$  for the projectile energies above 1 GeV. For much lower energies, say for a few hundreds-MeV, the contribution of  $U_{\text{pond}}$  becomes more noticeable, reaching the eV range in the regions  $2|y|/d \approx \dots, -1, 0, 1, \dots$ . Thus, it should be accounted if an accurate integration of the EM (B.20) is desired. Figure B3 illustrates the change in the continuous interplanar Si(110) potential due to the ponderomotive correction. Solid curves show the corrected potentials, the dashed ones – the term  $U_0$ . The data refer to 250 MeV positron channeling in Si(110) bent periodically with the period  $\lambda_u = 308$  microns; the values of bending amplitude (in Å) are indicated in the figure.

## References

- [1] Korol, A. V. and Solov'yov, A. V. Crystal-based intensive gamma-ray light sources *Europ. Phys. J. D* in print (2020).
- [2] Doerr, A. The new XFELs. *Nature Meth.* **13**, 33 (2018).
- [3] Seddon, E. A., Clarke, J. A., Dunning, D. J., Masciovecchio, C., Milne, C. J., Parmigiani, F., Rugg, D., Spence, J. C. H., Thompson, N. R., Ueda, K., Vinko, S. M., Wark, J. S. and Wurth, E. Short-wavelength free-electron laser sources and science: a review. *Rep. Prog. Phys.* **80**, 115901 (2017).
- [4] Milne, Ch. J., Schietinger, Th., Aiba, M., Alarcon, A., Alex, J. et al. SwissFEL: The Swiss X-ray free electron laser. *Appl. Sci.* **7**, 720 (2017).
- [5] Bostedt, Ch., Boutet, S., Fritz, D. M., Huang, Z., Lee, H. J., Lemke, H. T., Robert, A., Schlotter, W. F., Turner, J. J., Williams, G. J. Linac coherent light source: The first five years. *Rev. Mod. Phys.* **88**, 015007 (2016).
- [6] Yabashi, M. and Tanaka, H. The next ten years of X-ray science. *Nat. Photonics* **11**, 12 (2017).
- [7] Ayvazyan, V., Baboi, N., Bohnet, I., Brinkmann, R., Castellano, M. et al. A new powerful source for coherent VUV radiation: Demonstration of exponential growth and saturation at the TTF free-electron laser. *Europ. Phys. J. D* **20**, 149 (2002).
- [8] Pavlov, A. V., Korol, A. V., Ivanov, V. K. and Solov'yov, A. V. Brilliance of radiation from crystalline undulators. *In preparation* (2020).
- [9] Solov'yov, I. A., Yakubovich, A. V., Nikolaev, P. V., Volkovets, I. and Solov'yov, A. V. MesoBioNano Explorer - a universal program for multiscale computer simulations of complex molecular structure and dynamics. *J. Comp. Chem.* **33**, 2412 (2012).
- [10] <http://mbnresearch.com/get-mbn-explorer-software>
- [11] Gover, A., Friedman, A., Emma, C., Sudar, N., Musumeci, P. and Pellegrini, C. Superradiant and stimulated-superradiant emission of bunched electron beams. *Rev. Mod. Phys.* **91**, 035003 (2019).
- [12] Korol, A. V., Solov'yov, A. V. and Greiner, W. *Channeling and Radiation in Periodically Bent Crystals*, Second ed., Springer-Verlag, Berlin, Heidelberg, 2014.
- [13] W. Greiner, A. V. Korol, A. Kostyuk and A. V. Solov'yov. Vorrichtung und Verfahren zur Erzeugung elektromagnetischer Strahlung, Application for German patent, June 14, Ref.: 10 2010 023 632.2 (2010).
- [14] Lindhard, J. Influence of crystal lattice on motion of energetic charged particles. *K. Dan. Vidensk. Selsk. Mat. Fys. Medd.* **34**, 1-64 (1965).
- [15] Sushko, G. B., Bezchastnov, V. G., Solov'yov, I. A., Korol, A.V., Greiner, W. and Solov'yov, A. V. Simulation of ultra-relativistic electrons and positrons channeling in crystals with MBN Explorer. *J. Comp. Phys.* **252**, 404 (2013).
- [16] Wistisen, T. N. and Di Piazza, A. Complete treatment of single-photon emission in planar channeling. *Phys. Rev. D* **99**, 116010 (2019).



- [17] Andersen, J. U., Andersen, S. K. and Augustyniak, W. M. Channeling of electrons and positrons. *K. Dan. Vidensk. Selsk. Mat. Fys. Medd.* **39**, 1-58 (1977)
- [18] Kostyuk, A., Korol, A. V., Solov'yov, A. V. and Greiner, W. Planar channeling of 855 MeV electrons in silicon: Monte Carlo simulations. *J. Phys. B At. Mol. Opt. Phys.* **44**, 075208 (2011).
- [19] Bogdanov, O. V., Fiks, E. I., Korotchenko, K. B., Pivovarov, Yu. L. and Tukhfatullin, T. A. Basic channeling with mathematica: a new computer code. *J. Phys. Conf. Ser.* **236**, 012029 (2010).
- [20] Bagli, E. and Guidi, V. Dynecharm++: a toolkit to simulate coherent interactions of high-energy charged particles in complex structures, *Nucl. Instrum. Methods B* **309**, 124-129 (2013).
- [21] Bagli, E., Guidi, V. and Maisheev, V. A. Calculation of the potential for interaction of particles with complex atomic structures. *Phys. Rev. E* **81**, 026708 (2010).
- [22] Bandiera, L., Bagli, E., Guidi, V. and Tikhomirov, V. V. RADCHARM++: A C++ routine to compute the electromagnetic radiation generated by relativistic charged particles in crystals and complex structures. *Nucl. Instrum. Methods B* **355**, 44-48 (2015).
- [23] Baier, V. N., Katkov V. M. and Strakhovenko, V. M. *Electromagnetic Processes at High Energies in Oriented Single Crystals*. World Scientific, Singapore (1998).
- [24] Sytov, A. I., Tikhomirov, V. V. and Bandiera, L. Simulation code for modeling of coherent effects of radiation generation in oriented crystals. *Phys. Rev. Accel. Beams* **22**, 064601 (2019).
- [25] Sytov, A. and Tikhomirov, V. CRYSTAL simulation code and modeling of coherent effects in a bent crystal at the LHC. *Nucl. Instrum. Methods B* **355**, 383 (2015).
- [26] Tikhomirov, V. V. Quantum features of relativistic particle scattering and radiation in crystals. *Phys. Rev. Accel. Beams* **22**, 054501 (2019).
- [27] Guidi, V., Bandiera, L. and Tikhomirov, V. Radiation generated by single and multiple volume reflection of ultrarelativistic electrons and positrons in bent crystals. *Phys. Rev. A* **86**, 042903 (2012).
- [28] Korol, A. V., Solov'yov, A. V. and Greiner, W. The influence of the dechanneling process on the photon emission by an ultra-relativistic positron channeling in a periodically bent crystal. *J. Phys. G Nucl. Part. Phys.* **27**, 95-125 (2001).
- [29] Nielsen, C. F. GPU accelerated simulation of channeling radiation of relativistic particles. *Comp. Phys. Comm.* **252**, 107128 (2020) (see also *arXiv preprint arXiv:1910.10391v1* (2019)).
- [30] Doyle, P. A. and Turner, P. S. Relativistic Hartree-Fock X-ray and Electron Scattering Factors. *Acta Cryst. A* **24** 390-397 (1968)
- [31] Bezchastnov, V. G., Korol, A. V. and Solov'yov, A. V. Reply to Comment on 'Radiation from multi-GeV electrons and positrons in periodically bent silicon crystal' *J. Phys. B At. Mol. Opt. Phys.* **51**, 168002 (2018).
- [32] Sushko, G. B., Korol, A. V., Greiner, W., Solov'yov, A. V. Sub-GeV Electron and Positron Channeling in Straight, Bent and Periodically Bent Silicon Crystals, *J. Phys.: Conf. Ser.* **438**, 012018 (2013).
- [33] Sushko, G. B., Bezchastnov, V. G., Korol, A. V., Greiner, W., Solov'yov, A. V. Polozkov, R. G. and Ivanov, V. K. Simulations of electron channeling in bent silicon crystal. *J. Phys.: Conf. Ser.* **438**, 012019 (2013).
- [34] Polozkov, R. G., Ivanov, V. K., Sushko, G. B., Korol, A. V. and Solov'yov, A. V. Radiation emission by electrons channeling in bent silicon crystals. *Eur. Phys. J. D* **68**, 268 (2014)
- [35] Bezchastnov, V. G., Korol, A. V. and Solov'yov, A. V. Radiation from multi-GeV electrons and positrons in periodically bent silicon crystal. *J. Phys. B* **47**, 195401 (2014).
- [36] Sushko, G. B., Korol, A. V. and Solov'yov, A. V. Multi-GeV electron and positron channeling in bent silicon crystals. *Nucl. Instrum. Methods B* **355**, 39 (2015).
- [37] Sushko, G. B. *Atomistic Molecular Dynamics Approach for Channeling of Charged Particles in Oriented Crystals* (Doctoral dissertation), Goethe-Universität, Frankfurt am Main (2015).
- [38] Sushko, G. B., Korol, A. V. and Solov'yov, A. V. A small-amplitude crystalline undulator based on 20 GeV electrons and positrons: Simulations. *St. Petersburg Polytechnical Uni. J.: Phys.*

- Math.* **1**, 341 (2015) (doi: 10.1016/j.spjpm.2015.09.002).
- [39] Sushko, G. B., Korol, A. V. and Solov'yov, A. V. Electron and positron propagation in straight and periodically bent axial and planar silicon channels. *St. Petersburg Polytechnical Uni. J.: Phys. Math.* **1**, 332 (2015).
  - [40] A. V. Korol, V. G. Bezchastnov, G. B. Sushko and A. V. Solov'yov. Simulation of channeling and radiation of 855 MeV electrons and positrons in a small-amplitude short-period bent crystal. *Nucl. Instrum. Meth. B* **387**, 41-53 (2016).
  - [41] Korol, A.V., Bezchastnov, V.G., Solov'yov, A.V. Channeling and radiation of the 855 MeV electrons enhanced by the re-channeling in a periodically bent diamond crystal. *Eur. Phys. J. D* **71**, 174 (2017).
  - [42] Shen, H., Zhao, Q., Zhang, F.S., Sushko, G.B., Korol, A.V., Solov'yov, A.V. Channeling and radiation of 855 MeV electrons and positrons in straight and bent tungsten (110) crystals. *Nucl. Instrum. Meth. B* **424**, 26 (2018).
  - [43] Pavlov, A.V., Korol, A.V., Ivanov, V.K., Solov'yov, A.V. Interplay and specific features of radiation mechanisms of electrons and positrons in crystalline undulators. *J. Phys. B: At. Mol. Opt. Phys.* **52**, 11LT01 (2019).
  - [44] Pavlov, A.V., Korol, A.V., Ivanov, V.K., Solov'yov, A.V. Channeling of electrons and positrons in straight and periodically bent diamond(110) crystals. *Eur. Phys. J. D* **74**, 21 (2020).
  - [45] Haurylavets, V. V., Leukovich, A., Sytov, A., Mazzolari, A., Bandiera, L., Korol, A. V., Sushko, G. B., Solovyov, A. V. MBN Explorer atomistic simulations of electron propagation and radiation of 855 MeV electrons in oriented silicon bent crystal: theory versus experiment. Submitted to *Europ. Phys. J. C* (2020)
  - [46] G. Molière. Theorie der Streuung schneller geladener Teilchen I: Einzelstreuung am abgeschirmten Coulomb-Feld. *Z. f. Naturforsch A* **2**, 133-145 (1947).
  - [47] L. Fernandes Pacios. Analytical Density-Dependent Representation of Hartree-Fock Atomic Potentials. *J. Comp. Chem.* **14**, 410-421 (1993).
  - [48] Solov'yov, I. A., Korol, A. V. and Solov'yov A.V. *Multiscale Modeling of Complex Molecular Structure and Dynamics with MBN Explorer*. Springer International Publishing, Cham, Switzerland (2017).
  - [49] D.S. Gemmell. Channeling and related effects in the motion of charged particles through crystals. *Rev. Mod. Phys.* **46**, 129-227 (1974).
  - [50] H. Backe, private discussions (2018-2020).
  - [51] Tsyganov, E. N. Fermilab Preprints TM-682: Some aspects of the mechanism of a charged particle penetration through a monocrystal. & TM-684: Estimates of Cooling and bending processes for charged particle penetration through a monocrystal. (Fermilab, Batavia, 1976).
  - [52] Beloshitsky, V.V., Kumakhov, M.A. and Muralev, V.A. Multiple scattering of channeling ions in crystals – II. Planar channeling *Radiat. Eff.* **20**, 95 (1973).
  - [53] Scandale, W., Fiorini, M., Guidi, V., Mazzolari, A., Vincenzi, D., Della Mea, G., Vallazza, E., Afonin, A.G., Chesnokov, Yu.A., Maisheev, V.A., Yazynin, I.A., Kovalenko, A.D., Taratin, A.M., Denisov, A.S., Gavrikov, Yu.A., Ivanov, Yu.M., Lapina, L.P., Skorobogatov, V.V., Bolognini, D., Hasan, S. and Prest, M. Measurement of the dechanneling length for high-energy negative pions. *Phys. Lett.* **B719**, 70 (2013).
  - [54] Backe, H., Kunz, P., Lauth, W. and Rueda, A. Planar Channeling Experiments with Electrons at the 855-MeV Mainz Microtron. *Nucl. Instrum. Methods B* **266**, 3835 (2008).
  - [55] Bogdanov, O.V. and Dabagov, S.N. Radiation Spectra of Channeled Electrons in Thick Si (111) Crystals, *J. Phys.: Conf. Ser.* **357**, 012029 (2012).
  - [56] V.M. Biryukov, Yu.A. Chesnokov and V.I. Kotov. *Crystal Channeling and its Application at High-Energy Accelerators*. (Springer Science & Business Media, 2013).
  - [57] Mazzolari, A., Bagli, E., Bandiera, L., Guidi, V., Backe, H., Lauth, W., Tikhomirov, V., Berra, A., Lietti, D., Prest, M., Vallazza, E. and De Salvador, D. Steering of a Sub-GeV Electron Beam through Planar Channeling Enhanced by Rechanneling, *Phys. Rev. Lett.* **112**, 135503

- (2014).
- [58] Wienands, U., Markiewicz, T.W., Nelson, J., Noble, R.J., Turner, J.L. Uggerhøj, U.I., Wistisen, T.N., Bagli, E., Bandiera, L., Germogli, G., Guidi, V., Mazzolari, A., Holtzapple, R. and Miller, M. Observation of Deflection of a Beam of Multi-GeV Electrons by a Thin Crystal, *Phys. Rev. Lett.* **114**, 074801 (2015).
  - [59] Wistisen, T.N., Uggerhøj, U.I., Wienands, U., Markiewicz, T.W., Noble, R.J., Benson, B.C., Smith, T., Bagli, E., Bandiera, L., Germogli, G., Guidi, V., Mazzolari, A., Holtzapple, R.L. and Tucker, S. Channeling, volume reflection, and volume capture study of electrons in a bent silicon crystal. *Phys. Rev. Accel. Beams* **19**, 071001 (2016).
  - [60] Backe, H. and Lauth, W. Channeling Experiments with Sub-GeV Electrons in Flat Silicon Single Crystals. *Nucl. Instrum. Meth. B* **355**, 24-29 (2015).
  - [61] Sytov, A.I., Bandiera, L., De Salvador, D., Mazzolari, A., Bagli, E., Berra, A., Carturan, S., Durighello, C., Germogli, G., Guidi, V., Klag, P., Lauth, W., Maggioni, G., Prest, M., Romagnoni, M., Tikhomirov, V. V. and Vallazza, E. Steering of Sub-GeV electrons by ultrashort Si and Ge bent crystals. *Eur. Phys. J. C* **77**, 901 (2017).
  - [62] Backe, H. Electron channeling experiments with bent silicon single crystals – a reanalysis based on a modified Fokker-Planck equation. *JINST* **13**, C02046 (2018).
  - [63] Tanabashi, M. et al. (Particle Data Group): Review of Particle Physics, *Phys. Rev. D* **98**, 030001 (2018).
  - [64] Jackson, J.D. *Classical Electrodynamics* (Wiley, Hoboken, 1999)
  - [65] Tsai, Y.-S. Pair production and bremsstrahlung of charged leptons. *Rev. Mod. Phys.* **46**, 815 (1974).
  - [66] Bak, J., Ellison, J. A., Marsh, B., Meyer, F. E., Pedersen, O., Petersen, J. B. B., Uggerhøj, E. and Østergaard, K. Channeling radiation from 2-55 GeV/c electrons and positrons: (I) planar case. *Nucl. Phys. B.* **254**, 491 (1985).
  - [67] Atkinson, M., Bak, J. F., Bussey, P. J., Christensen, P., Ellison, J. A., Ellison, R. J., Eriksen, K. R., Giddings, D., Hughes-Jones, R. E., Marsh, B. B., Mercer, D., Meyer, F. E. Moller, S. P., Newton, D., Pavlopoulos, P., Sharp, P. H., Stensgaard, R., Suffert, M. and Uggerhøj, E. Radiation from planar channeled 5-55 GeV positrons and electrons. *Phys. Lett. B* **110**, 162 (1982).
  - [68] Tikhomirov, V. V. A benchmark construction of positron crystal undulator. arXiv preprint arXiv:1502.06588 (2015).
  - [69] Chouffani, K. and Überall, H. Theory of Low Energy Channeling Radiation. *phys. stat. sol. (b)* **213**, 107-151 (1999).
  - [70] Uggerhøj, E. Some recent experimental investigations of photon emission and shower formation in strong crystalline fields. *Rad. Eff. Def. Solids* **25**, 3 (1993).
  - [71] Carrigan, A. and Ellison, J. (eds.): *Relativistic Channeling*. Plenum, New York (1987)
  - [72] Scandale, W., Arduini, G., Cerutti, F., Garattini, M., Gilardoni, S., Lechner, A., Losito, R., Masi, A., Mirarchi, D. et al. Focusing of 180 GeV/c pions from a point-like source into a parallel beam by a bent silicon crystal. *Nucl. Instrum. Method B* **446**, 15–18 (2019).
  - [73] Takabayashi, Y., Pivovarov, Yu.L. and Tukhfatullin, T.A. First observation of scattering of sub-GeV electrons in ultrathin Si crystal at planar alignment and its relevance to crystal-assisted 1D rainbow scattering. *Phys. Lett.* **B785**, 347-353 (2018).
  - [74] Backe, H., Lauth, W. and Tran Thi, T. N. Channeling experiments at planar diamond and silicon single crystals with electrons from the Mainz Microtron MAMI. *JINST* **13**, C04022 (2018).
  - [75] Mazzolari, A., Sytov, A., Bandiera, L., Germogli, G., Romagnoni, M., Bagli, E., Guidi, V., Tikhomirov, V. V., De Salvador, D., Carturan, S., Durighello, C., Maggioni, G., Campostrini, M., Berra, A., Mascagna, V., Prest, M., Vallazza, E., Lauth, W., Klag, P. and Tamisari, M. Broad angular anisotropy of multiple scattering in a Si crystal. *Eur. Phys. J. C* **80**, 63 (2020).
  - [76] Tran Thi, T. N., Morse, J., Caliste, D., Fernandez, B., Eon, D., Härtwig, J., Barbay, C., Mer-Calfati, C., Tranchant, N. Arnault, J. C., Lafford, T. A. and Baruchel, J. Synchrotron Bragg

- diffraction imaging characterization of synthetic diamond crystals for optical and electronic power device applications. *J. Appl. Cryst.* **50**, 561 (2017).
- [77] Nething, U., Galemann, M., Genz, H., Höfer, M., Hoffmann-Stascheck, P., Hormes, J., Richter, A. and Sellschop, J. P. Intensity of electron channeling radiation, and occupation lengths in diamond crystals. *Phys. Rev. Lett.* **72**, 2411–2413 (1994).
  - [78] Boshoff, D., Copeland, M., Haffeejee, F., Kilbourn, Q., MacKenzie, B., Mercer, C., Osato, A., Williamson, C., Sihoyiya, P., Motsoai, M., Connell, M., Henning, C.A., Connell, S.H., Palmer, N.L., Brooks, T., Härtwig, J., Tran Thi, T. N. and Uggerhøj, U. The search for crystal undulator radiation. In *Proc. of SAIP 2016* (Ed. S. Peterson, S. Yacoob) p. 112 (2017).
  - [79] Brau, C. A., Choi, B.-K., Jarvis, J. D., Lewellen, J. W. and Piot, P. Channeling Radiation as a Source of Hard X-rays with High Spectral Brilliance. *Synchrotron Radiat. News* **25**, 20 (2012).
  - [80] <https://www6.slac.stanford.edu/facilities/facet.aspx>
  - [81] Uggerhøj, U. The interaction of relativistic particles with strong crystalline fields. *Rev. Mod. Phys.* **77**, 1131 (2005).
  - [82] Kovalenko, A. D., Mikhailov, V. A., Taratin, A. M., Boiko, V. V., Kozlov, S. I. and Tsyganov, E. N. Bent Tungsten Crystal as Deflector for High Energy Particle Beams, *JINR Rapid Comm.* **72**, 9–18 (1995).
  - [83] Yoshida, K., Goto, K., Isshiki, T., Endo, I., Kondo, T., Matsukado, K., Takahashi, T., Takashima, Y., Potylitsin, A., Amosov, C. Yu., Kalinin, B., Naumenko, G., Verzilov, V., Vnukov, I., Okuno, H., and Nakayama, K. Positron Production in Tungsten Crystals by 1.2-GeV Channeling Electrons, *Phys. Rev. Lett.* **80**, 1437–1440 (1998).
  - [84] Backe, H., Lauth, W., Scharafutdinov, A. F., Kunz, P., A. S. Gogolev and Potylitsyn, A. P. Forward Diffracted Parametric X Radiation From a Thick Tungsten Single Crystal at 855 MeV Electron Energy, *Proc. SPIE* **6634**, 66340Z (2007).
  - [85] Kostyuk, A., Korol, A. V., Solov'yov, A. V. and Greiner, W. The Influence of the Structure Imperfectness of a Crystalline Undulator on the Emission Spectrum, *Nucl. Instrum. Meth. B* **266**, 972–987 (2008).
  - [86] Rand, Brian. Graphite: Structure, properties and manufacture. <https://pdfslide.net/documents/graphite-structure-properties-and-manufacture.html>
  - [87] M.S. Dresselhaus, R. Kalish. Ion Implantation in Diamond, Graphite and Related Materials. Springer Science & Business Media (Springer-Verlag, Berlin, Heidelberg, New York, 2013).
  - [88] Kaplin, V. V., Vorobev, S. A. On the Electromagnetic Radiation of Channeled Particles in a Curved Crystal. *Phys. Lett.* **67A**, 135–137 (1978).
  - [89] Bashmakov, Yu. A. Radiation and Spin Separation of High Energy Positrons Channeled in Bent Crystals. *Radiat. Eff.* **56**, 55–60 (1981).
  - [90] Taratin, A. M., Vorobiev, S. A. Radiation of High-Energy Positrons Channeled in Bent Crystals. *Nucl. Instrum. Meth. B* **31**, 551–557 (1988).
  - [91] A.M. Taratin, S.A. Vorobiev: Quasi-Synchrotron Radiation of High-Energy Positrons Channeled in Bent Crystals. *Nucl. Instrum. Meth. B* **42**, 41–45 (1989).
  - [92] Arutyunov, V.A., Kudryashov, N.A., Samsonov, V.M., Strikhanov, M.N. Radiation of Ultrarelativistic Charged Particles in a Bent Crystal. *Nucl. Phys. B* **363**, 283–300 (1991).
  - [93] Solov'yov, A.V., Schäfer, A., Greiner, W. Channeling Process in a Bent Crystal. *Phys. Rev. E* **53**, 1129–1137 (1996).
  - [94] Polozkov, R. G., Ivanov, V. K., Sushko, G. B., Korol, A.V., Solov'yov, A. V. Channeling of Ultra-Pelativistic Positrons in Bent Diamond Crystals. *St. Petersburg Polytechnical Uni. J: Phys. Math.*, **1**, 212–218 (2015).
  - [95] Backe, H., Krambrich, D., Lauth, W., Lundsgaard, H. J. and Uggerhøj, U. K. I. X-ray emission from a crystal undulator: Experimental results at channeling of electrons, *Nuovo Cimento C* **34**, 157 (2011).
  - [96] Backe, H., Lauth, W., Kunz, P., Rueda, A., Esberg, A., Kirsebom, K., Hansen, J. L. and Uggerhøj,

- U. K. I. Photon Emission of Electrons in a Crystalline Undulator. In *Charged and Neutral Particles Channeling Phenomena* (Eds: S. B. Dabagov, L. Palumbo, A. Zichichi) pp. 281-290. Singapore, World Scientific, 2010.
- [97] Mikkelsen, U. and Uggerhøj, E. A crystalline undulator based on graded composition strained layers in a superlattice. *Nucl. Instrum. Methods B*, **160**, 435 (2000).
- [98] Fei Mao, Gennady B. Sushko, Andrei V. Korol, Andrey V. Solov'yov, Wei Cheng, Haibo Sang, Feng-Shou Zhang. Radiation by ultra-relativistic positrons and electrons channeling in periodically bent diamond crystals. *Unpublished* (2015).
- [99] Backe, H. and Lauth, W. "Channeling Experiments with Electrons at the Mainz Microtron" in *4th Int. Conf. "Dynamics of Systems on the Nanoscale"* (Bad Ems, Germany, Oct. 3-7 2016) Book of Abstracts, p. 58 (2016).
- [100] Taratin, A. M. and Vorobiev, S. A. Volume reflection of high-energy charged particles in quasi-channeling states in bent crystals. *Phys. Lett.* **119**, 425 (1987).
- [101] Nielsen, C. F., Uggerhøj, U. I., Holtzapple, R., Markiewicz, T.W., Benson, B.C., Bagli, E., Bandiera, L., Guidi, V., Mazzolari, A., Wienands, U. Photon emission by volume reflected electrons in bent crystals. *Phys. Rev. Acc. Beams* **22**, 114701 (2019)
- [102] Taratin, A. M. and Vorobiev, S. A. Deflection of high-energy charged particles in quasi-channeling states in bent crystals. *Nucl. Instrum. Meth. B* **26**, 512 (1987).
- [103] Shul'ga, N. F., Boyko, V. V. and Esaulov, A. S. New mechanism of jump formation in a spectrum of coherent radiation by relativistic electrons in the field of periodically deformed crystal planes of atoms. *Phys. Lett. A* **372**, 2065–2068 (2008).
- [104] Korol, A. V., Solov'yov, A. V. and Greiner, W. Coherent radiation of an ultrarelativistic charged particle channeled in a periodically bent crystal. *J. Phys. G: Nucl. Part. Phys.* **24**, L45 (1998).
- [105] Korol, A. V., Solov'yov, A. V. and Greiner, W. Photon emission by an ultra-relativistic particle channeling in a periodically bent crystal. *Int. J. Mod. Phys. E* **8**, 49 (1999).
- [106] Korol, A. V., Solov'yov, A. V. and Greiner, W. Channeling of positrons through periodically bent crystals: On the feasibility of crystalline undulator and gamma-laser. *Int. J. Mod. Phys. E* **13**, 897 (2004).
- [107] Kostyuk, A. Crystalline undulator with a small amplitude and a short period. *Phys. Rev. Lett.* **110**, 115503 (2013).
- [108] Wistisen, T. N., Andersen, K. K., Yilmaz, S., Mikkelsen, R., Hansen, J. L., Uggerhøj, U. I., Lauth, W. and Backe, H. Experimental realization of a new type of crystalline undulator. *Phys. Rev. Lett.* **112**, 254801 (2014).
- [109] Uggerhøj, U. I. and Wistisen, T. N. Intense and energetic radiation from crystalline undulators. *Nucl. Instrum Meth. B* **355**, 35 (2015).
- [110] Uggerhøj, U. I., Wistisen, T. N., Hansen, J. L., Lauth, W. and Klag, P. Radiation collimation in a thick crystalline undulator. *Eur. J. Phys. D* **71**, 124 (2017).
- [111] Wienands, U., Gessner S., Hogan, M. J., Markiewicz, T. W., Smith, T., Sheppard, J., Uggerhøj, U. I., Hansen, J. L., Wistisen, T. N., Bagli, E., Bandiera, L., Germogli, G., Mazzolari, A., Guidi, V., Sytov, A., Holtzapple, R.L., McArdle, K., Tucker, S., Benson, B. Channeling and radiation experiments at SLAC. *Nucl. Instrum Meth. B* **402**, 11 (2017).
- [112] Medvedev, M. V. Theory of "jitter" radiation from small-scale random magnetic fields and prompt emission from gamma-ray burst shocks. *The Astrophys. J.* **540**, 704-714 (2000).
- [113] Kellner, S. R., Aharonian, F. A. and Khangulyan, D. On the jitter radiation. *The Astrophys. J.* **774**, 61 (2013).
- [114] G.B. Sushko, A.V. Korol, and A.V. Solov'yov. Unpublished (2016).
- [115] SLAC Site Office: *Preliminary Conceptual Design Report for the FACET-II Project at SLAC National Accelerator Laboratory*. Report SLAC-R-1067, SLAC (2015).
- [116] Korol, A. V., Solov'yov, A. V. and Greiner, W. Total Energy Losses due to the Radiation in an Acoustically Based Undulator: The Undulator and channeling radiation included. On the feasibility of crystalline undulator and gamma-laser. *Int. J. Mod. Phys. E* **9**, 77 (2000).



- [117] Nielsen, C. F., Justesen, J. B., Sørensen, A. H., Uggerhøj, U. I., Holtzapple, R. Radiation reaction near the classical limit in aligned crystals. *Phys. Rev. D* **102**, 052004 (2020).
- [118] Landau, L.D., Lifshitz, E.M.: *Course of Theoretical Physics, vol. 2. The classical theory of fields*. Elsevier Butterworth-Heinemann, Oxford (2005).
- [119] Sushko, G. B., Solov'yov, I. A., and Solov'yov, A. V. Molecular dynamics for irradiation driven chemistry: application to the FEBID process. *Eur. Phys. J. D* **70**, 217 (2016).
- [120] Tikhomirov, V. V. Quantum features of high energy particle incoherent scattering in crystals. *Phys. Rev. Accel. Beams* **22**, 054501 (2019) (Erratum: *ibid.* **23**, 039901 (2020)).
- [121] Waasmaier, D. and Kirfel, A. New analytical scattering-factor functions for free atoms and ions. *Acta Cryst.* **A51**, 416-431 (1995).
- [122] G.V. Dedkov, Interatomic potentials of interactions in radiation physics *Sov. Phys. - Uspekhi* **38**, 877-910 (1995).
- [123] Landau, L.D., Lifshitz, E.M.: *Course of Theoretical Physics, vol. 1. Mechanics*. Elsevier, Oxford (2003)
- [124] Appleton, B.R., Erginsoy, C. and W.M. Gibson: Effects in the Energy Loss of 3-11-MeV Protons in Silicon and Germanium Single Crystals. *Phys. Rev.* **161**, 330-349 (1967).
- [125] Erginsoy, C. Anisotropic Effects in Interactions of Energetic Charged Particles in a Crystal Lattice. *Phys. Rev. Lett.* **15**, 360-363 (1965).
- [126] Møller, S.P. High-energy channeling – applications in beam bending and extraction. *Nucl. Instrum. Method A* **361**, 403–420 (1995).